

Hybrid torque and SQUID magnetometry of individual magnetic nanotubes

Inauguraldissertation

zur Erlangung der Würde eines Doktors der Philosophie

vorgelegt der
Philosophisch-Naturwissenschaftlichen Fakultät
der Universität Basel

von

Arne Buchter

aus Reutlingen, Deutschland

Basel, 2015



Originaldokument gespeichert auf dem Dokumentenserver der Universität Basel edoc.unibas.ch.

Genehmigt von der Philosophisch-Naturwissenschaftlichen Fakultät auf Antrag von

Prof. Dr. Martino Poggio
Fakultätsverantwortlicher

Prof. Dr. Jean-Philippe Ansermet
Korreferent

Basel, den 13.10.2015

Prof. Dr. Jörg Schibler
Dekan

Contents

1. Introduction	1
2. Magnetism	5
2.1. Introduction	5
2.2. Magnetic field	5
2.3. Different kinds of magnetism	6
2.3.1. Diamagnetism and paramagnetism	6
2.3.2. Ferromagnetism and antiferromagnetism	8
2.4. Exchange bias	10
2.5. Magnetism of small particles	13
2.5.1. Interactions and characteristic length scales in magnetic materials	13
2.5.2. Stoner-Wohlfarth model and beyond	14
2.6. Review of experimental techniques	17
3. Torque Magnetometry	21
3.1. Introduction	21
3.2. Dynamic cantilever magnetometry (DCM)	21
3.2.1. The high-field limit	25
3.2.2. The low-field limit	25
4. Superconducting Quantum Interference Device (SQUID)	27
4.1. Introduction	27
4.2. Superconductivity	27
4.3. Josephson effect	30
4.4. The dc SQUID	32
5. Experimental setup	37
5.1. Introduction	37
5.2. Ultrasoft Si cantilever	37
5.3. Ni, CoFeB and permalloy nanotubes	38
5.4. Sample to cantilever attachment	40
5.5. He ³ cryostat	41
5.6. Nb nanoSQUID and its operation	43
5.7. Scanning probe microscopy	44
6. Nanoscale multifunctional sensor formed by a Ni nanotube and a scanning Nb nanoSQUID	47
6.1. Introduction	48
6.2. SQUID layout, properties and readout	49
6.3. Low temperature magnetic force microscopy setup	49

6.4. Magnetic force microscopy imaging of an Abrikosov vortex	51
6.5. Experimental determination of the spatial flux signal dependence	52
6.6. Analysis with spatial dependent coupling factor	54
6.7. Displacement detection	55
6.8. Conclusion	55
7. Reversal mechanism of an individual Ni nanotube simultaneously studied by torque and SQUID magnetometry	57
7.1. Introduction	58
7.2. Setup and methods	58
7.3. SQUID magnetometry	60
7.4. High and low field characterization with DCM	61
7.5. Micromagnetic simulations	62
7.6. Comparison of DCM and SQUID magnetometry data	63
7.7. Conclusion	64
8. Magnetization reversal nucleating at the end of a CoFeB nanotube detected with SQUID and torque magnetometry	65
8.1. Introduction	66
8.2. Setup	66
8.3. High and low field characterization with DCM	67
8.4. SQUID magnetometry	68
8.5. Conclusion and outlook	70
9. Magnetization reversal of an individual exchange biased permalloy nanotube	71
9.1. Introduction	72
9.2. Setup	72
9.3. DCM high field characterization	74
9.4. Training effect	75
9.5. Temperature dependence	78
9.6. X-ray absorption spectroscopy of permalloy oxides	79
9.7. Conclusion	81
10. Conclusions & Outlook	83
References	87
A. Supplement to chapter 7	105
Acknowledgements	113
Curriculum Vitae	115
Education	115
List of Publications	116

1. Introduction

”The hysteresis loop is central to technical magnetism; physicists endeavour to explain it, materials scientists aim to improve it and engineers work to exploit it.” [1]. It is the central feature common to all material systems including ferromagnetic components below their ordering temperature, the Curie temperature T_C . The range of applications for magnets has been and still is immense. To name just a few, they are used in motors, as cores in transformers, form the basis of audio devices like speakers, contactless sensing relies on magnets as do simple holding devices and as a major field, magnetic recording and data storage.

The requirements of these various applications on the specific magnets differ strongly. Magnets in motors or speakers need to be hard magnets, i.e. they have to withstand thermal effects and magnetic fields with their magnetization remaining. The magnets in transformers need to be soft magnets switching their magnetization easily with small applied fields to minimize losses. To choose a suitable material for each specific application, detailed knowledge of the magnet’s properties i.e. its hysteresis loop is indispensable.

A more complicated case are memory applications including data recording and storage, which can also be seen as a driving force to research on magnetism. Here the small magnetic regions assigned to single bits, on the one hand have to switch easily, but on the other also have to maintain the information in the form of stable magnetization. Apart from the challenge of finding and designing the appropriate materials in data storage, the ever increasing density also poses challenges in understanding fundamental physical mechanisms.

Magnetic random access memory (MRAM) for example evolved from the macroscopic magnetic core memory with inductive read-out to highly integrated MRAM devices employing spin valves relying on the quantum mechanical giant magnetoresistance effect (GMR) [2, 3]. GMR is observed for currents flowing through ferromagnetic multilayers, where the electrical resistance depends on the layers’ magnetization being parallel or antiparallel [4]. For application in spin valves the magnetization of a ferromagnetic layer can be pinned by an additional antiferromagnetic layer, exploiting exchange bias [5].

GMR has also been a crucial effect to allow for further increase of the memory density on magnetic hard disk drives. However, the size of a magnetic bit can not be reduced arbitrarily. At some point magnetization is not stable any more and temperature induced flips of the magnetization can occur, which is referred to as the superparamagnetic limit [6]. On the long run new ways have to be found to circumvent these limitations.

One way to avoid these limitations is by going to the third dimension and away from static bits written to a medium. A promising proposal is, to encode information in domain walls moving through nanowires, which are then read-out [7]. Similar to this, for planar geometries domain wall logic elements based on nanowires have been proposed and to some extent realized [8]. To realize such memory devices, going back to first sentence of the introduction, joint forces are needed.

The proposal is based on fast, reproducible domain wall movements in high aspect ratio nanoscale particles. There is extensive research on theory and modelling of the dynamic behaviour of ferromagnetic nanowires and nanotubes (NT). These investigations have shown

that NTs omit the magnetic point singularity that is existent in nanowires [9]. What makes NTs especially promising is the proposed high domain wall velocity, avoiding the so-called Walker breakdown [10]. The phase diagram for magnetic states, depending on the NT's geometry has been explored, as well as the reversal mechanism and possibilities to drive domain walls with current pulses [11–14].

A fundamental aspect is high quality and reliable material growth. To fabricate ferromagnetic nanowires and NTs, electrochemical and atomic layer deposition in anodic aluminium oxide templates has become a reliable fabrication method [15–18]. It is possible to fabricate large arrays of various geometries and materials with a broad range of particle separation. Apart from growing the particles in templates, epitaxial growth has been demonstrated [19, 20] as well as coating of semiconductor nanowires [21, 22]

An arising challenge is the thorough analysis in order to understand the physics in a real sample and how it is influenced by material's properties like roughness, impurities or influence of the geometry. There are plenty of studies conducted with various experimental techniques [15, 23–25]. Most studies however are on ensembles which is due to the limited sensitivity of the measurement techniques in conjunction with the small magnetic moment of an individual particle caused by the inherently small volume. The drawback is that properties on the single particle level are obscured by averaging effects and altered due to interaction [16, 24, 26]. To properly characterize such particles, measurements on the single particle level are necessary.

Despite the difficulties, there are methods available that have already proven capable of detecting signal from single magnetic nanoparticles. This is anisotropic magnetoresistance measurements, cantilever magnetometry and SQUID magnetometry to name just the ones relevant in the light of the thesis [21, 22, 27–33].

It is the aim of this thesis to develop a versatile magnetometer consisting of well-proven devices, capable of investigating single magnetic nanoscale particles. The magnetometer consists of an ultrasensitive Si cantilever and a Nb nanoSQUID. The devices support complementary measurement principles with the cantilever being sensitive to the volume magnetization of the magnetic particle attached to its tip and the nanoSQUID detecting its stray field. Attaching a single NT with its long axis parallel to that of the cantilever we investigate Ni, CoFeB and permalloy NTs with the developed hybrid magnetometer.

The thesis is organized as follows. In chapter 2 some basic concepts of the wide field of magnetism relating to the results presented in this thesis, are compiled.

Chapter 3 introduces the technique of dynamic cantilever magnetometry emphasizing on the mathematical framework used to analyze the data presented in the thesis.

The condensate of superconductivity and the Josephson effect that is needed to understand the basic working principles of a dc SQUID are presented in chapter 4.

Chapter 5 presents the samples used, their preparation and the key components of the hybrid magnetometer setup, namely the cryostat, cantilever and nanoSQUID.

These four chapters build the basis for the results presented in the following chapters 6-9.

The results presented in chapter 6 are fundamental in characterizing the hybrid magnetometer regarding the nanoSQUID's capabilities. The coupling of stray fields in the nanoSQUID is mapped out in detail by a Ni NT positioned in the three dimensional half space above the nanoSQUID. Furthermore scanning probe data relying on the magnet-tipped cantilever to detect Abrikosov vortices in the superconducting structure is presented.

In chapter 7 and 8 the magnetization reversal of a single Ni and respectively CoFeB NT are investigated. The Ni NT exhibits significant surface roughness, while the CoFeB NT is formed by a smooth magnetic film. Comparing the results obtained on the reversal of volume magnetization and stray field with micromagnetic simulations we identify surface morphology as an important influence on NT's magnetization reversal. Furthermore the NTs' saturation magnetizations are determined by dynamic cantilever magnetometry.

In chapter 9 experiments on the reversal of a single permalloy NT are presented. We find the hysteresis loop to be shifted along the field axis, which we account to exchange bias. In further experiments we confirm exchange bias by measuring the training effect and the temperature dependence of the magnetization reversal. Performing X-ray absorption spectroscopy, we find Fe and Ni oxides in the NT's surface layer. The compounds found are known to show antiferromagnetic order, thus confirming exchange bias.

The conclusion and outlook are presented in chapter 10 to round off the thesis.

k_0, l_e, μ_0	physical constants and quantities	italic lower case letters
θ, Φ'	angles	greek letters
\mathbf{M}, \mathbf{H}	vector physical quantities	italic boldface upper case letters
M_s, V, H	norm of physical quantities	italic upper case letters
\hat{x}, \hat{z}'	unit vector	lower case letters with hat

Table 1.1. | Notation

2. Magnetism

2.1. Introduction

This chapter is intended to provide a brief introduction into the relevant topics and principles of magnetism needed to understand the results presented in the experimental part of this thesis. By no means this chapter is supposed to be complete, but it shall rather serve as a condensed handbook for the reader of this work. The main parts presented follow, if not otherwise stated, the books of Kittel, Skomski/Coey and Aharoni [34–36]

The first section deals with the concept of magnetic fields, the second section gives an overview on the different kinds of magnetism and magnetic order present in solids. Section 3 is devoted to the foundations of the exchange bias effect. In Section 4 the Stoner-Wohlfahrt model describing the magnetization of single-domain particles is introduced before we turn to the influence of reduced size and dimension in nanoscale samples and experimental techniques to measure such nanoscale magnetic samples.

2.2. Magnetic field

Generation of magnetic fields is possible by electrical currents or permanent magnets. The magnetic field \mathbf{H} is also known as "magnetizing force" due to its ability to create a magnetic or superconducting response in a solid and has the unit A/m. The magnetization \mathbf{M} of most materials, which is defined as dipole moment per unit volume, has the same unit as the magnetic field and is directly proportional to it

$$\mathbf{M} = \chi \mathbf{H}. \quad (2.1)$$

The dimensionless parameter χ is the material's susceptibility (more details on this parameter and its implications are covered in the next section). The material's magnetization generates a demagnetizing field [35]

$$\mathbf{H}_d(\mathbf{r}) = \frac{1}{4\pi} \int \frac{(\mathbf{r} - \mathbf{r}') \nabla \mathbf{M}(\mathbf{r}') d\mathbf{r}'}{|\mathbf{r} - \mathbf{r}'|^3}, \quad (2.2)$$

outside the material this is also referred to as the magnet's stray field. The total, internal magnetic field is then determined by the externally applied field and the demagnetizing field as $\mathbf{H}' = \mathbf{H} + \mathbf{H}_d$ [35].

The so called flux density or magnetic induction is given in units of Tesla $T=N/(Am)$ and is defined as

$$\mathbf{B} = \mu_0(\mathbf{H}' + \mathbf{M}). \quad (2.3)$$

The physical constant $\mu_0 = 4\pi \times 10^{-7} NA^{-2}$ is known as vacuum permeability. Multiplying \mathbf{H}' and \mathbf{M} by this constant allows to express these values in the more common units of Tesla rather than A/m. To visualize the connection between \mathbf{H}' , \mathbf{M} and \mathbf{B} on the example of a

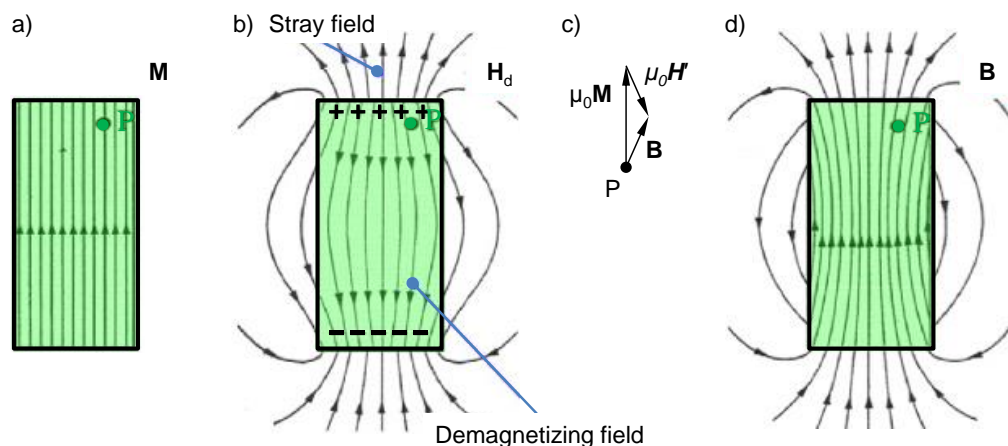


Figure 2.1. | Illustration of a bar shaped magnet's a) magnetization \mathbf{M} , b) demagnetizing and stray field \mathbf{H}_d , d) magnetic flux density \mathbf{B} and c) its vectorial components evaluated at point P inside the magnet. The figure is adapted from [37].

bar-shaped permanent magnet a sketch, adapted from [37], is shown in Fig. 2.1. The sketch uses the concept of magnetic field lines, that exemplify the force of a magnetic field on a test dipole, for visualization. These field lines follow closed lines, their density is proportional to the field strength and the tangent along a field line gives the direction of magnetic force.

2.3. Different kinds of magnetism

The following section covers the different contributions to magnetization in matter. The focus lies in an overview of the fundamental physics, important parameters and some relevant materials with respect to this thesis. A first and simple differentiation of the phenomena covered in the following paragraphs can be carried out via the material's response to a magnetic field, i.e. its magnetic susceptibility, defined in Eq. 2.1. Dia- and paramagnets, which are covered in the next subsection, show a negative and respectively positive susceptibility following simple rules. The subsequent passage covers the phenomena of ferro- and antiferromagnetism which show a more complex behaviour regarding its susceptibility and also the underlying physics. Furthermore the related phenomena of ferrimagnetism is discussed in that passage.

2.3.1. Diamagnetism and paramagnetism

Diamagnetism is an effect present in all materials, but often not noticeable due to its weak magnitude. When a magnetic field \mathbf{H} is applied, the electric charges in diamagnetic materials partially shield its interior from this applied magnetic field. This behaviour is in analogy with Lenz's law known from electromagnetism. When a magnetic field penetrates a current loop and changes its magnitude the current adapts in such a way that the magnetic field created, is opposed to the original field. To get a more quantitative understanding of this effect a quasi-classical approach, the Langevin formula, is presented. This treatment, although not

explicitly obeying quantum mechanics, is in agreement with the quantum mechanical results for the susceptibility of diamagnets.

Applying a magnetic field leads to a precession of the electrons with an angular frequency additional to the orbiting around the nucleus, present without applied field. The electron precession takes place with the so-called Larmor frequency

$$\omega = \frac{eB}{2m}. \quad (2.4)$$

Assuming that the electron current around the nuclei averages to zero before applying the field, then the field induced Larmor precession generates an electric current

$$I = (-Ze) \frac{1}{2\pi} \cdot \frac{eB}{2m}, \quad (2.5)$$

where Z is the number of orbiting electrons per nucleus. This current loop produces a magnetic moment (*current \times area of loop*)

$$\mu = -\frac{Ze^2B}{4m} \langle r_{\perp}^2 \rangle. \quad (2.6)$$

$\langle r_{\perp}^2 \rangle$ is the mean square of the electron's distance to the nucleus in the plane perpendicular to the applied field. For N atoms per unit volume and accounting for a spherical distribution of the electrons with a mean square radius $\langle r^2 \rangle$, the magnetic susceptibility per unit volume can then be written as

$$\chi = \frac{\mu_0 N \mu}{B} = -\frac{\mu_0 N Z e^2}{6m} \langle r^2 \rangle. \quad (2.7)$$

This result, with the simplification of fixed electron orbits, however reproduces the case of noble gases most accurately. In the case of solids, especially metals, with delocalized electrons it is obvious that this simple model reaches its limits. Nevertheless, based on these findings we can draw several conclusions. 1) Diamagnetism is present in all kinds of matter. 2) The susceptibility of a diamagnet is always negative, the magnitude however is very small and on the order of $\chi \approx 10^{-5}$. 3) Diamagnetism is not explicitly temperature dependent. Measured deviations can be assigned to temperature induced variations of $\langle r^2 \rangle$ 4) Superconducting materials show perfect diamagnetic behaviour with $\chi = -1$, the physics behind differ from the Langevin model and will be covered in Chapter 4.

Paramagnetism is based on magnetic moments present in the atoms of matter which get aligned when an external magnetic field is present and its contribution to magnetic susceptibility is positive. This means, while diamagnets try to expel applied fields (Lenz's law) and thus are repelled by these fields, paramagnets are attracted by magnetic fields. Paramagnetism is present in atoms and molecules with an uneven number of electrons (e.g. free alkali metal atoms, gaseous NO), free atoms with partly filled inner shells (e.g. Mn^{2+} , Gd^{3+}) and metals via its conduction electrons. The temperature dependence of a paramagnet's susceptibility, the Curie law, can be derived in a semi-classical way via equilibrium populations of a simple two state particle (e.g. single spin) in a magnetic field, this particle with no orbital moment in a magnetic field has the two energy levels $U = \pm\mu B$. Then a system has the equilibrium populations

$$\frac{N_1}{N} = \frac{\exp(\mu B/k_B T)}{\exp(\mu B/k_B T) + \exp(-\mu B/k_B T)}, \quad \frac{N_2}{N} = \frac{\exp(-\mu B/k_B T)}{\exp(\mu B/k_B T) + \exp(-\mu B/k_B T)} \quad (2.8)$$

where N_1 and N_2 are the population levels of the lower and upper level and the total number of particles $N = N_1 + N_2$. For a system with N particles the magnetization per unit volume is given by

$$M = (N_1 - N_2)\mu = N\mu \frac{\exp(\mu B/k_B T) - \exp(-\mu B/k_B T)}{\exp(\mu B/k_B T) + \exp(-\mu B/k_B T)} = N\mu \tanh(\mu B/k_B T), \quad (2.9)$$

for $\mu B/k_B T \ll 1$ and consequently $\tanh(\mu B/k_B T) \simeq \mu B/k_B T$ we obtain

$$M \simeq N\mu(\mu B/k_B T). \quad (2.10)$$

From the magnetization term just obtained, the susceptibility derives according to

$$\chi = \left(\frac{\partial M}{\partial B} \right) = \frac{N\mu^2}{k_B T}. \quad (2.11)$$

After obtaining the susceptibility of two-level ensembles in the next step this can be used to calculate the paramagnetic susceptibility of conduction electrons in metals. The susceptibility of most normal non-ferromagnetic metals does not show a temperature dependence as would be expected from Eq. 2.11, this has to do with the fact that in the case of electrons in a metal the Fermi-Dirac statistics have to be applied. Electrons in the Fermi sea can not necessarily align according to an applied magnetic field, because most orbitals, that is the ones below the Fermi level, are already occupied. Therefore only the fraction of electrons that have enough thermal energy to occupy the orbitals above the Fermi level in the range $k_B T$ can align accordingly and thus contribute to the metal's susceptibility. If only the fraction T/T_F , where T_F is the Fermi temperature of the metal, can contribute, then the susceptibility is given by

$$\chi = \frac{N\mu^2}{k_B T} \cdot \frac{T}{T_F} = \frac{N\mu^2}{k_B T_F}. \quad (2.12)$$

The paramagnetic susceptibility is on the order $\chi \approx 10^{-3}$ and thus outweighs the diamagnetic contribution in most cases. After having covered para- und diamagnetism, which only show magnetic order if induced by an external magnetic field we now turn to phenomena with intrinsic magnetic order.

2.3.2. Ferromagnetism and antiferromagnetism

The phenomena of ferromagnetism (FM) and antiferromagnetism (AF) (as well as ferrimagnetism) are very closely related regarding the underlying physics. We will start by discussing FM followed by applying these findings to the case of AF and ferrimagnetism mostly following [34, 38]. All three cases are depicted in Fig. 2.2 to visualize the spin order present in the solid.

In the case of ferromagnetism, materials show $\chi \gg 1$ with non-linear field dependence. A FM has a spontaneous spin order where magnetic moments align in parallel, resulting in a net magnetic moment even without an applied field. This order is moderated by the so called exchange interaction. The classical dipolar interaction between electrons in the solid can be excluded as underlying mechanism, because it is far too weak to cause this kind of order. A brief evaluation of the dipolar interaction energy between two magnetic moments with magnitude of Bohr's magneton μ_B at a distance $r = 2 \text{ \AA}$ confirms this. It is $U \sim \mu_0 \mu_B^2 / r^3 \sim 10^{-4} \text{ eV}$, this energy could explain magnetic order at 1 K, but not far above room temperature as is

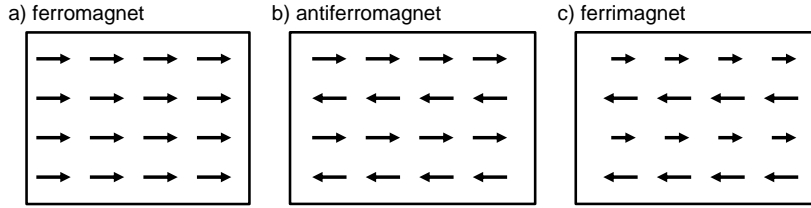


Figure 2.2. | Schematic arrangement of spins in a) ferromagnet, b) antiferromagnet and c) ferrimagnet.

observed. The actual mechanism is of quantum mechanical origin, based on the Pauli exclusion principle and will briefly be described. The energy of two interacting atoms i, j with electron spins $\mathbf{S}_i, \mathbf{S}_j$ can be described by the term

$$U = -2J\mathbf{S}_i\mathbf{S}_j. \quad (2.13)$$

The parameter J measures the strength of the exchange interaction depending on the spatial separation between the atoms and in the case of FM is positive. Due to the Pauli exclusion principle, two electrons in a solid can not occupy the same state. Therefore two electrons with parallel spin can not reside at the same place, with opposite spin however it is possible. The solid's electrostatic energy depends on the relative spin orientations and thus defines the exchange energy which is on the order of eV.

An important parameter related to FM is the exchange stiffness constant

$$A = \frac{nJS^2}{a} \quad (2.14)$$

with lattice constant a and number of atoms per unit cell n . It is a measure for the magnetic coupling and the difficulty for a given spin to deviate from the homogeneous magnetic state.

A further important parameter of a FM is its Curie temperature T_C . This temperature is material dependent and tells the boundary between FM state and transition to the paramagnetic state, i.e. loss of magnetic order. When a FM is heated above its T_C the thermal energy eventually overcomes magnetic order and the solid behaves paramagnetic until cooled again below T_C .

FM order at room temperature is found in the elements Fe, Ni, Co whose Curie temperatures are between 600 – 1000 K and a multitude of alloys like the ones relevant for this thesis FeCo and NiFe. As well as in rare-earth compounds like $\text{Nd}_2\text{Fe}_{14}\text{B}_{14}$ used for high performance applications. Soft alloys like FeSi find their application in transformer cores or electrical machines [1].

Central element of any magnetic solid is its hysteresis, i.e. the behaviour of its magnetization when a magnetic field is applied (Fig. 2.3). For high enough applied fields the magnetization does not change significantly anymore. All moments in the material are aligned with the external field and the saturation magnetization M_s is reached. For smaller fields the magnetization decreases, however for zero applied field the FM still shows some remaining magnetization. This magnetization, remaining for zero applied field, is called remanence M_r . Upon further reducing the applied field also the magnetization further reduces down to zero magnetization. The field necessary to generate zero magnetization in a ferromagnet is called the coercive field H_c . For applications the knowledge of H_c and H_r is important, because these parameters define the magnet's hardness and the energy dissipation per magnetization cycle.

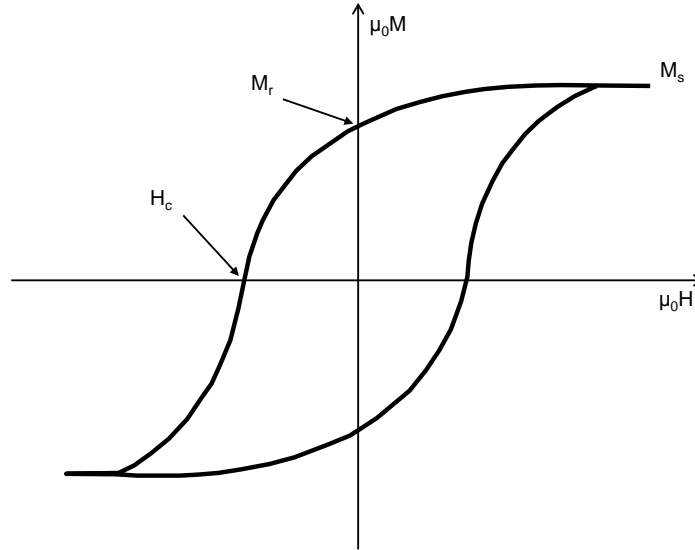


Figure 2.3. | Magnetization of a FM solid versus applied field.

Antiferromagnets show antiparallel alignment of the spins in the solid, cancelling each other out and thus leading to zero net magnetization. The underlying mechanism that induces this order is the same as for FM, but the exchange parameter J is negative here. Analogous there is a critical temperature above which the magnetic order is lost and the sample shows paramagnetic behaviour. This temperature is called Neél temperature T_N and is a material dependent constant. AF order is found in elements like Mn ($T_N = 96$ K), compounds like FeMn ($T_N = 510$ K) and it is very common among transition metal oxides like e.g. NiO, FeO ($T_N = 850$ K), Fe_2O_3 to name just a few. Included are some T_N to give an idea of its order of magnitude [39].

Ferrimagnets, like AF, have $J < 0$ leading to antiparallel alignment of the spins. Contrary to AF, ferrimagnets show a net magnetization. Ferrimagnets consist of two sub lattices each with different magnitude of magnetic moments causing the material to show non zero magnetic moment despite of the anti parallel alignment. As in the case of FM and AF, magnetic order is lost above a critical temperature T_c . Ferrimagnetism is found in ferrites like $\text{Ba}_2\text{Fe}_{12}\text{O}_{19}$ and $\text{Sr}_2\text{Fe}_{12}\text{O}_{19}$, magnetic garnets like e.g. YIG (Yttrium iron garnet) and oxides like Fe_3O_4 ($T_c = 856$ K). Especially due to their magnetic hardness the ferrites find applications in motors, actuators or holding devices [1].

2.4. Exchange bias

Exchange bias (EB) is an interface phenomenon typically observed between a FM and an AF layer. The signature effect is a shift of the hysteresis loop of the layered system along the field axis. Exchange bias was discovered in 1956 by Meiklejohn and Bean on Co fine particles with the surface oxide CoO [40, 41]. In a first attempt it was explained as a field dependent exchange anisotropy. In modern technology the effect found and still finds its application in magnetic recording media [42], spin valves and magnetic tunnel junctions [5, 43].

For description of the phenomena within this thesis we will restrict ourselves to a bilayer system of FM/AF because it is most relevant for this thesis and also most common. Information on other material systems like ferri/FM, AF/ferri, and others can be found in [44, 45]. Based on Fig. 2.4 an intuitive explanation for the EB is provided. For initialization the sample has to be brought to elevated temperature above T_N of the AF, but below the FM's T_C . Then a magnetic field is applied (here it is positive). This leads to the FM's spins aligning parallel to the external field. The AF however is disordered in its paramagnetic state due to the elevated temperature. The sample undergoes field cooling below T_N . The AF spins located

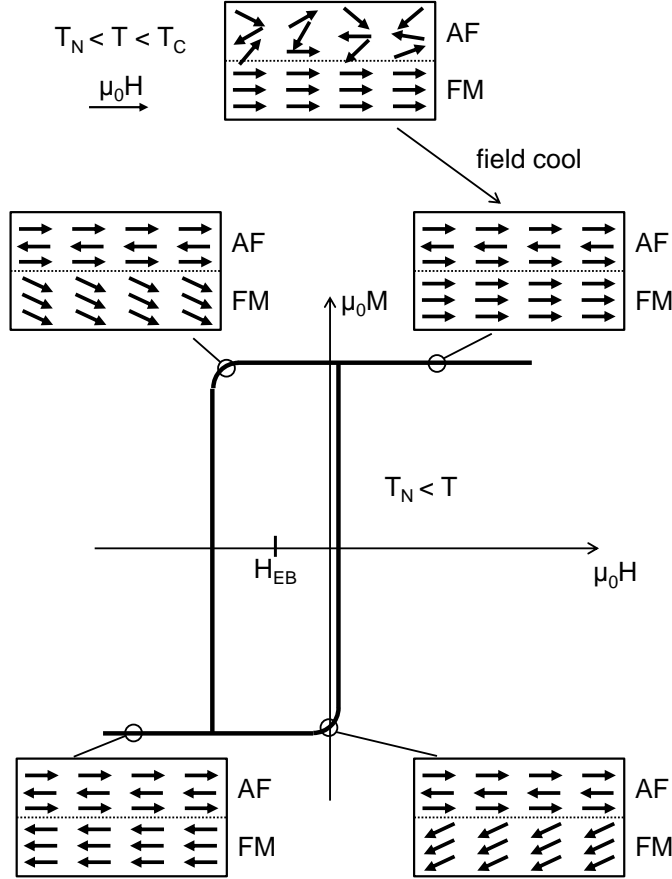


Figure 2.4. | Sketch of the spin configuration of an exchange-biased AF/FM bilayer during initialization and successive hysteresis loop.

directly at the interface couple to FM spins in direct proximity of the interface and align in parallel to them. Based on this, the remaining AF spins order in alternating way that their net magnetization is zero as expected for AF.

Now, when reversing the applied field at low temperature, AF spins remain fixed due to their high anisotropy. The FM spins however follow the field. The FM reversal is hindered, because the fixed AF spins exert a torque on the FM spins at the interface. This torque is counteracting the external field and has to be overcome. For high enough fields, higher than the magnitude needed to reverse the plain FM layer, the FM spins eventually reverse.

When sweeping back the magnetic field, the contrary can be observed. Now the field is parallel to the AF spins at the interface. Consequently the reversal of FM is now supported by the torque exerted by AF on the FM spins at the interface. Magnetization reversal happens at much lower fields than before, also lower than without AF interfacing the FM layer. This described mechanism is the origin of the hysteresis' shift along the field axis. The direction of the shift is determined by the direction of the field applied during the field cooling and can be chosen accordingly.

Depending on the AF's anisotropy two limiting cases can be defined. The first case with very high anisotropy, i.e. fixed AF spins, during field reversal was just described and leads to a shift of the hysteresis loop.

The second case for very low anisotropy behaves very differently. In the case of low AF anisotropy the spins do not remain fixed, but together with the FM spins follow the applied field. If this is the case, no loop shift is observed. Instead, an increase of the coercivity is measured, meaning that the hysteresis loop only broadens. This symmetric loop broadening can be associated with the extra energy needed to irreversibly switch the AF's orientation. In this case the hysteresis loop is symmetric, because no preferential direction relative to the applied field exists anymore. Most of the time, in a real system a mixture of both, broadening and shifting, is observable. The main reasons are structural defects and grain size distribution which lead to a local variation of the AF's anisotropy.

However, the mechanism described in the above paragraph is an intuitive picture, which can not predict or explain all observations experimentally made. To solve this, different theoretical approaches have been undertaken. Nonetheless, due to the complexity and the fact that the effect is strongly dependent on the experimentally hardly accessible interface, none of these approaches provides a general explanation of the phenomena. More details on the difficulties and the different theoretical approaches is discussed in reviews [44–46].

Understanding an EB system's temperature dependence is of great importance and directly relates to the two above mentioned limiting cases. Starting from very low temperature, with elevating temperature a reduction of H_E and simultaneously an increase of H_c can often be observed. This trend holds until, at a temperature defined as blocking temperature T_B , the exchange field H_{EB} goes to zero. Furthermore, before T_B is reached, a maximum of H_c is observed [45, 47]. Following above arguments, a rise in temperature is directly related to a decrease of the AF's anisotropy. The observed temperature dependence can be related to the AF's morphology. There is a wide spread in T_B , at which H_{EB} becomes zero, compared to the AF's Néel temperature. This variance is related to grain size and thickness of the AF layer. For single crystal and large grain films, $T_B \approx T_N$ is observed [48]. However, for small grains and thin films $T_B \ll T_N$ can be observed [49, 50]. This strong reduction of T_B is the case, when grain size and film thickness are close to or below critical AF system parameters [49]. Statistical distribution of grain sizes in turn, can also lead to a distribution of T_B rather than a sharply defined temperature [51, 52].

A further important effect of EB systems is called the training effect, which is the dependence on the number n of measured hysteresis loops. With increasing n , a reduction of H_{EB} and H_c is observed. This effect is divided into two regimes that seem to be caused by different underlying mechanisms. The large change in H_{EB} from first to second loop is assigned to the symmetry of the AF layer. Numerical simulations suggest the existence of multiple AF easy axes, which then relax into collinearity after the first loop [53]. For the successive loops it has been found, that the evolution of H_{EB} can be described by $H_{EB}^n - H_{EB}^\infty \propto 1/\sqrt{n}$, where H_{EB}^n and H_{EB}^∞ are the exchange bias fields at loop number n and in the limit of infinite loops respectively [54].

The training effect is also dependent very much on the AF layer's morphology. In single crystal samples the training effect is negligible. In polycrystalline samples with small grain sizes it is very pronounced. An explanation for the dependence $H_{EB}(n)$ is, that the AF at the interface undergoes configurational rearrangements of AF moments or domains [55].

2.5. Magnetism of small particles

In this section an extension of the basics on ferromagnetism is given in the light of particles on the micro- and nanoscale. The chapter will mostly follow Guimãraes and Aharoni [36, 56]. The reduced size leads to some peculiarities, because sample dimensions can reach down to length scales intrinsic to the magnetic material. The reversal of small magnetic particles will be discussed in the light of the Stoner-Wohlfarth model and its limitations, followed by a brief overview on the influence of tubular geometry on magnetic behaviour.

2.5.1. Interactions and characteristic length scales in magnetic materials

To describe magnetism on the micro- and nanoscale, the total energy functional of the magnet is the starting point. Formally, by minimizing the energy functional with respect to the orientation of the magnetic moment, the magnetization is obtained. This knowledge allows insight into e.g. the magnet's domain formation, onset of magnetization reversal or coercivity. The energy functional for a defect free, ideal magnet is given by

$$E = E_{ex} + E_{ms} + E_Z + E_A + E_\sigma. \quad (2.15)$$

The different energy contributions will now be described in the following.

The exchange energy E_{ex} arises due to the quantum mechanical interaction between the indistinguishable electrons in the magnet. E_{ex} originates from the exchange interaction responsible for magnetic ordering in a solid as described before. It causes spins to align in parallel in a ferromagnet. By summing over nearest neighbour spin pairs, the energy can be expressed as

$$E_{ex} = -\frac{1}{2} \sum_{i,j} J_{i,j} \mathbf{S}_i \mathbf{S}_j \quad (2.16)$$

with exchange constant J and spin operators \mathbf{S} . In the case of uniform magnetization, E_{ex} is at a minimum.

The magnetostatic energy E_{ms} is caused by interaction of the sample's magnetization and its own stray field. It is thus sometimes also termed stray field, dipolar or magnetic self-energy. E_{ms} is given by the volume integral over the sample's magnetization \mathbf{M} in its demagnetizing field \mathbf{H}_d

$$E_{ms} = -\frac{1}{2} \mu_0 \int_V \mathbf{H}_d \cdot \mathbf{M} dV. \quad (2.17)$$

A special case, where E_{ms} is relatively easy to determine are ellipsoidal particles. Here \mathbf{H}_d is constant throughout the volume [56] and we obtain

$$E_{ms} = -\frac{1}{2} \mu_0 M_s^2 V (D_\perp \sin^2(\theta) + D_\parallel \cos^2(\theta)). \quad (2.18)$$

It is μ_0 the vacuum permeability, M_s the sample's saturation magnetization and V its volume. The angle between magnetic field and ellipsoid's rotational symmetry axis is θ and the demagnetization factors along and perpendicular to the ellipsoid's symmetry axis are D_{\parallel} , D_{\perp} . For more information on demagnetization factors see chapter 3.

The Zeeman energy E_Z , in contrast, has its origin in the interaction of an external magnetic field H with the particle's magnetization \mathbf{M} . It is given by

$$E_Z = -\mu_0 \int_V \mathbf{H} \cdot \mathbf{M} dV. \quad (2.19)$$

The magnetocrystalline anisotropy E_A is defined by the direction of magnetization relative to the crystal's structural axes. Its contribution consequently depends on the solid's crystal structure and for non-crystalline samples amounts to zero [57].

The interaction of a solid's magnetization and the mechanical strain present in the material provides a further contribution to the total magnetic energy. Magnetoelastic energy E_{σ} depends on crystalline structure and vanishes for polycrystalline or amorphous materials like the ones investigated in this thesis [57].

While working out this energy functional some prefactors that can be assigned to characteristic material's parameters and give an idea of relevant length scales in micromagnetism.

The exchange length l_{ex} of a ferromagnet determines the scale below which exchange dominates over magnetostatic effects. It is defined as

$$l_{ex} = \sqrt{\frac{2A}{\mu_0 M_s^2}} \quad (2.20)$$

with exchange stiffness A , vacuum permittivity μ_0 and saturation magnetization M_s .

In case of multiple domains present, the width of a domain wall can be expressed by the material's stiffness A and its anisotropy K

$$\delta_0 = \pi \sqrt{\frac{A}{K}}. \quad (2.21)$$

If a magnet's spatial dimensions are below a certain critical diameter D_{cr} it is energetically more favourable to only form a single domain instead of a multi-domain state. This critical diameter is expressed by already known parameters as

$$D_{cr} = \frac{72\sqrt{AK}}{\mu_0 M_s^2}. \quad (2.22)$$

For Ni as a relevant example these parameters in units of 10^{-9}m are $D_{cr} = 53.6$, $\delta_0 = 123$, $l_{ex} = 7.64$ [56].

2.5.2. Stoner-Wohlfarth model and beyond

A relatively simple but effective model to describe magnetism in small particles was developed by Stoner and Wohlfarth in 1948 [58]. The model assumes a homogeneously magnetized particle in single domain state and in the shape of an elongated, unstrained ellipsoid placed in a homogeneous magnetic field (Fig.2.5a)). Prerequisite for homogeneous magnetization is

the presence of exchange interaction that keeps the magnetic moments aligned without spatial dependence. Because all magnetic moments reverse their magnetization in unison, one often also speaks of a "macro-spin" behaviour. This simplifies the model drastically, because the exchange energy is constant and goes to zero when minimizing the total energy. Due to the simplifications, the only interactions considered are Zeeman interaction, shape and crystalline anisotropy. The total energy, which is the starting point for all predictions this model provides,

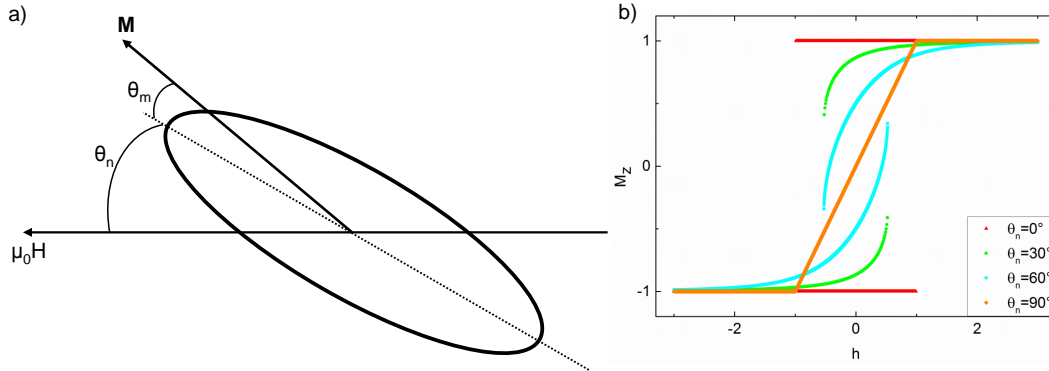


Figure 2.5. | a) Magnetic ellipsoid in an applied field. The ellipsoid's easy axis is marked with a dashed line. The angle between applied field and magnetization \mathbf{M} is $(\theta_n + \theta_m)$ and the angle between magnetic field and easy axis is θ_n . b) Magnetization of an ellipsoidal magnet versus applied field for different spatial orientations of the magnet given by the angle θ_n .

is

$$E = KV \sin^2(\theta_m) - \mu H \cos(\theta_n + \theta_m) \quad (2.23)$$

with volume V , magnetic moment $\mu = \mu_0 M_s V$ and anisotropy constant K . By minimizing this expression, predictions about hysteresis and coercivity depending on the spatial orientation of the magnet relative to an applied magnetic field are possible. One main result obtained within the framework of this model is shown in Fig. 2.5b) which depicts the magnet's hysteresis depending on its relative orientation to the applied field. For a magnet with easy axis oriented parallel to the field, a bistable, square hysteresis with irreversible switching is predicted that evolves with an increasing amount of reversible switching into a diagonal line for the case of a perpendicular orientation of the easy axis relative to the applied field. The case for a magnet with easy axis aligned parallel to the applied field will be solved explicitly in chapter 3. What makes this model particularly useful is the fact, that it can also be applied to non-ellipsoidal geometries. It can be shown, that a single-domain particle of arbitrary shape can be modelled by a suitably chosen ellipsoid [11].

The model of Stoner and Wohlfarth presented here in excerpts, though simple, is able to make valid predictions for real particles [59–61]. There are however limitations and cases not included in this model that shall be briefly discussed in the following.

One common challenge that goes beyond the Stoner-Wohlfarth model is describing the reversal of an assembly of magnetic particles interacting with each other. These interactions can be of dipolar, exchange or Ruderman-Kittel-Kasuya-Yoshida (RKKY) nature. The modifications to the magnetic system regarding relevant parameters to describe the magnetization reversal and hysteresis need more elaborate modelling and understanding of underlying principles and are beyond our scope [56].

Challenges in precise modelling of a magnet's behaviour are not only faced in ensembles, but also for single particles. Due to the magnetization in the Stoner-Wohlfarth model being uniform throughout the sample and the moments being tightly held in parallel due to exchange interaction, magnetization reverses in unison. This ideal situation does not hold any more for larger samples and inhomogeneous magnetization. In such non-ideal samples magnetic moments do not necessarily remain parallel and reversal has been identified to take place in different modes [62]. The three different modes are shown in Fig. 2.6 for the case of cylindrical shapes. The most common incoherent reversal mode is curling (2.6b)). In this mode the

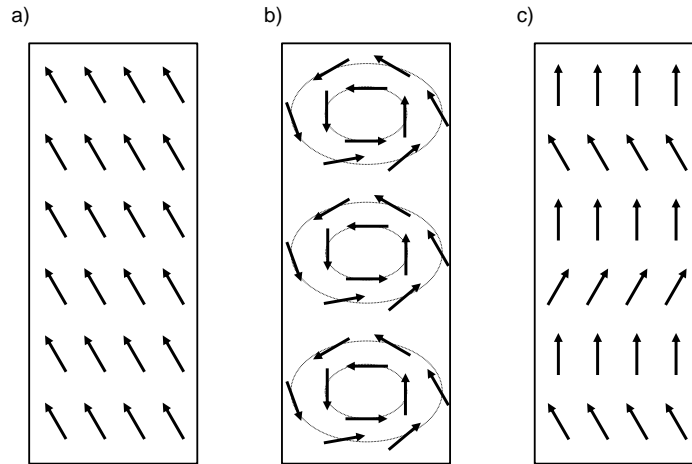


Figure 2.6. | Proposed reversal modes for cylindrical shaped particles, with a) coherent rotation b) curling and c) buckling.

magnetic moments align tangential to the cylinder's surface plane for magnetization reversal. Less common is the buckling mode for magnetization reversal. As visualized in Fig. 2.6c), the magnetic moments show a periodic dependence along the cylinder's long axis for reversal. The third reversal method is the uniform rotation of the magnetic moments, shown in 2.6 a) and already described in the frame of the Stoner-Wohlfarth model. Theoretical description of the newly introduced reversal modes is difficult due to the inhomogeneous magnetization and thus largely restricted to simple geometric shapes. Still it is possible to make predictions about nucleation fields (the field necessary to start reversal) and which reversal mode to expect depending on geometric parameters (e.g. diameter in the case of a cylinder).

The curling mode is of special interest to this thesis, because it provides motivation to investigate magnetic nanotubes in general. It has been shown in simulations, that during the reversal of a Ni cylinder, along the center axis a singularity occurs [9]. This singularity is known as Bloch point, close to this point no direction can be assigned to the solid's magnetization meaning that any direction is present.

This Bloch point can be avoided when moving to tubular structures that support radial spin configuration, but avoiding the singularity. In [12] detailed analytical and numerical studies of the reversal of tubular magnetic structures have been conducted. It is shown that reversal takes place by domain wall nucleation and propagation along the tube. Reversal can take place by propagation of a vortex domain wall or transversal domain wall, which is dependent on geometric parameters like the tube's radius and the ratio of its outer and inner radius (i.e. the tube's thickness). Both reversal modes are depicted in Fig. 2.7a),b). The reversal of

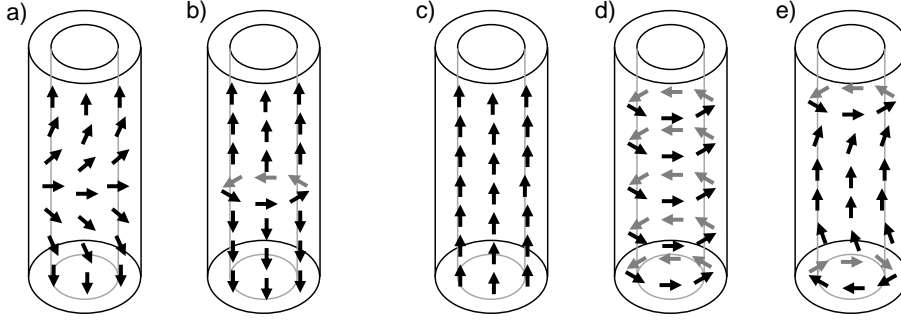


Figure 2.7. | Magnetization reversal modes for tubular magnetic structures showing reversal via a) transversal domain wall and b) vortex domain wall. Possible stable states the magnetic moments relax into in applied field are c) axial state, d) vortex state and e) mixed state.

tubular structures is also of interest, because very high domain wall velocity and robustness has been predicted making it suitable for future memory or logic devices [10, 13, 63]. Apart from the reversal mechanism, also phase diagrams for the magnetic tube's final state have been investigated. It has been proposed that, depending on the geometric parameters length and radius, three stable configurations are possible. The axial state, where all spins are axially aligned as shown in Fig. 2.7c). The mixed state, which supports axially aligned spins along the tube and curling at the tubes ends to reduce stray field (Fig. 2.7e)). In the proposed vortex state, all spins are radially aligned (Fig. 2.7d)) leading to flux closure and consequently vanishing stray field.

2.6. Review of experimental techniques

There is a multitude of experimental techniques established, that provide insight into different aspects of magnetic solids. The techniques of dynamic cantilever and nanoSQUID magnetometry, which are most relevant to this thesis are just two among many and will be described later on in detail. Therefore, this subsection provides a brief overview of some of the different techniques and their capabilities.

To investigate magnetic solids on the atomic scale, diffraction methods using neutrons or X-rays are used. Single crystal or crystalline powder samples are irradiated with X-rays or neutrons with wavelengths on the order of the lattice constant. Interference of the scattered waves follows Bragg's law, however the scattering mechanism for neutrons and X-rays differs. Scattering of X-rays occurs by interaction with atomic nuclei or electrons, neutrons scatter from the magnetic moments of electrons. X-rays are preferably used to unravel structural properties, while neutrons are also able to provide information on magnitude and direction of magnetic moments in a unit cell [64].

To conduct element specific investigations spectroscopic methods like X-ray absorption spectroscopy are frequently used [65]. Access to hyperfine interaction is conveniently achieved using nuclear magnetic resonance (NMR) [66].

X-ray magnetic circular dichroism (XMCD) is a method that relies on the difference in absorption of circular left and circular right polarized X-rays impinging on a magnetic sample [67]. This method is able to determine spin and orbital momentum of unpaired electrons in atoms [68].

To obtain information of magnetization on domain-scale, different techniques based on X-ray, optical light as well as scanning probe methods are available.

Applying XMCD analysis in a surface sensitive photoemission electron microscope (PEEM), is a valuable tool to image magnetic domains in samples [69–71].

Exploiting magneto-optical effects employing linearly polarized visible light, emitted by a laser, is a powerful means to image magnetic domains. Two similar effects, the Faraday and the Kerr effect are distinguished here [72]. The Faraday effect leads to a rotation of the plane of polarization of linearly polarized light when passing through a magnetic sample. It is for example used to image domains in transparent ferrimagnets [73]. The magneto-optical Kerr effect (MOKE) is very similar to the Faraday effect, but works in reflection mode and thus demands for samples with clean surfaces. Rastering across a surface, the technique is capable of imaging magnetic domains and their dynamics [74]. MOKE is also used to record hysteresis loops of magnetic samples [75]. This is achievable when the beam of light is much larger than the magnetic domains and thus the measurement averages over a larger part of the sample. Although powerful and very sensitive imaging techniques, measurements basing on Faraday and Kerr effect are not capable of measuring absolute values of magnetization [1].

Instead of X-rays or visible light, also electrons can be used to image magnetic domains with Lorentz microscopy, which is an extension to regular transmission electron microscopy (TEM). In Lorentz microscopy, the analysis of electrons that are deflected by the Lorentz force $e\mathbf{v} \times \mathbf{B}$ when passing through a magnetic sample allows to image magnetic domains [76, 77]. The spatial resolution is very high and can reach down to atomic scale resolution. This technique however is restricted to samples prepared as thin foils [1].

An extension to this method is electron holography [78]. In electron holography the electron wave's phase information is analyzed to obtain information on magnetic domains and magnetic field lines emanating from the sample [79].

Various scanning probe methods are available to investigate magnetic samples and provide information on their magnetic structure on the domain-scale and below.

The most established technique is magnetic force microscopy (MFM). Similar to atomic force microscopy (AFM), a cantilever equipped with a sharp magnetic tip is scanned across a surface [80]. Due to the magnetic tip, the cantilever is sensitive to gradients of the stray fields emerging from the investigated sample. MFM is surface sensitive and has demonstrated its ability to image at the sub-micron level early on [81, 82] with application to magnetic recording media [83].

Another scanning probe method uses the relatively new system of nitrogen vacancy (NV) centers embedded in diamond. Using a cantilever, functionalized with such an NV, imaging magnetic domains and also determining a domain wall's internal structure was demonstrated [84, 85].

Scanning micro-SQUID susceptometers, where a pick-up coil is scanned across mesoscopic samples have proven its capability for spatially resolved experiments [86].

A very new technique is the scanning SQUID-on-tip. The SQUID is evaporated to the apex of a glass tip and has diameters down to 46 nm. It can resolve Abrikosov vortices spaced 120 nm apart and in principle is sensitive to a single electron spin [87, 88].

Apart from radiation based and scanning probe techniques also transport measurements provide information on magnetization of various kinds of samples.

In anisotropic magnetoresistance (AMR) the magnetic field dependence of a magnet's resistance is analyzed [89]. In AMR, the electrical resistance depends on the angle between the directions of electrical current and magnetization. This technique is suitable for thin film sam-

ples and most important in the light of this thesis also on individual ferromagnetic nanowires and -tubes [4, 21, 22, 27, 90].

All methods mentioned up to here, despite their diverse capabilities, have one thing in common—their inability to determine an absolute value for the sample’s magnetization. A way to determine this number is by bulk magnetization measurements detecting stray fields generated by the investigated sample or forces between sample and applied field [35, 91].

In an alternating gradient force magnetometer (AGFM) the magnetic sample is attached to a vibrating support rod and an alternating field gradient is applied additional to a homogeneous magnetic field to then detect the rod’s oscillation amplitude. Such a setup, employing lock-in detection achieves sensitivities on the order of 10^{-10} A/m [91]. It is used for thin film samples with film thickness down to a few nanometres.

Two methods that detect the magnetic sample’s stray field are the SQUID magnetometer and the vibrating sample magnetometer (VSM). In VSM the sample is attached to a rod that vibrates at a given frequency between two pick-up coils. This vibration of the sample in turn induces a voltage in the coil which is then detected. The sensitivity of VSM is on the order of 10^{-9} A/m [91].

In a SQUID magnetometer the magnetic sample is placed inside a superconducting pick-up loop which is then read-out by a SQUID. Compared to VSM a SQUID magnetometer is by two orders of magnitude more sensitive [91].

3. Torque Magnetometry

3.1. Introduction

Cantilever torque magnetometry provides an integral measurement that averages over the whole volume of the magnetic sample that is studied. In general a magnetic sample is mounted on the tip of a cantilever which is then placed in a homogeneous magnetic field \mathbf{H} . The sample's magnetic moment $\boldsymbol{\mu}(\mathbf{H})$ together with the applied field exerts a torque $\boldsymbol{\tau} = \boldsymbol{\mu} \times \mathbf{H}$ on the cantilever. Generally there are three modes that can be distinguished. 1 - measuring a constant deflection of the cantilever in a static or low frequency field, 2 - measuring the cantilever frequency in a static field (this is referred to as dynamic cantilever magnetometry (DCM) and is the mode used in this thesis), 3 - measuring the resonant cantilever displacement by applying a magnetic field at the cantilever's resonance frequency [92].

Dynamic cantilever magnetometry is an elegant method to study a magnet, because it is minimally invasive. The method avoids perturbation of the sample's magnetization by currents as used in transport measurements, intense illumination or inhomogeneous magnetic fields. Solely exposure to a static magnetic field is necessary, the cantilever read-out is not interfering with the magnetic sample at all. One drawback however, is the inability to access magnetization dynamics since the method is limited to the cantilever's resonance frequency which is on the order of kHz and thus well below relevant time scales. Hence, DCM data always corresponds to magnetization being in equilibrium.

DCM measures the cantilever resonance frequency's dependence on the applied field $f(H)$. To be able to analyze this data further and draw conclusions about the sample's magnetization, in the following an analytical model will be presented. The model is based on the Stoner-Wohlfarth model describing a magnet's behaviour and treating the cantilever as simple harmonic oscillator.

3.2. Dynamic cantilever magnetometry (DCM)

The cantilever can be treated as harmonic oscillator and its equation of motion is given by

$$m_e \ddot{x} + \Gamma \dot{x} = \tau/l_e. \quad (3.1)$$

It is m_e and l_e the cantilever's effective mass and length, Γ is its mechanical dissipation and τ is a torque exerted on the cantilever. Starting from this equation of motion, in the next step the torque will be expressed in terms of the energy of the magnet-tipped cantilever.

The total energy of a magnet on cantilever system is given by the mechanical energy term and the magnetic energy E_m . E_m for now will be treated as general term and only later specified, furthermore we assume the Si cantilever and the epoxy to fix the magnet as completely non-magnetic. The mechanical energy is that of a simple harmonic oscillator with spring constant

k_0 where displacement is expressed by oscillation angle θ_c and effective cantilever length l_e using small angle approximation ($\theta_c \ll 1$). It is

$$E = \frac{1}{2}k_0(l_e\theta_c)^2 + E_m. \quad (3.2)$$

As shown in Fig. 3.1a) the cantilever is aligned along \hat{z} and its axis of rotation is along \hat{y} . The cantilever deflection θ_c depends on the torque exerted on the cantilever along \hat{y} and is given by $\tau = -\partial E/\partial\theta_c$. Since we operate in the small angle regime, the torque can be obtained by expanding E to first order around the cantilever's equilibrium angle $\theta_c = 0$ and obtain

$$\tau = - \left(\frac{\partial E_m}{\partial\theta_c} \Big|_{\theta_c=0} \right) - \left[k_0 l_e^2 + \left(\frac{\partial^2 E_m}{\partial\theta_c^2} \Big|_{\theta_c=0} \right) \right] \theta_c. \quad (3.3)$$

The obtained torque is composed of two components. The first term corresponds to a constant cantilever deflection, which is not what we are going to measure. Rather than measuring the cantilever's deflection we are sensitive to changes in the cantilever's spring constant that eventually lead to frequency shifts. This change of spring constant is mathematically expressed by the term in square brackets. The above expression for the torque can now be inserted in Eq. 3.1 and leads to

$$m_e\ddot{\theta}_c + \Gamma\dot{\theta}_c + \left[k_0 + \frac{1}{l_e^2} \left(\frac{\partial^2 E_m}{\partial\theta_c^2} \Big|_{\theta_c=0} \right) \right] \theta_c = -\frac{1}{l_e^2} \left(\frac{\partial E_m}{\partial\theta_c} \Big|_{\theta_c=0} \right). \quad (3.4)$$

In the following steps the damping part will be neglected. This is justified because the cantilevers used in the experiments show very high quality factors $Q > 20 \times 10^3$. Solving Eq. 3.4 leads to the following term for the angular resonance frequency of the cantilever

$$\omega = \sqrt{\frac{k_0}{m_e} + \frac{1}{m_e l_e^2} \left(\frac{\partial^2 E_m}{\partial\theta_c^2} \Big|_{\theta_c=0} \right)} \quad (3.5)$$

This equation can be rewritten to provide the frequency shift $\Delta\omega = \omega - \omega_0$ we are interested in and using the definition $\omega_0 = \sqrt{k_0/m_e}$:

$$\Delta\omega = \omega_0 \left(\sqrt{1 + \frac{1}{m_e \omega_0^2 l_e^2} \left(\frac{\partial^2 E_m}{\partial\theta_c^2} \Big|_{\theta_c=0} \right)} - 1 \right) \quad (3.6)$$

With the second term in the square-root being very small, the square-root can be expanded using $\sqrt{1+x} \approx x/2 + 1$ for $x \ll 1$ to

$$\Delta\omega = \frac{\omega_0}{2k_0 l_e^2} \left(\frac{\partial^2 E_m}{\partial\theta_c^2} \Big|_{\theta_c=0} \right). \quad (3.7)$$

Using the relation $\omega = 2\pi f$ Eq. 3.7 can be transformed in terms of the measured frequency shift to

$$\Delta f = \frac{f_0}{2k_0 l_e^2} \left(\frac{\partial^2 E_m}{\partial\theta_c^2} \Big|_{\theta_c=0} \right). \quad (3.8)$$

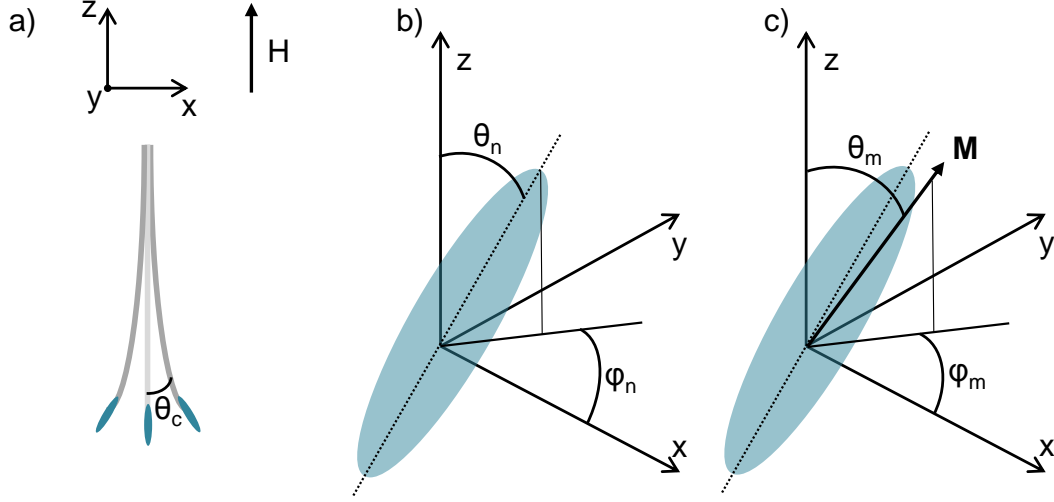


Figure 3.1. | a) Cantilever with attached ellipsoidal magnet at its tip. The axis of rotation is along \hat{y} and the angle θ_c determines the deviation from the equilibrium position. The magnetic field is along \hat{z} . b) Orientation of the ellipsoidal magnet with easy axis (dashed line) along its long axis. The magnet's spatial orientation is determined by polar and azimuthal angles φ_n and θ_n . c) Orientation of the magnetization vector relative to the magnet's easy axis is determined by the polar and azimuthal angles φ_m and θ_m .

The measured frequency shift can thus be expressed in terms of intrinsic cantilever properties and the curvature of the magnetic energy with respect to rotations of the magnetic sample around the cantilever oscillation axis. This general result can be applied to a variety of magnetic samples and geometries.

For actual evaluation of Eq. 3.8 the magnetic energy term has to be specified. The NTs investigated in this thesis can be approximated as single-domain magnets. The framework to treat this kind of idealized particle is the Stoner-Wohlfarth model introduced in chapter 2.5.2. The particles are modelled as prolate ellipsoid with uniform magnetization. Their demagnetizing field is $H_d = -D\mathbf{M}$ with magnetization \mathbf{M} and tensor D consisting of the diagonal elements D_x, D_y, D_z which are the demagnetization factors describing the particle's shape anisotropy. For the case of the NTs investigated, the shape of a hollow cylinder is a suitable approximation. For the tube's long axis along \hat{z} and the large aspect ratios present the following demagnetization factors are obtained $D_x = D_y \equiv D_\perp \approx 0.5$ and $D_z \equiv D_\parallel \approx 0$. In reality we find deviations on the order of 10^{-3} from these values. Based on this, we only consider shape-induced uniaxial anisotropy along the tube axis and define an effective anisotropy $D_u = D_z - D_x$. For more details on demagnetization factors see [37, 93] and references therein.

The spatial orientation of the particle can generally be described by the spherical coordinates θ_n and φ_n as depicted in Fig. 3.1b). However, for the sake of simplicity we choose the special case $\theta_n = \varphi_n = 0$ which corresponds to a particle aligned along \hat{z} and is the case for all experiments presented in this thesis. Consequently the direction of the particle's easy-axis \hat{n}

is also along \hat{z} . As depicted in Fig. 3.1c), the magnetization \mathbf{M} of the "macro-spin" is also described in spherical coordinates

$$\mathbf{M} = M_s \begin{pmatrix} \sin \theta_m \cos \varphi_m \\ \sin \theta_m \sin \varphi_m \\ \cos \theta_m \end{pmatrix}, \quad (3.9)$$

with the particle's saturation magnetization M_s . Because the magnetization is confined to the plane defined by the particle's easy axis and the direction of magnetic field, a further simplification used is $\varphi_m = 0$.

In accordance to the assumptions made by the Stoner-Wohlfarth model, given in chapter 2.5.2 the magnetic energy E_m is given by the Zeeman and the anisotropy energy

$$E_m = -\mu_0 V \mathbf{M} \cdot \mathbf{H} + \frac{1}{2} \mu_0 D_u V (\mathbf{M} \cdot \hat{n})^2, \quad (3.10)$$

with vacuum permeability μ_0 , particle volume V and effective demagnetization factor D_u . To find the particle's equilibrium magnetization the magnetic energy has to be minimum and fulfil the conditions

$$\frac{\partial E_m}{\partial \theta_m} = 0 \quad \text{and} \quad \frac{\partial^2 E_m}{\partial \theta_m^2} > 0. \quad (3.11)$$

Deriving E_m and applying the geometric simplifications, we obtain

$$\frac{\partial E_m}{\partial \theta_m} = -\mu_0 V M_s H \sin(\theta) - \mu_0 V D_u M_s^2 \cos(\theta_m) \sin(\theta_m). \quad (3.12)$$

By defining a reduced magnetic field $h = \frac{H}{M_s D_u}$ the above equation can be rewritten to

$$\frac{\partial E_m}{\partial \theta_m} = \sin(\theta_m)(h + \cos(\theta_m)). \quad (3.13)$$

The term equals zero and thus fulfills the first condition indicated in Eq. 3.11 in the following cases

$$\theta_m = 0, \quad \theta_m = \pi, \quad \theta_m = \arccos(-h) \quad (3.14)$$

The first two solutions refer to the magnetization aligning along $\pm \hat{z}$. The third solution refers to a special case not relevant for this thesis and will thus be neglected in the following. To verify the first solutions obtained, the second derivative of E_m is used as given by

$$\frac{\partial^2 E_m}{\partial \theta_m^2} = 2 \cos^2(\theta_m) + h \cos(\theta_m) - 1. \quad (3.15)$$

The solutions obtained in Eq. 3.14 put in this equation fulfill the second condition stated in Eq. 3.11 in the following cases. It is $\theta_m = 0$ for $h > -1$ and $\theta_m = \pi$ for $h < 1$. For $|h| > 1$ the solution is unique, but in between both orientations of magnetization are valid solutions. The solution obtained here is the one of a square hysteresis with switching field h .

Having worked out the magnetic energy we can go back to applying these results to the particle on cantilever to further analyze the measured frequency shift. Treatment will restrict to two limiting cases presented in the following subsections.

3.2.1. The high-field limit

The high field limit is of particular interest to characterize the magnetic particle's saturation magnetization M_s and its anisotropy. Working at fields for which $H \gg D_u M_s$ is an effective way to probe the particles anisotropy energy.

When high fields are applied, the particle's magnetization is forced to align in parallel to the field ($\mathbf{M} \parallel \mathbf{H}$). Therefore the first term in Eq. 3.10 is constant with respect to θ_m

$$E_m = -\mu_0 V M_s H + \frac{1}{2} \mu_0 D_u V M_s^2 \cos^2(\theta_c). \quad (3.16)$$

Forming the second derivative leads to

$$\frac{\partial^2 E_m}{\partial \theta_c^2} = -\mu_0 D_u V M_s^2 (\cos^2(\theta_c) - \sin^2(\theta_c)). \quad (3.17)$$

This term can now be inserted in Eq. 3.8 and allows analysis in the light of the cantilever's frequency shift Δf which we can measure. After further simplification, by taking $\theta_c = 0$, the frequency shift approaches a horizontal asymptote in the limit of high magnetic fields which is given by

$$\Delta f = \frac{f_0 \mu_0 V}{2 k_0 l_e^2} M_s^2 D_u. \quad (3.18)$$

By fitting this asymptote to measured high field data and setting parameters determined beforehand, the magnet's saturation magnetization M_s can be obtained.

3.2.2. The low-field limit

The low-field limit is of special interest for this thesis, because the nanoSQUID used only allows operation at moderate magnetic fields. A thorough analysis of the low field data obtained by cantilever magnetometry is crucial to fully exploit the duality of the setup and being able to compare nanoSQUID and cantilever data.

In the limit of low fields ($H \ll D_u M_s$), the magnet's shape anisotropy dominates E_m and ensures that \mathbf{M} remains parallel or antiparallel to the magnet's easy-axis. Considering this, we obtain

$$E_m = -\mu_0 V M_s H \cos(\theta_c) + \frac{1}{2} \mu_0 D_u V M_s^2. \quad (3.19)$$

The second derivative with respect to θ_m then is

$$\frac{\partial^2 E_m}{\partial \theta_c^2} = \mu_0 V H M_s \cos(\theta_c), \quad (3.20)$$

where $M_s \cos(\theta_c)$ is the magnetization's z -component M_z . Inserting this into Eq. 3.8 the frequency shift is described by

$$\Delta f = \frac{f_0 \mu_0 V}{2 k_0 l_e^2} M_z. \quad (3.21)$$

Solving this equation for M_z allows direct determination of the z -component of the magnetization averaged over the whole magnet by measuring the frequency shift. We obtain

$$M_z = \frac{2 k_0 l_e^2}{f_0 \mu_0 V H} \Delta f. \quad (3.22)$$

4. Superconducting Quantum Interference Device (SQUID)

4.1. Introduction

Superconductivity can be seen as the text-book example for a macroscopic quantum effect, where the mechanism is governed by quantum mechanics but the effect can be measured on a macroscopic scale. The discovery in 1911 by H. K. Onnes was only possible due to the previous technological achievement to liquefy Helium and thus allow cooling of samples close to absolute zero. This fascinating effect is the basis for the nanoSQUIDs used in this thesis. The following chapter is devoted to the fundamentals of superconductivity as needed to understand the experiments performed. Then an introduction into the Josephson effect is presented followed by an overview on SQUID technology and the working principles of these devices. If not stated otherwise, this chapter mostly follows [34, 94, 95].

4.2. Superconductivity

The most striking and probably most popular effect of superconductivity is that a sample undergoes a phase transition when cooled below a critical temperature T_c and its dc electrical resistivity drops to zero. This zero resistance can be demonstrated by inducing an electrical current in a superconducting solenoid, its decay rate is then probed, leading to extrapolated decay times in the range of 100 000 years [96]. The mechanism of superconductivity has theoretically been described by the BCS-Theory [97]. In simple words, this theory describes that in the superconducting ground state electrons couple in pairs (so called Cooper pairs) with opposite wavevector and spin and the coupling is mediated by phonons. Furthermore all n electrons in the material are described by one single wavefunction instead of n of them, just differing in phase for different locations in the material.

Superconductivity can be found in a wide range of materials. It is present in pure elements (e.g. Hg, Nb, Pb), in alloys (e.g. NbTi, NbN), ceramics (e.g. $\text{YBa}_2\text{Cu}_3\text{O}_7$, $\text{HgBa}_2\text{Ca}_2\text{Cu}_3\text{O}_8$) as well as in organic materials (e.g. Rb_3C_{60} , $\text{K}_{3.3}\text{Picene}$). All these materials have in common that they show zero electrical resistance below T_c , but they differ in magnitude of T_c and their response when an external magnetic field is applied. High temperature superconductors like the ceramic cuprates often have $T_c > 77$ K and thus can be cooled with liquid nitrogen. On the other hand, most superconductors show T_c well below 77 K. Room temperature superconductivity or something close to it has not yet been achieved.

When weak magnetic fields are applied to any superconducting material cooled below T_c then the field is completely expelled from its bulk. This shielding effect, equivalent to perfect diamagnetic behavior, is also known as the Meissner-Ochsenfeld effect [98]. This shielding, in the case of superconductors, can not exclusively be explained by the law of induction which requires a changing magnetic field. To clarify this, two descriptive examples are given, where the second is in contrast to ordinary diamagnets. When a superconducting material is cooled

below T_c and an external field is ramped up, eddy currents are induced to expel the field from inside the material. This example is in line with what is known about common diamagnets, the following case however is exclusive to superconductors. In case of a constant field applied to a superconductor above T_c the induced eddy currents soon decay and the material is penetrated by field lines. When cooled below T_c in constant field, surface currents spontaneously emerge and expel the magnetic field completely from the inside of the now superconducting material. Mathematically this can be derived from the London equation for exponentially decaying fields in a superconductor.

Applying stronger magnetic fields, the behaviour of different superconductors is not universal and in many cases not all of the field is expelled from the bulk. Depending on the response to increasing external fields, superconductors are divided in two classes (type I and II), which can be classified with the phenomenological Ginzburg-Landau theory [34] and London equation [99]. Essential parameters are the London penetration depth λ_L and the superconducting coherence length ξ . The London penetration depth is a decay constant classifying the distance to which a magnetic field can penetrate a superconductor until it falls off to $1/e$ the value at the superconductor's surface. λ_L can be derived, considering the London equation and Ampere's law for the case of a flat superconductor-free space interface and a constant magnetic field B_0 perpendicular to this interface. The field inside the superconductor is the given by

$$B(x) = B_0 e^{(-\frac{x}{\lambda_L})}. \quad (4.1)$$

The penetration depth is typically on the order of 10^{-8} m and given by the expression

$$\lambda_L = \sqrt{\frac{m}{\mu_0 n q^2}} \quad (4.2)$$

with the mass of the sample's charge carriers m , their number density n and charge q .

The other important parameter to characterize superconductors is the superconducting coherence length ξ which is proportional to the mean free path of conduction electrons in a metal and defines the scale at which superconducting electrons can recover their equilibrium after small perturbations. Within the Ginzburg-Landau theory this parameter can be derived to

$$\xi = \frac{\hbar v_F}{2E_g} \quad (4.3)$$

where \hbar is Planck's constant, v_F the Fermi velocity and E_g the superconductor's energy gap between superconducting and normal conducting state.

With the aid of the two material parameters just introduced, it is possible to define a criterion to distinguish the two types of superconductors.

Superconductors which have $0 < \lambda_L/\xi < 1/\sqrt{2}$ are type I and are also known as soft superconductors, because they can withstand less magnetic field before the superconducting phase breaks down. This type mostly consists of pure elements like e.g. Al, Pb, Hg. The behavior of a type I superconductor in an applied magnetic field is sketched in Fig. 4.1a). The figure shows a linear relation between applied field $\mu_0 H$ and internal magnetization $-\mu_0 M$ of the superconductor to expel the applied field. This relation holds until a critical field H_c is reached where the magnetization suddenly drops to zero which indicates the breakdown of the superconducting phase. The superconducting or Meissner phase depends on the sample's temperature and the applied field as shown in the phase diagram in Fig. 4.1b). This plot also describes the influence that temperature and magnetic field have on each other. The lower

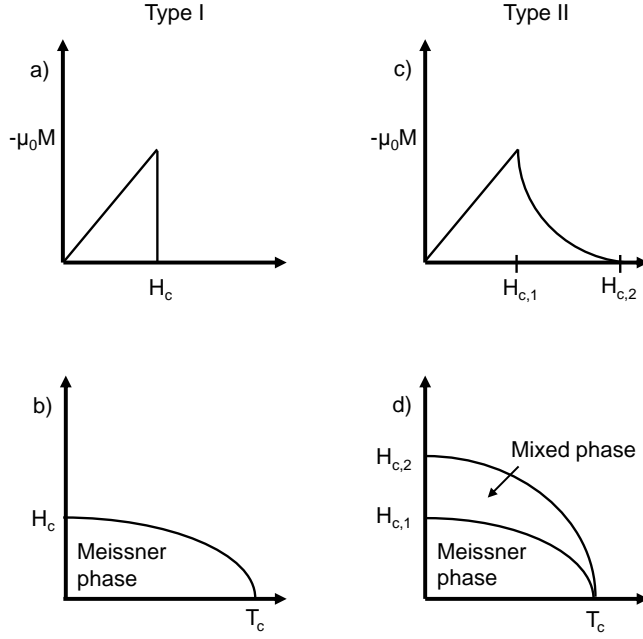


Figure 4.1. | a)/c) Magnetization of a type I/type II superconductor versus applied magnetic field. b)/d) H-T phase diagram of a type I/type II superconductor.

the temperature, the higher the fields a superconductor can withstand. Vice versa a strong applied field leads to a reduction of the effective critical temperature.

Superconductors of type II are those with $\lambda_L/\xi > 1/\sqrt{2}$ which do not show a sharp phase transition with applied magnetic field as depicted in Fig. 4.1c). The group of type II materials consists almost exclusively of alloys like the high T_c cuprates, or e.g. NbTi, but as an exemption also the pure element Nb. These superconductors are suitable for applications like e.g. in superconducting magnets since they withstand higher fields. These materials are characterized by two critical fields $H_{c,1}$ and $H_{c,2}$ corresponding to the boundaries of the superconducting phase and the mixed phase which is present before superconductivity breaks down. In the case of pure Nb at $T = 3.7$ K it is $H_{c,1} = 108$ mT and $H_{c,2} = 183$ mT [100]. Up to $H_{c,1}$ the type II superconductors behave exactly like the type I materials in the Meissner phase and build up magnetization to expel the applied field. Above $H_{c,1}$ there is no discontinuous transition to the normal state, instead until $H_{c,2}$ a mixed state exists where the field is not completely expelled and field lines can penetrate the material which partially becomes normal conducting. It is remarkable that the field lines do not penetrate the material homogeneously, but rather in spatially localized flux tubes as sketched in Fig. 4.2 [101]. Above $H_{c,1}$ it becomes energetically more favourable for the superconductor to not completely prevent the magnetic field from penetrating, but rather become partially normal conducting and let the field enter in these regions. These small normal conducting regions are shielded from the remaining superconductor by circular supercurrents and have a radius equal to the material's coherence length. The flux of the vortices is quantized in units of the fundamental flux quantum

$$\Phi_0 = \frac{h}{2e} \cong 2.00678 \times 10^{-15} \text{ Tm}^2 \quad (4.4)$$

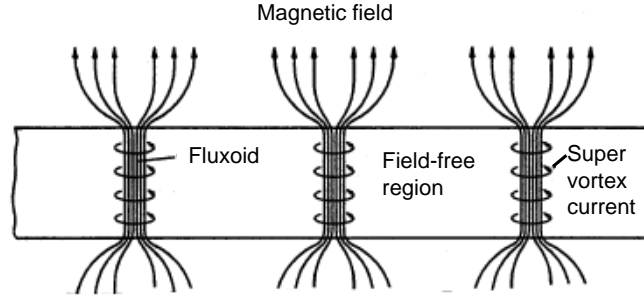


Figure 4.2. | Abrikosov vortices in a type II superconductor in the mixed phase above $H_{c,1}$. Figure adapted from [102].

and depends solely on Planck's constant h and elementary charge e [103]. Knowing the spatial dimensions and the flux quantization allows for an estimate of a material's lower critical field. The flux in a single vortex is $\pi\lambda_L^2 H_{c,1}$ which must be equal to Φ_0 , hence $H_{c,1} \simeq \Phi_0/\pi\lambda_L^2$. In case multiple vortices are present in a sample they repel each other and form regular lattices which have experimentally been observed and are known as Abrikosov vortex lattice [104, 105]. Vortices can travel inside the material, which increases the electrical resistance of the material. They can also be pinned to material defects naturally present or generated on purpose [105, 106].

In analogy to the critical field just discussed, the phase transition from superconducting to normal conducting state can also be induced by a current flowing in the superconductor (type I or II) and exceeding a critical magnitude I_c . H_c and I_c are directly connected because a current flowing induces a magnetic field which, if above H_c on the edges of the sample, induces the phase transition to normal conducting.

The concept of flux quantization, introduced with Abrikosov vortices, is of a more general nature in the physics of superconductors and not only limited to Abrikosov vortices. It is strongly connected with the single wavefunction and its phase describing the electrons in the superconducting groundstate and can be derived generally for a superconducting ring (for the full derivation see e.g. [34]). Note that this flux quantization holds for the sum of the flux generated by the ring current and the flux generated from an applied field. Together with the Josephson effect described in the next section these are the basics to understand the working principle of a SQUID.

4.3. Josephson effect

The Josephson effect describes tunneling phenomena where two superconductors are separated by a thin barrier [107]. The basic configuration of this device also known as Josephson junction (JJ) is sketched in Fig 4.3. The electrons in the left superconductor are described by wavefunction Ψ_L and phase φ_L , whereas the electrons on the right are described by Ψ_R and φ_R . The weak coupling of the two superconductors (S) can be achieved by either a thin insulating layer (SIS-junction) or a thin normal metal layer (SNS-junction). Also, point contact and constriction type JJs have been realized as well as junctions based on grain boundaries. In the

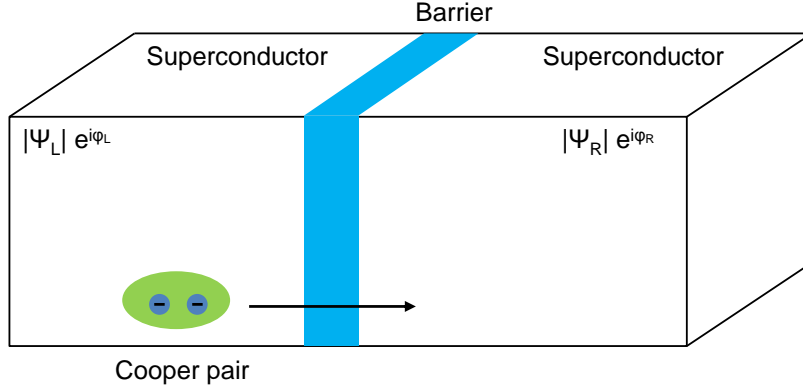


Figure 4.3. | Josephson junction consisting of two superconductors separated by a thin barrier that a Cooper pair can tunnel through.

original work, the mechanism was described for SIS junctions at $T = 0$ K. Resulting in the equation for the so called dc Josephson effect

$$I = I_0 \sin(\varphi_L - \varphi_R). \quad (4.5)$$

Here I is the supercurrent across the JJ and I_0 is the maximum supercurrent which is significantly lower than that of a bare superconductor. This equation means that in the static regime, in the absence of any external voltage applied to the junction, a dc current with values between $\pm I_0$ and depending on the phase difference between left and right superconductor is measurable [108].

If a (dc) bias current I_b is applied to the JJ, it is transported as a loss-free supercurrent across the device as long as $I_b < I_0$. This (dc) supercurrent is carried by Cooper-pairs tunneling through the barrier and is driven by the phase difference $\delta = \varphi_L - \varphi_R$. If the applied bias current exceeds the maximum supercurrent ($I_b \geq I_0$), the phase difference δ will evolve in time, leading to a voltage drop U across the JJ. This relation is known as the ac Josephson effect

$$\frac{d\delta}{dt} = 2\pi U \Phi_0. \quad (4.6)$$

Time integration of Eq. 4.6 and inserting it into Eq. 4.5 leads to

$$I = I_0 \sin\left(\frac{2\pi U}{\Phi_0} t + \delta_0\right). \quad (4.7)$$

This means that in the resistive state there will be an ac current oscillating across the JJ with a frequency $\omega_J = 2\pi U/\Phi_0$ due to the interference of the two wavefunctions of the superconductors. This effect can for example be exploited for voltage normals [109, 110].

Now a brief overview of non-idealized junctions is given where noise is considered and shunting of the JJ. The intention is to only highlight results and leave the details to [94, 95]. The first step in modeling a real junction is the so-called RCSJ model (resistively and capacitively shunted junction) where an ideal junction is connected in parallel to a capacity and a resistor. The resistivity introduces dissipation in the finite voltage regime without affecting the lossless

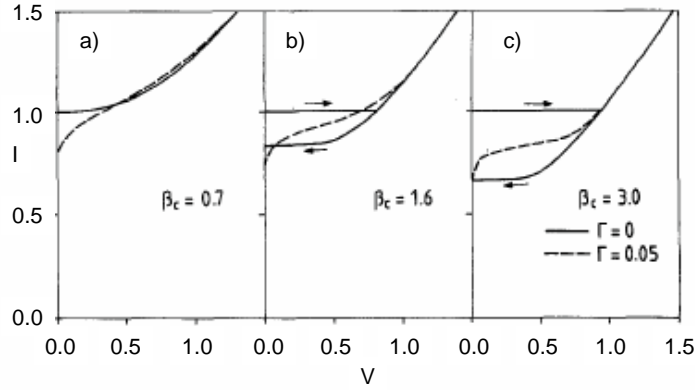


Figure 4.4. | Numerically calculated $I - V$ characteristic of a JJ with a) $\beta_c = 0.7$, b) $\beta_c = 1.6$, c) $\beta_c = 3.0$ at $T = 0$ K (solid lines) and at finite temperature (dashed line). Figure is adapted from [111].

dc regime of the JJ. The capacity can be viewed as geometric shunting capacitance between the two electrodes. Two regimes can be identified, the case of the over- and underdamped junction which are discriminated by the Stewart McCumber parameter $\beta_c = 2\pi I_0 R^2 C / \Phi_0$ [112, 113]. In the underdamped limit ($\beta_c > 1$) the junction shows a mostly ohmic response leading to a hysteretic current-voltage characteristic. In the overdamped limit ($\beta_c < 1$) the junction capacitance is negligible and the junction behaves non-hysteretic. For SQUIDS meant for practical applications, this regime is mostly preferred since it offers unambiguous response of the device to external signals. Both cases are shown in Fig. 4.4, the overdamped case is shown in a). In b) and c) the increase of the hysteretic behaviour with increasing β_c is demonstrated with the sweep direction marked by arrows. The hysteretic behaviour also leads to a temporal decrease of I_c . Apart from the hysteretic influence it has also been shown that I_c is temperature dependent and maximizes for low temperatures [108].

Apart from considering the RCSJ model, a further influence on the JJ's behavior is noise. Thermal noise leads to fluctuations of the current around its mean value which is visible in the I-V-curve for low voltages as "noise-rounding". This rounding effect is demonstrated in Fig. 4.4 with numerical calculations taken from [111]. The solid lines correspond to the case $T = 0$ K and the dashed lines correspond to finite temperature with normalized thermal energy $\Gamma = 2\pi k_B T / I_0 \Phi_0$.

The second relevant noise source is $1/f$ -noise which can dominate the sensitivity determining white noise of a JJ at low frequencies. This $1/f$ -noise can be caused by vortex motion or fluctuations in the JJ for example by trapping events in the junction during tunneling processes which lead to a variation of the critical current.

When a magnetic field is applied to a JJ it behaves in analogy to the optical double-slit experiment. The applied field leads to a modulation of I_0 which follows the Fraunhofer pattern [95]

$$I(\Phi) = I_0 \left| \frac{\sin(\pi\Phi/\Phi_0)}{\pi\Phi/\Phi_0} \right|. \quad (4.8)$$

4.4. The dc SQUID

A dc superconducting quantum interference device (dc SQUID) is formed by a superconducting ring which is intersected by two JJ, hence these JJ are connected in parallel. A schematic of

this basic principle is depicted in Fig. 4.5. A dc SQUID is a device to transform magnetic flux penetrating the loop into voltage (Fig. 4.5a)), currently being the most sensitive device to detect magnetic fields down to the range of 10^{-15} T [114] or respectively changes in magnetic flux on the order of $10^{-8}\Phi_0$.

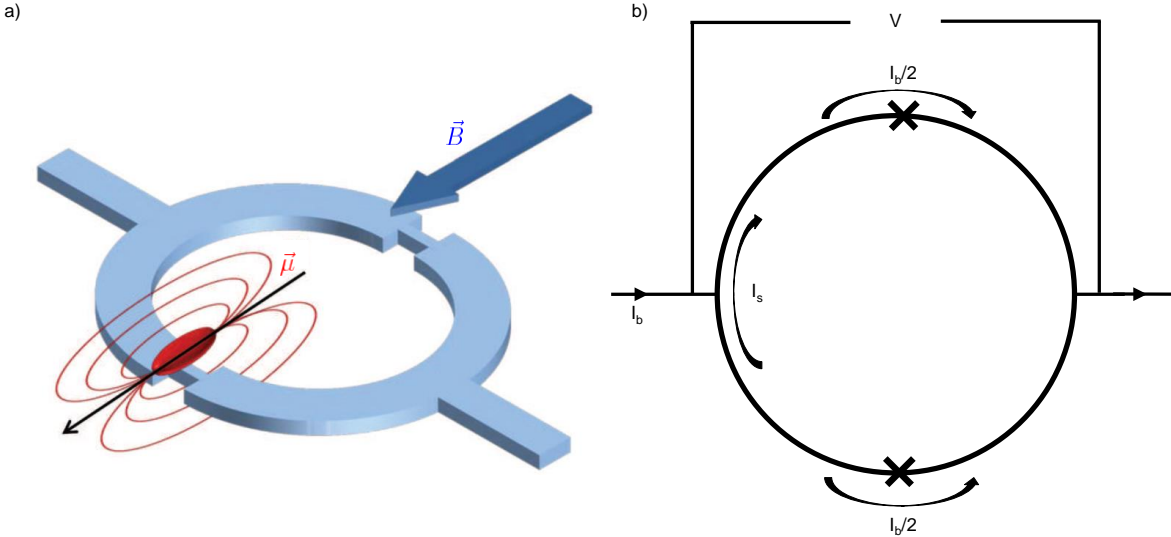


Figure 4.5. | a) Magnetic particle coupling flux in the SQUID loop. (Adapted from Ref. [115]) b) Schematic drawing of a dc SQUID consisting of two JJ connected in parallel via a superconducting ring. Introducing the bias current I_b , the voltage V and the screening current I_s .

For operation, the SQUID has to be biased, i.e. the working-point has to be set, with a constant current I_b slightly above the critical current I_c of the SQUID. For currents below I_c no voltage drop across the SQUID is measurable. Consequently, to determine the SQUID's I_c the bias current can be ramped up until a voltage appears. The $I-V$ characteristics of a SQUID look very similar to a single JJ, but $I_c = 2I_0$ is twice that of a single junction because the current splits equally on the two junctions. Knowing that, the following paragraph describes the mechanism how a SQUID detects magnetic flux from a user's point of view following [116] and omitting rigorous quantum mechanical treatment.

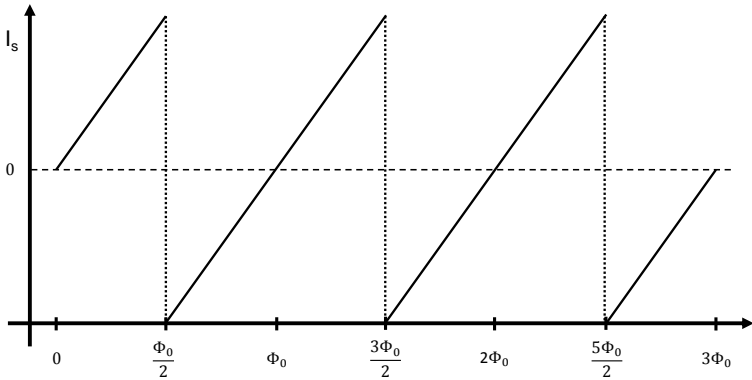


Figure 4.6. | Plot of the screening current I_s over magnetic flux Φ applied to the SQUID.

Coupling a very small amount of flux (much less than $\Phi_0/2$) into the SQUID loop by applying an external magnetic field, this will generate a screening current I_s opposing the applied field and effectively cancelling it out in the loop to fulfill flux quantization. This screening current, caused by the applied field, leads to a reduction of the SQUID's critical current. This is because I_s adds to the already applied I_b and with I_s present the amount of I_b that can flow before the junction becomes resistive is reduced. A sketch of the currents present is shown in Fig. 4.5b). With increasing applied magnetic flux the screening current will also increase as shown in Fig. 4.6 until $\Phi_0/2$ is present in the loop. When half a flux quantum is reached, the screening current will switch sign, now also producing $\Phi_0/2$ so that the flux in the loop is Φ_0 . This is the energetically most favourable solution to fulfill flux quantization in a superconducting loop since it is more favourable to enhance $< \Phi_0/2$ than shield $> \Phi_0/2$. Upon further increasing the applied flux, the screening current reverses direction to continue fulfilling flux quantization and so on with a periodicity of Φ_0 as the plot shows.

After understanding the screening/enhancement process this is now translated in the output voltage picture necessary to understand the read-out of the sensor (Fig. 4.7). On the left the $I - V$ characteristics of a SQUID are plotted for two cases. The right curve with maximum I_c corresponds to $\Phi = n\Phi_0$ and the curve left of it with reduced I_c is for $\Phi = (n + 1/2)\Phi_0$ with $n = 0, 1, 2, \dots$. The dotted line depicts the bias current which is slightly above I_c and stays fixed during the whole process. The crossing with the $I - V$ curve tells the output voltage of the SQUID which is plotted in the graph on the right. For increasing applied flux the $I - V$ -curve

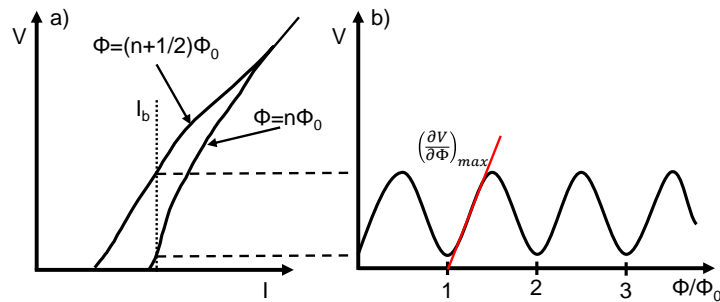


Figure 4.7. | a) SQUID's $I - V$ characteristics for different amounts of flux coupled in the loop. b) Sinusoidal modulation of the SQUID's output voltage over applied flux, induced by the flux dependence of the SQUID's critical current. Red line marks the ideal working point where transfer function is at a maximum.

oscillates between the two depicted extremal curves, leading to a Φ_0 -periodic voltage output of the SQUID.

The obtained sinusoidal $V - \Phi$ curve represents the measuring signal of the sensor, the drawback is its non-linearity in the so-called open loop mode. In the extremal points even a relatively large flux change leads to a vanishing voltage change. The maximum sensitivity is obtained in the reversal point of the curve where the slope, or transfer function $V_\Phi = \delta V / \delta \Phi$ is steepest, as marked in red. To profit from this, SQUIDS can be operated in the flux-locked-loop where a feedback flux is generated to maintain the SQUID's working point such that the transfer function is always at a maximum. This way, the sensor is most sensitive and also linear, thus allowing a direct translation of the measured output to flux. The spectral density of the SQUID's intrinsic white flux noise is given by $S_\Phi(f) = S_V(f) / V_\Phi^2$, where $S_V(f)$ is spectral density of the white voltage noise across the SQUID [95]. In the light of detecting small magnetic particles with a SQUID, a related important figure of merit is the spin sensitivity

$S_\mu^{1/2} = S_\Phi^{1/2}/\phi_\mu$ with coupling factor ϕ_μ [117]. This coupling factor ϕ_μ , depending on the SQUID's geometry and the magnetic particle's magnetization, quantifies the flux coupled into the SQUID loop by a magnetic particle with magnetic moment μ . To obtain a spin sensitivity of only a few Bohr magneton μ_B , it is essential to minimize S_Φ and maximize ϕ_μ .

SQUIDs suitable for application can be distinguished essentially in two categories. Nb SQUIDs with different kinds of junctions (e.g. microbridge [31, 32] or SNS [117]) which have proven their suitability for applications at low temperatures and intermediate fields (below 100 mT) and are prone to degradation. The high- T_c SQUIDs are made of cuprate superconductors (e.g. [118]) and work at higher temperatures and higher magnetic fields (in the Tesla-range) but suffer from degradation over time. Both device designs have proven their suitability for applications with high sensitivity to be able to measure also samples with low stray field.

Apart from the material choice, another important parameter for successful application is the size of the device. Miniaturization to the nanoscale is favourable because it allows operation at higher fields and is necessary to measure nanoscale samples because the loop size should be comparable to the sample for optimal detection. However it can not be shrunk to arbitrarily small dimensions, because that also leads to performance degradation and at some point is technologically not feasible anymore.

5. Experimental setup

5.1. Introduction

This chapter is devoted to cover some more technical details of sample preparation, realization and operation of the setup in the He³ cryostat and image acquisition of the cantilever in scanning probe mode in addition to chapters 6-9.

5.2. Ultrasoft Si cantilever

Key component of the hybrid magnetometer setup developed in the course of this thesis is the ultrasoft Si cantilever which is fabricated in a multi step lithography process [119]. Due to its very low spring constant, this kind of cantilever acts as a highly sensitive force transducer and it thus allows DCM of single nanoscale magnetic particles as well as scanning probe microscopy.

The cantilever (SEM image shown in Fig. 5.1) is beam shaped, clamped on the side of the chip and free at the other end. It is composed of a beam with width 4 μm and thickness 0.1

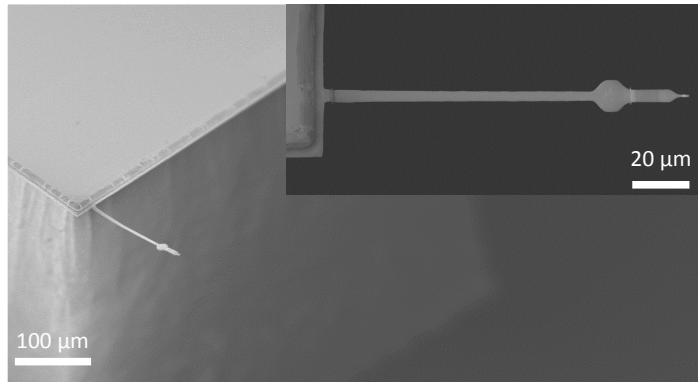


Figure 5.1. | SEM image of a cantilever as used in the course of this thesis. Figure adapted from [120]

μm . The length of this beam varies and for the cantilevers used in this thesis is 75 and 90 μm . Then a 12 μm wide and 12 μm long paddle with same thickness follows. The end of the cantilever is formed by a 1 μm thick, 4 μm wide and 18 μm long mass which suppresses higher order vibrational modes and is tapered towards its end to form a 1 μm wide tip.

These cantilevers show resonance frequencies from $f_0 = 3194 - 3980$ Hz, quality factors $Q_0 = (25 - 41) \cdot 10^3$ and very low spring constants $k_0 = 90 - 195$ $\mu\text{N/m}$. Another important parameter to describe such a cantilever as resonator, especially in the light of DCM, is its effective length l_e . The effective length is obtained by linear extrapolation of the cantilever's tip when oscillating in the fundamental mode and extending it to the base line as shown in Fig. 5.2. The obtained effective length with $l_e \leq l$ can be viewed as compensation to the cantilever's non-linear mode shape. The mode shape can either be determined by finite element

calculations [121] or in a more simplistic way by applying the Euler-Bernoulli theory of beams [122]. For a cantilever with a $75 \mu\text{m}$ long shaft $l_e = 76 \mu\text{m}$ and in the case of a $90 \mu\text{m}$ shaft

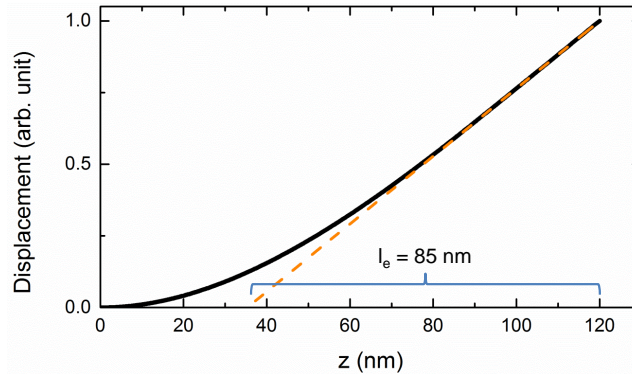


Figure 5.2. | Fundamental mode of a cantilever with $90 \mu\text{m}$ long shaft (black line) as determined by finite element calculations. The orange dashed line is the tangent to the cantilevers tip whose crossing with the base line determines $l_e = 85 \mu\text{m}$.

$l_e = 85 \mu\text{m}$.

To account for the interferometric read-out being at the position of the paddle and not the tip, a correction factor (c-factor) is introduced. Basing on the mode shape plot shown in Fig. 5.2, the displacement at the position of the paddle d_{paddle} and the tip d_{tip} is related $c = d_{tip}/d_{paddle}$. For the two different cantilever lengths used we obtain $c_{75} = 1.47$ and $c_{90} = 1.39$.

The interferometric read-out of the cantilever is described in some detail in chapter 7, a more detailed analysis of the interferometer and description of laser and displacement control can be found in [123].

5.3. Ni, CoFeB and permalloy nanotubes

In this section a brief summary of the sample fabrication methods for the magnetic Ni, CoFeB and permalloy ($\text{Ni}_{80}\text{Fe}_{20}$) NT samples is given. More extensive information can be found in [124] and references therein.

The general structure of all NT samples investigated throughout this thesis is the same (Fig. 5.3a)). They all consist of a GaAs core which is grown by molecular beam epitaxy (MBE) in vapor liquid solid (VLS) growth and is then coated with a magnetic shell.

These GaAs nanowires are grown at the EPFL Lausanne in the group of Prof. Anna Fontcuberta i Moral. For growth Si(111) wafers are used as substrates. The nanowires are growing mainly perpendicular to the substrate. The resulting GaAs nanowires have a hexagonal cross section and at a nanowire's end, a Ga droplet is present which serves as catalyst during growth. These nanowires are then used as a template to mechanically support the magnetic film which is applied in a second fabrication step now being described for the various samples used in this thesis. All processes involving coating the GaAs templates with magnetic thin films are conducted in Prof. Dirk Grundler's group at the TU München.

In chapters 6 and 7 Ni NTs are studied. Bulk Ni has a saturation magnetization $\mu_0 M_s = 0.64$ T at $T = 0$ K and its Curie temperature is $T_C = 627$ K [34]. The Ni NTs used in our studies were fabricated by PhD students Rupert Huber and Thomas Schwarze. The 30 nm thick Ni shell is grown by atomic layer deposition (ALD) which, due to its growth mechanism, avoids

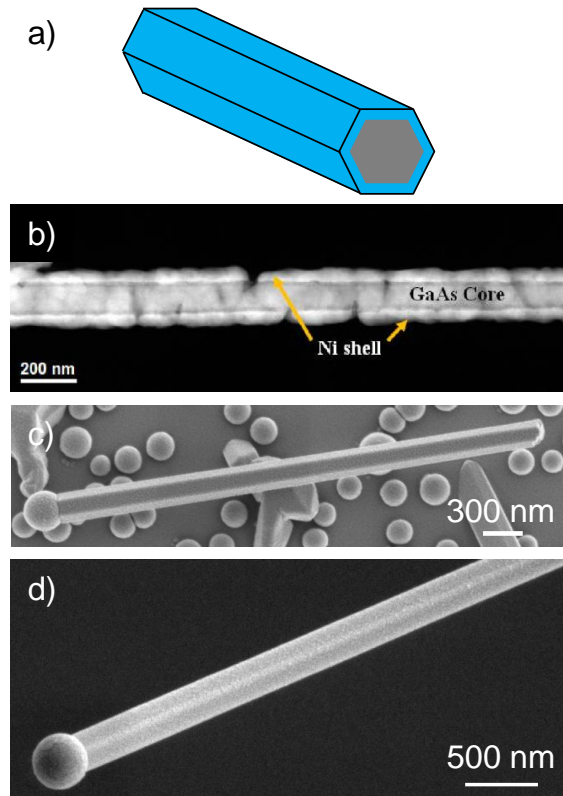


Figure 5.3. | a) Image of the general structure of a NT investigated consisting of a GaAs core (gray) and a FM shell (blue) b) SEM image of a Ni NT from the same batch used in this thesis. c) SEM image of a CoFeB NT from the same batch used in this thesis. d) SEM image of a Py NT from the same batch used in this thesis.

shadowing effects. Fig. 5.3b) shows a high resolution image of such a NT used in this thesis. From the image we can conclude that the surface of the NTs shows considerable roughness of up to 30 nm leading to occasional discontinuities of the Ni film.

For the experiments presented in chapter 8, NTs with a nominally 30 nm thick $\text{Co}_{20}\text{Fe}_{60}\text{B}_{20}$ shell are investigated. CoFeB shows no crystalline anisotropy [125] and has in bulk a saturation magnetization of $\mu_0 M_s = 1.8 \text{ T}$ [126] and Curie temperature $T_C > 1300 \text{ K}$ [127]. The samples, shown in Fig. 5.3c), were fabricated by PhD student Florian Heimbach. The same GaAs nanowires that are used as templates for the Ni NTs are again used. The CoFeB shell is applied in a magnetron sputtering process in Xe atmosphere with a $\text{Co}_{20}\text{Fe}_{60}\text{B}_{20}$ target. To obtain a homogeneous thickness and avoid shadowing, the wafer containing the as-grown GaAs NTs is mounted under 35° angle relative to the incoming CoFeB flux and is rotated constantly during the process.

In chapter 9 experiments on NTs formed by a 30 nm thick film of the $\text{Ni}_{80}\text{Fe}_{20}$ alloy known as permalloy are presented. Permalloy also shows no magnetocrystalline anisotropy [128] and has a saturation magnetization $\mu_0 M_s = 1.0 \text{ T}$ [129] and Curie temperature $T_C = 853 \text{ K}$ [130] in bulk. Coating of the GaAs nanowires is realized by a thermal evaporation process performed by PhD student Florian Heimbach. Same as for CoFeB, the sample is mounted with a 35° tilt and constantly rotated during evaporation to achieve conformal coating. An image of such NT is shown in Fig. 5.3d).

5.4. Sample to cantilever attachment

Attachment of the magnetic NTs to the cantilever tip follows a standard procedure routinely used in the Poggio Lab also for non-magnetic samples with different aspect ratios than the elongated NTs investigated in this thesis. A more detailed and excellently illustrated description can be found in [37].

The main tool is an optical microscope (Nikon Eclipse FN1) equipped with hydraulic micro-manipulators (Narishige MMO-202ND) sitting on an optical table to reduce vibrations during the delicate sample fabrication process. The microscope offers high magnification (eyepiece: $20\times$, objectives: $5\times$ and $50\times$) and most importantly a working distance in the range of 10 – 30 mm for convenient accessibility of the sample under investigation. The glass needles used to

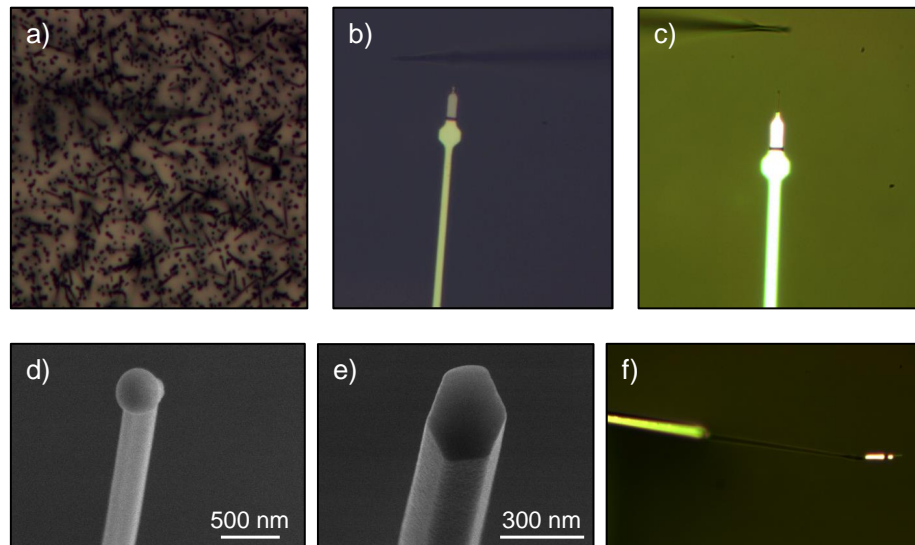


Figure 5.4. | Optical microscope images of a) Wafer of as-grown NTs. b) A droplet of glue transferred to the cantilever's tip. c) NT placed in the desired orientation to the cantilever. d) SEM image of the catalyst at the tip of a NT. e) The same NT with its catalyst cut off in a FIB process. f) Side view of a cantilever whose shaft accidentally was exposed to FIB irradiation.

directly handle individual specimen are pulled from solid glass rods and are renewed for each new process to avoid contamination of the sample. The glass needles are fabricated in a two-step pulling process with a commercial puller (Narishige PC-10). Different tip shapes and radii ($< 1 - 100 \mu\text{m}$) are available by choosing appropriate parameters of the resistive heating coil and the attached pulling weights [131, 132]. To avoid electrostatic charging, needles, sample, epoxy, and cantilever each are exposed to a radioactive α -source for about one minute.

For the actual attachment process, first a wafer piece with as-grown NTs is placed under the microscope Fig. 5.4a). Using one glass needle, an individual NT is picked up from the wafer. This process can be thought of as chopping down a tree. The needle with the NT sticking to its end can then be parked temporarily aside from the working area.

In the next step the two component epoxy (Gatan G1), mixed on a glass slide is placed under the microscope. With a fresh glass needle, a droplet is picked up and transferred to the tip of the cantilever where it is wiped to leave a small droplet ($\leq 100 \text{ fl}$) on the cantilever Fig. 5.4b).

The already picked up NT is now transferred with one of its ends to this drop of epoxy and its long axis roughly parallel to the cantilever. After this coarse alignment during the transfer process a final alignment is performed with the tip of the glass needle pushing the NT in position (Fig. 5.4c). The aligned NT on cantilever now needs to cure over night before further processing.

For the study of NTs it is desirable to have samples deviating little as possible from an ideal tubular structure. Due to their growth, the NTs investigated in this thesis have a ball shaped catalyst on one end (Fig. 5.4d)), which is not favorable for the experiments performed. To remove the catalyst at the NT's end, the cantilever is brought to a focussed ion beam microscope (FIB) to cut off the interfering catalyst ball (Fig. 5.4e)).

To minimize damage to the magnetic material, low acceleration voltages and ion currents are chosen for the cutting process. Generally the process has to be conducted with great care, because excessive exposure of magnetic material to Ga ion bombardment changes the magnetic properties [133]. Additionally, the cantilever is strongly affected by any exposure of its shaft to Ga ions. In the example depicted in Fig. 5.4f) the cantilever is bent at the paddle with possible degradation of mechanical properties and can not be used for experiments any more.

5.5. He³ cryostat

A crucial element to operate this, not only electrically sensitive, but also mechanically, sensitive setup is isolation from external vibrations. Therefore the cryostat is mounted to an optical table with its platform mounted on legs with pressurized air bearings (Fig. 5.5a)).

The microscope head itself is hanging from springs, for further isolation of the sensitive cantilever from outside vibrations, in the UHV sample chamber (Fig. 5.5c)). In order to make the experiment's operation possible in a wide temperature range and not be restricted to the temperature of the liquid He⁴ bath a further chamber, the inner vacuum chamber (IVC), is used. To achieve thermal isolation from the He⁴-bath, the UHV sample chamber is placed inside the IVC, which in turn is directly placed in the He-bath.

The cryostat is equipped with a He³ circulation which includes a He⁴ reservoir, which is pumped on, and reaches 1 K (1K-pot) to pre-cool the He³. Due to this He³ circulation, temperatures down to 300 mK can be reached. The additional use of resistive heaters among other places at the sample chamber and the 1K-pot enable to reach temperatures up to 120 K. Due to thermal decoupling of the sample chamber from the He-bath, stable operation at elevated temperatures is possible with reasonable He consumption. Temperature control is realized via a PID-loop that controls the built-in heaters. Under stable conditions and with careful operation, stability in the range of ± 0.3 mK over several hours is possible.

Magnetic fields up to ± 6 T can be applied with a superconducting magnet (Cryomagnetics) enclosing the IVC. To enclose the IVC, the magnet's bore is 15 cm. This and the number of windings necessary to achieve such high fields leads to an inductance of 27.7 H. Due to this inductance the magnet shows considerable lag when sweeping small fields. To account for this lag, the nanoSQUID is used as a field sensor to determine a reference which is proportional to the actual applied field. More details of this method are described in chapter 7.

Apart from these already available elements, additional wiring is necessary to operate the serial SQUID array (SSA), serving as an amplifier, and the nanoSQUID. A scheme of the wiring including basic components of the cryostat is shown in Fig. 5.5b). Additional to electrical connection, the wiring has to accomplish three requirements.

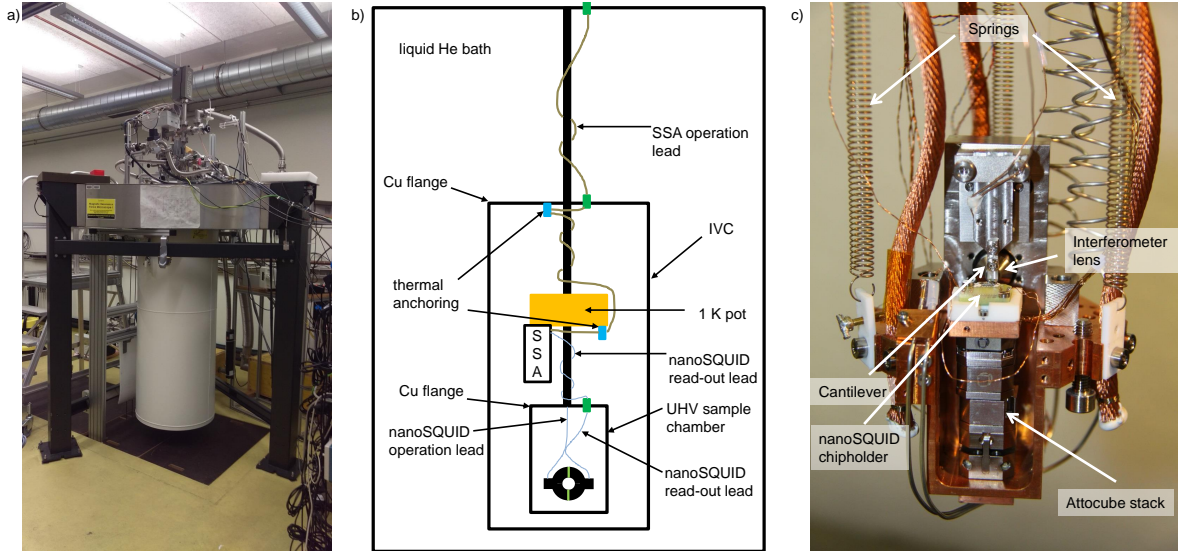


Figure 5.5. | a) Picture of the cryostat mounted to the optical table. b) Scheme of He^3 cryostat used for the experiments including all necessary components added for nanoSQUID and SSA operation. c) Picture of the microscope head hanging from springs.

The wires have to be of low resistance to ensure proper operation of the SQUID devices, therefore we use plain Cu wires. Because SQUIDs are electrically very sensitive, proper shielding of the devices is necessary, consequently in a first step the Cu wires are prepared in twisted-pair configuration. For shielding of the Cu twisted-pairs, a tubular braid made of tinned copper (AlphaWire 2162) serves as conductive jacket to the twisted-pairs. Electrical connection of the different segments via feedthroughs (realized with crimp contacts) between vacuum chambers is ensured. The whole shielding braid is connected to one common ground, which is the cryostat's mass.

To operate the SSA and nanoSQUID at low and stable temperatures, proper thermal anchoring is necessary. This is achieved by winding the Cu wires a few turns around brass bobbins and fixing them with the thermally conducting epoxy Stycast[®]. These bobbins (marked in blue in Fig. 5.5b)) are then firmly screwed onto thermalization stages in the cryostat. As first anchor to 4 K the flange of the IVC is chosen, a further anchor below 1 K is the cryostat's 1K-pot.

To ensure reliable operation of the SSA, additional to wiring and thermal anchoring, effective shielding of electromagnetic radiation is inevitable. Serving as an amplifier for the nanoSQUID's output voltage, any spurious signals coupling into this highly sensitive device have to be avoided. The chip is placed inside a screwed capsule, made of Nb, featuring only two small holes to feed the wire connections. This capsule is then wrapped with a sandwich of Mu-metal (a Ni-Fe soft magnetic alloy) foil and again Nb foil. The Mu-metal's purpose is to protect the Nb capsule from any spurious magnetic fields (e.g. earth's magnetic field, rest magnetization in cryostat parts) during the cool-down. This is necessary because, although a perfect diamagnet, superconductors can easily trap vortices when undergoing the phase transition from normal conducting to the superconducting state. The outer most Nb layer in turn protects the Mu-metal from getting magnetized when high fields are applied during the experiments. Inside the capsule, the SSA is fixed with a Ti screw to a oxygen-free high thermal conductivity (OFHC) Cu finger which is anchored to the 1K-pot for optimal thermalization

of the device. The use of OFHC Cu has proven to be mandatory. In a first attempt Nb was used instead, but did not allow stable SSA operation. Low thermal conductivity in the superconducting state does not provide enough cooling power, hence thermal instabilities caused by resistive heating due to the device's operation occur.

5.6. Nb nanoSQUID and its operation

In general, the design of dc SQUIDs follows always the same principle as depicted in Fig. 4.5 in the previous chapter. A dc SQUID consists of a superconducting ring intersected by two JJs. The nanoSQUIDs used in the course of this thesis also follow this design principle, but are optimized towards the challenges of these experiments. Their geometry, as well as the read-out scheme used, shall be introduced in more detail in this section.

The nanoSQUID's loop is not in the plane of the substrate, but perpendicular (in the $\hat{x} - \hat{z}$ plane) to it in a sandwich structure (Fig. 5.6a,b)). The external magnetic field is applied along \hat{z} that it produces minimum magnetic flux in the SQUID loop and the JJs. In this way the detected signals from the sample under investigation are much greater, as compared to the signals arising from the applied magnetic field.

The superconducting ring consists of Nb and the $(200 \times 200 \times 24 \text{ nm}^3)$ barriers are formed by normal conducting $\text{Hf}_{50}\text{Ti}_{50}$. HfTi is chosen because it does not become superconducting at 4.2 K, it supports high critical current densities $200 - 300 \text{ kA cm}^2$ and it serves as an intrinsic shunt leading to non-hysteretic $I - V$ characteristics. The loop dimensions are given by the spatial separation of the JJs ($1.6 \mu\text{m}$) and the distance between top and bottom electrode (224 nm). The devices are fabricated by the Physikalisch-Technische Bundesanstalt (PTB) in Braunschweig. The fabrication process of this tri-layer structure includes electron-beam lithography, chemical-mechanical polishing and sputtering. The details of the process are described in [134].

The nanoSQUID used is extremely compact, because it does not need a pickup loop, an external shunt resistor or a modulation coil for feedbacking; all of this is directly integrated into the device as described and sketched in Fig. 5.6a,b).

The fabrication process is wafer based, consequently there are multiple nanoSQUIDs located on one wafer. In the experiments, only a single device, which has to be cut out of the wafer, can be mounted. The cutting is done with a diamond wafer saw to minimize dust, obtain clean edges and avoid mechanical stress that might damage the nanoSQUIDs. This step is of great importance, because the nanoSQUID has to be located closer than $200 \mu\text{m}$ to the edge facing the interferometer lens (Fig. 5.6c)). For devices further inside the chip, a simultaneous operation with the cantilever close by is not possible due to shadowing of the cantilever's paddle from the laser light necessary for read-out.

After cutting out a single nanoSQUID, the wafer piece has to be further prepared for operation. The chip (dimensions below $(1 \times 0.5) \text{ cm}^2$) is glued with TorrSeal[®] onto a chip holder compatible with our microscope. Great care has to be taken to place the chip as horizontal as possible to minimize misalignment, i.e. the influence of the applied magnetic field on the nanoSQUID's performance (Fig. 5.6d)).

After gluing the chip onto the holder and an overnight cure of the TorrSeal[®], Al bonding between the Nb bondpads on the chip and the contacts of the chipholder is done. Cu twisted pair cables, soldered to the chipholder, are now employed to connect the I_{mod} to coaxial lines,

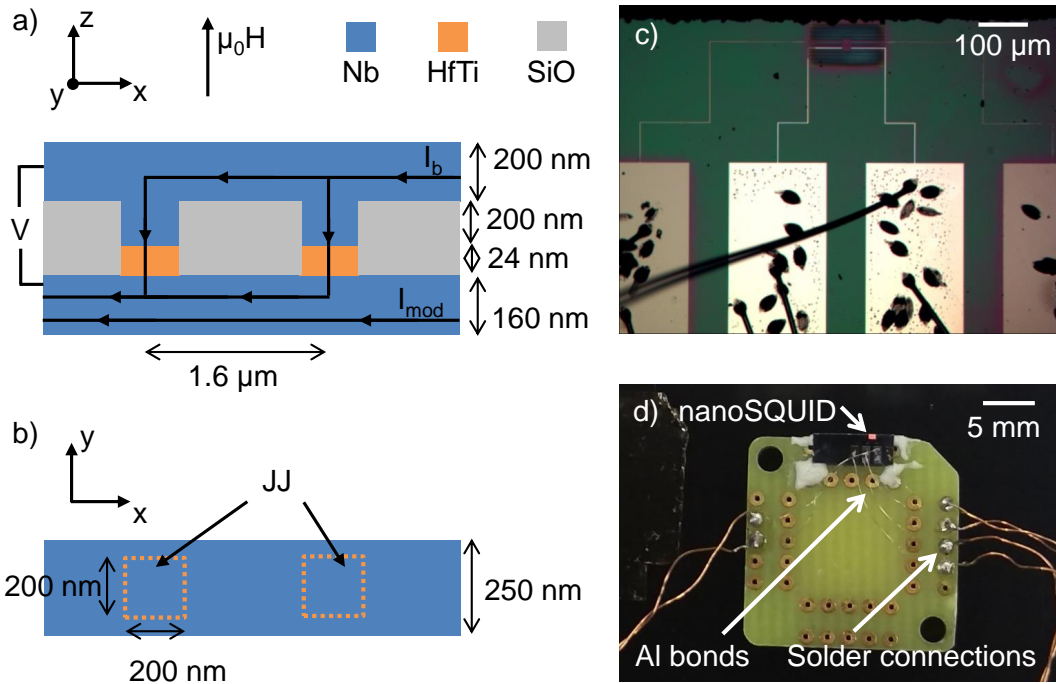


Figure 5.6. | Sketch (not to scale) of the nanoSQUID's dimensions in a) side view with direction of applied currents and voltage read-out and b) top view. c) Microscope image of the nanoSQUID chip showing the cut edge at the top of the image. The nanoSQUID is located in the middle of rectangular field of Nb stripes needed for the fabrication. On the bottom, four Nb bond pads are visible with bonds coming out. d) Picture of the nanoSQUID chip glued with TorrSeal[®] (white spots) to the chip holder. The Al bonds go from the chip to the inner row of connectors on the chip. Soldered to the outer row are the Cu twisted-pairs.

I_b to Cu lines and V to the SSA input. The use of low resistance wires is absolutely essential to avoid heating of the nanoSQUID due to the currents applied.

I_b and I_{mod} are delivered by a set of custom electronics which are battery driven to reduce 50 Hz noise. The nanoSQUID's output voltage is sent to the SSA, where it is amplified and then read out. Read out and operation of the SSA is achieved with Magnicon XXF-1 electronics, placed outside the cryostat, which is computer controlled by the commercial software "SQUIDViewer".

The nanoSQUID's FLL operation is realized by a home-made software feedback in LabView. The nanoSQUID's working point is set to the steepest point of its $V(\Phi)$ (compare Fig.4.7) curve by applying the necessary I_b and I_{mod} which remain fixed during an experiment. The flux generated by the external field and the magnetic NT, causing a voltage offset, is compensated by applying matching I_{mod} via the FLL software. This way a direct measure of the amount of flux generated by the investigated NT is available.

5.7. Scanning probe microscopy

The cantilever fulfills multiple purposes in the experiments described in this thesis. Apart from its use as a stand-alone sensor in the DCM (described in chapter 3) it is used to position the magnetic NTs relative to the nanoSQUID in optimal coupling position. Additional to this, the

cantilever serves as a scanning-probe to navigate on the nanoSQUID chip and, equipped with a NT as magnetic tip, it senses magnetic field gradients that allows us to detect e.g. Abrikosov vortices in the superconducting structure (compare Chapter 6). A general description of the frequency shifts induced in the cantilever will be given in the following.

The cantilever is mounted in pendulum-geometry, is singly clamped, beam-shaped and due to its geometry can only oscillate along one direction we define along \hat{x} . The derivation of the frequency shift is first generally derived and then the special case of a magnetic dipole is treated. The cantilever can be approximated as simple harmonic oscillator

$$m\ddot{x} + \Gamma\dot{x} + k_0x = \mathbf{F}\hat{x} \quad (5.1)$$

with mass m , damping Γ , spring constant k_0 and external force \mathbf{F} . The cantilever is only sensitive to components of \mathbf{F} along \hat{x} . Distinguishing between constant and spatially varying components is necessary, because constant force components simply result in constant deflection of the cantilever which is not what we detect. In the microscope used, changes in the cantilever's resonance frequency, which are due to changes in the effective cantilever's spring constant are measured. The small deflections x allow to expand $\mathbf{F}\hat{x}$ to first order in x around $x = 0$

$$m\ddot{x} + \Gamma\dot{x} + k_0x = F_{x,0} + \left. \frac{\partial F}{\partial x} \right|_{x=0} x. \quad (5.2)$$

This can be rewritten to clarify the force's influence on the spring constant

$$m\ddot{x} + \Gamma\dot{x} + \left(k_0 - \left. \frac{\partial F}{\partial x} \right|_{x=0} \right) x = F_{x,0}. \quad (5.3)$$

Assuming small dissipation ($\Gamma \approx 0$) and neglecting the constant force term, solving the differential equation leads to

$$\omega = \omega_0 \sqrt{1 - \frac{1}{k_0} \left. \frac{\partial F}{\partial x} \right|_{x=0}}. \quad (5.4)$$

Using $\Delta\omega = \omega - \omega_0$, $\omega = 2\pi f$ and $\sqrt{1-x} \approx 1 - x/2$ for $x \ll 1$ we obtain for the measured frequency shifts

$$\Delta f = \frac{-\omega_0}{4\pi k_0} \left(\left. \frac{\partial F}{\partial x} \right|_{x=0} \right) \quad (5.5)$$

This result is generally valid, for the case of a scanning probe experiment in the described geometry. To e.g. model vortices detected with a magnetic particle at the cantilever tip, we have to consider the actual forces and fields present.

The force acting on the cantilever and causing the frequency shift is determined by the interaction between the magnetic particle (in our case a NT), which we assume to be magnetized perfectly along $\pm\hat{z}$, and the Abrikosov vortex trapped in the superconductor. The energy of the NT in a magnetic field is given by the term

$$U = -\boldsymbol{\mu}\mathbf{B}. \quad (5.6)$$

Because the cantilever is assumed to oscillate along \hat{x} , we only consider force components along that direction

$$F_x = \frac{\partial}{\partial x}(\boldsymbol{\mu} \cdot \mathbf{B}) = \pm\mu \frac{\partial B_z}{\partial x}. \quad (5.7)$$

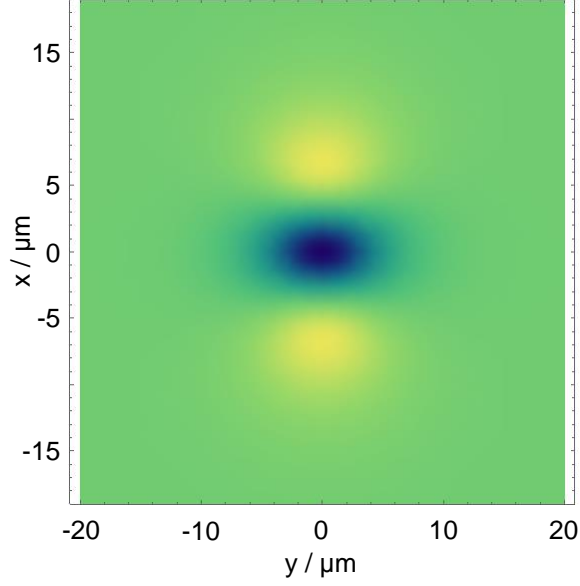


Figure 5.7. | Modelling of the expected scanning probe microscopy signal an ideal magnetic dipole causes.

Inserting the just obtained result in the general Eq. 5.5 leads to

$$\Delta f = \pm \mu \frac{\omega_0}{4\pi k_0} \left(\frac{\partial^2 B_z}{\partial x^2} \Big|_{x=0} \right). \quad (5.8)$$

This equation determines the frequency shift detected by a cantilever in the given geometry with a magnetic NT, having a magnetic moment μ , at its tip and an Abrikosov vortex generating a magnetic field with a component B_z along \hat{z} . The expected spatial map of the frequency shift at a fixed scanning height z can be simulated. Assuming a perfect magnetic dipole given by

$$\mathbf{H}(\mathbf{r}) = \frac{1}{4\pi} \left(\frac{3\mathbf{r}(\boldsymbol{\mu} \cdot \mathbf{r})}{r^5} - \frac{\boldsymbol{\mu}}{r^3} \right), \quad (5.9)$$

a magnetic field along \hat{z} and evaluating the expression around the cantilever's equilibrium position 0 leads to the results plotted in Fig. 5.7.

6. Nanoscale multifunctional sensor formed by a Ni nanotube and a scanning Nb nanoSQUID

Adapted from:

J. Nagel, [A. Buchter](#), D. Ruffer, F. Xue, D. P. Weber, O. F. Kieler, T. Weimann, J. Kohlmann, A. B. Zorin, E. Russo-Averchi, R. Huber, P. Berberich, A. Fontcuberta i Morral, M. Kemmler, R. Kleiner, D. Koelle, D. Grundler, and M. Poggio,

”Nanoscale multifunctional sensor formed by a Ni nanotube and a scanning Nb nanoSQUID”,

Phys. Rev. B **88**, 064425 (2013)

Nanoscale magnets might form the building blocks of next generation memories. To explore their functionality, magnetic sensing at the nanoscale is key. We present a multifunctional combination of a nanometer-sized superconducting quantum interference device (nanoSQUID) and a Ni NT attached to an ultrasoft cantilever as a magnetic tip. By scanning the Nb nanoSQUID with respect to the Ni tube, we map out and analyze their magnetic coupling, demonstrate the imaging of an Abrikosov vortex trapped in the SQUID structure — which is important in ruling out spurious magnetic signals — and reveal the high potential of the nanoSQUID as an ultrasensitive displacement detector. Our results open a new avenue for fundamental studies of nanoscale magnetism and superconductivity.

6.1. Introduction

There is growing interest in the investigation of small spin systems, such as molecular magnets [135–137], single chainmagnets [138], single electrons [139], or cold atom clouds [140]. Various detection schemes, e.g., magneto-optical spin detection [141, 142], magnetic resonance force microscopy [143], or scanning-tunneling-microscopy assisted electron spin resonance [144, 145], have been developed to detect such systems. Unlike these techniques, superconducting quantum interference devices (SQUIDs) directly measure the stray magnetic flux produced by a small magnetic particle (SMP) with a large bandwidth [146, 147]. This capability is especially interesting for the study of SMPs that support magnetic states not normally allowed in macroscopic magnets [148–151].

A direct current (dc) SQUID is a superconducting loop, intersected by two Josephson junctions, and works as a flux-to-voltage transducer, i.e., the magnetic flux Φ threading the loop modulates the voltage V across the junctions, with a period of the magnetic flux quantum $\Phi_0 = h/2e$ (see, e.g., Ref. [152]). Since the magnetic field distribution of a SMP is very close to that of a magnetic dipole, the figure of merit for SQUIDs is the spin sensitivity $S_\mu^{1/2} = S_\Phi^{1/2}/\phi_\mu$. Here, S_Φ is the spectral density of flux noise power and $\phi_\mu \equiv \Phi/\mu$ is the coupling factor, i.e., the flux coupled to the SQUID per magnetic moment $\mu \equiv |\boldsymbol{\mu}|$ of the SMP. Both S_Φ and ϕ_μ can be optimized by scaling the SQUID down to nanometer dimensions [153–156]. Various fabrication techniques, e.g., electron-beam lithography [117, 157], focused ion beam milling [156, 158, 159], atomic force microscopy anodization [160, 161], self-aligned shadow evaporation [87], or a combination of electronbeam lithography with the use of carbon nanotube junctions [162], have been used to realize nanoSQUIDs.

The experimental determination of S_Φ poses no basic difficulties, in some cases yielding very low $S_\Phi^{1/2} \approx 0.2\text{--}0.3 \mu\Phi_0/\sqrt{Hz}$ (Refs. [117, 157, 159], and [163]). In contrast, the determination of ϕ_μ is not straightforward, as it depends on the position \mathbf{r}_p and orientation $\hat{\epsilon}_\mu$ of $\boldsymbol{\mu}$ relative to the SQUID loop and on the SQUID geometry. Up to now, ϕ_μ has been estimated by numerical or analytical calculations, which often rely on strongly simplifying assumptions [154, 155, 164]. Also, a more advanced routine for calculating $\phi_\mu(\hat{\epsilon}_\mu, \mathbf{r}_p)$, which takes explicitly into account the SQUID geometry [117, 156], has not yet been validated experimentally.

Here, we present a multifunctional sensor system, which combines a low-temperature magnetic force microscope (LTMFM) using a Ni NT as a ferromagnetic tip and a Nb nanoSQUID, optimized for SMP detection. This system allows for magnetization measurements of nanoscaled magnetic samples using very different measuring principles. In the case of LTMFM, forces acting on the magnetic tip are detected, e.g., allowing for the imaging of Abrikosov vortices in superconductors [165, 166]. For the nanoSQUID, signals caused by the entrance of such vortices are indistinguishable from signals produced by a SMP. Therefore the *in situ* imaging of Abrikosov vortices is an important prerequisite for reliable nanoSQUID magnetometry. In the first part of the article, we identify the position of trapped flux in the superconducting lead of the nanoSQUID operated in high magnetic fields. In contrast to the LTMFM, the nanoSQUID directly measures the stray flux from the magnetic tip coupled to the SQUID loop. Therefore, in the second part, we present measurements of $\Phi(\mathbf{r})$ for the half space above the nanoSQUID by scanning a cantilever with a nanoscale ferromagnet at position \mathbf{r} as a magnetic tip. These findings are not exclusive to the use of a Ni NT, but should be valid for a wide range of SMPs. Furthermore, we show that the nanoSQUID can be used as a highly sensitive detector of displacement of the Ni NT.

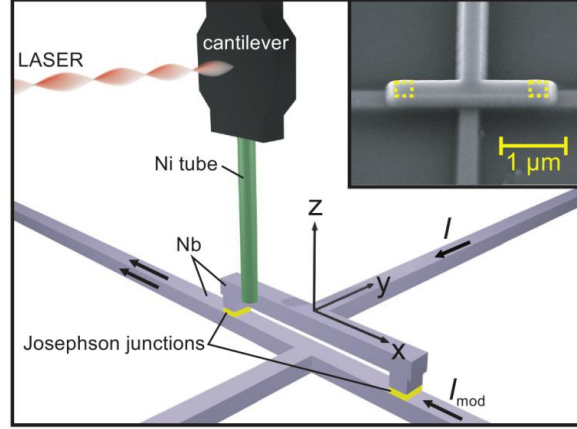


Figure 6.1. | Schematic view (not to scale) of the nanoSQUID and Ni NT geometry, indicating x, y, z directions as used below, with origin centered on the surface of the upper Nb layer. Thick arrows indicate flow of applied bias current I and modulation current I_{mod} . Inset shows scanning electron microscopy (SEM) image of the Nb nanoSQUID; dotted lines indicate the two JJs.

6.2. SQUID layout, properties and readout

For the experiments presented here, we use a dc SQUID which has a sandwich-like geometry (see Fig. 6.1), i.e., the two arms of the SQUID loop lie directly on top of each other, and are connected via two $200 \times 200 \text{ nm}^2$ planar Nb/HfTi/Nb Josephson junctions [134, 167]. The electric transport and noise properties of Nb nanoSQUIDs with this layout are described in Ref. [163]. For this geometry, the size of the SQUID loop (in the $x - z$ plane) is given by the gap ($\approx 225 \text{ nm}$) between the top and bottom Nb layers and the lateral distance ($\approx 1.8 \mu\text{m}$) between the two junctions. Using such a geometry, a very small loop size, and hence a small loop inductance of a few pH or even lower can be achieved, which is essential for obtaining very low values for S_Φ (Ref. [168]). The rms flux noise for the SQUID used here is $S_\Phi^{1/2} \approx 220 \text{ n}\Phi_0/\sqrt{\text{Hz}}$ (in the white noise limit above $\approx 1 \text{ kHz}$). This value was measured in a separate, magnetically and electrically shielded setup, using a sensitive cryogenic amplifier for SQUID readout. The nanoSQUID is mounted in a vacuum chamber (pressure $< 1 \times 10^{-6} \text{ mbar}$) at the bottom of a continuous-flow ^3He cryostat. The SQUID is biased at a current I slightly above its critical current and at a magnetic flux $\Phi_{mod} \propto I_{mod}$ coupled via the modulation current I_{mod} to the loop (cf. Fig. 6.1). To maintain operation of the SQUID at its optimum working point, i.e., at the maximum slope of its $V(\Phi)$ curve, we use a flux-locked loop (FLL) with a room-temperature voltage preamplifier. The FLL couples a feedback flux $\Phi_f = -\Phi$ to compensate for any flux signal Φ . Using such a scheme, the output voltage $V_{out} \propto I_{mod}$ provided by the feedback loop is directly proportional to Φ ; in our case $V_{out}/\Phi = 2.55 \text{ V}/\Phi_0$.

6.3. Low temperature magnetic force microscopy setup

The magnetic tip used in our LTMFM setup is a $l = 6\text{-}\mu\text{m}$ long Ni NT which is fabricated by the atomic layer deposition of Ni and a $\approx 25\text{-nm}$ thick AlO_x interlayer on a 75-nm diameter GaAs

nanowire [22]. The outer diameter $D_a = (190 \pm 35) \text{ nm}^a$, yielding a thickness $t = (32.5 \pm 17.5) \text{ nm}$ of the Ni layer and hence a volume of the Ni tube $V_{Ni} = (0.096 \pm 0.063) \mu\text{m}^3$. The Ni NT is affixed parallel to the cantilever axis (z axis) such that it protrudes from the cantilever end by $4 \mu\text{m}$. We define the position $\mathbf{r} = (x, y, z)$ of the Ni tip (relative to the SQUID) as the intersection point of its cylindrical axis with the bottom end of the tube. The cantilever hangs above the SQUID in the pendulum geometry, i.e., perpendicular to the scanned surface (in the x - y plane; cf. Fig. 6.1) [169]. A three-dimensional (3D) piezoelectric positioning stage (Attocube Systems AG) moves the SQUID relative to the Ni nanomagnet. In noncontact scanning force microscopy, the above-described configuration prevents the tip of the cantilever from snapping into contact with the sample surface and thus allows for the use of particularly soft—and therefore sensitive—cantilevers (spring constant $\leq 1 \text{ mN/m}$). Similar setups were used in experiments investigating noncontact friction between closely spaced bodies [28] and ultrasensitive magnetic resonance force microscopy [170]. The single-crystal Si cantilever used here is $120\text{-}\mu\text{m}$ long, $4\text{-}\mu\text{m}$ wide, and $0.1\text{-}\mu\text{m}$ thick and includes a $15\text{-}\mu\text{m}$ long, $1\text{-}\mu\text{m}$ thick mass on its end; for details see Ref. [119]. The oscillation of the lever along the y direction is detected using laser light focused onto a $10\text{-}\mu\text{m}$ wide paddle near the mass-loaded end and reflected back into an optical fiber interferometer [171]. One hundred nW of light are incident on the paddle from a temperature-tuned 1550-nm distributed feedback laser diode.

At temperature $T = 4.3 \text{ K}$ and applied magnetic field $H = 0$, the nanomagnet-loaded cantilever has a resonance frequency $f_{res} = 3413 \text{ Hz}$ and an intrinsic quality factor $Q_0 = 3.4 \times 10^4$. Its spring constant is determined to be $k = 90 \mu\text{N/m}$ through measurements of its thermal noise spectrum at several different temperatures. As a result, far from the SQUID, where surface interactions do not play a role [28, 172], the cantilever has a thermally limited force sensitivity of $10 \text{ aN}/\sqrt{Hz}$. Note that under ambient conditions a MFM with such a soft cantilever, operated in the shear mode, high resolution images of the topography are hard to obtain [173]. However, at very low temperature and pressure as used for the present work, the vibrating amplitudes of the cantilevers are very low. If the mean energy of the cantilever $k_B T$ (k_B is the Boltzmann constant) is converted to a mean displacement fluctuation $\langle y^2 \rangle = k_B T/k$, we infer a displacement noise $< 1 \text{ nm}/\text{Hz}^{1/2}$. The interferometric cantilever deflection signal is fed through a field programmable gate array (FPGA) (National Instruments) circuit back to a piezoelectric element which is mechanically coupled to the cantilever. In this way, it is possible to selfoscillate the cantilever at its fundamental resonance frequency and at a desired amplitude.

We produce noncontact force microscopy images by scanning (in the $x - y$ plane for fixed z) the position of the nanomagnet-tipped cantilever over the SQUID and simultaneously measuring the cantilever resonance frequency $f_{res}(x, y)$, which is proportional to the force gradient $\partial F_y / \partial y$ acting on the nanomagnet-tipped cantilever. Although no feedback is used to stabilize the cantilever position, the system is stable against mechanical drift of a few nanometers within times relevant to the measurements presented here. From such images we can identify the topography of the nanoSQUID, allowing us to precisely position the Ni NT with respect to the nanoSQUID. At the same time, due to the magnetization of the Ni NT tip, the images show features produced by the diamagnetic response of the superconductor.

^aThe determination of D_a for the tube investigated here was not possible, as the tube was lost during warm up after our measurements. Instead, we determined D_a for six other tubes from the same batch by SEM. Those had values of D_a varying from $155 - 225 \text{ nm}$ with a variation in D_a of $10 - 20 \text{ nm}$ along a single tube.

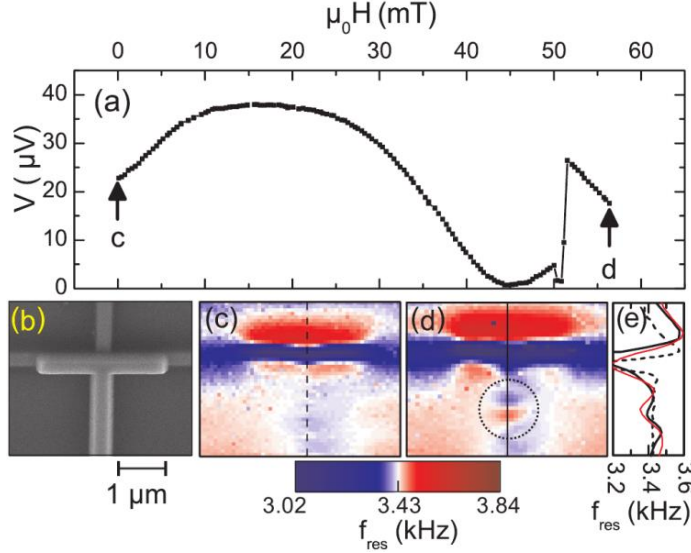


Figure 6.2. | MFM imaging of trapped flux: (a) $V(H)$ for a single sweep from 0 to 56 mT; labels c,d indicate field values for LTMFM images shown in (c) and (d), respectively. (b) SEM image of the nanoSQUID. LTMFM images $f_{res}(x, y)$, (c) without trapped vortices at $H = 0$ and (d) with a trapped vortex (indicated by dotted circle) at $\mu_0 H = 56$ T. (e) line scans along dashed line in (c) (dashed curve), solid line in (d) (solid curve) and calculated response for the SQUID with a trapped vortex along solid line in (d) (red curve).

6.4. Magnetic force microscopy imaging of an Abrikosov vortex

Prior to the measurements of the magnetic flux coupled by the Ni tip to the SQUID, we investigate a possible impact of an applied magnetic field on the nanoSQUID. In particular, Abrikosov vortices that may enter the superconducting areas are a severe problem for nanoSQUID magnetometry since such vortices (i) can degrade the SQUID performance and (ii) generate spurious magnetic signals and therefore mimic a magnetic behavior not related to the sample under investigation. In this section we show that with the presented sensor system an *in situ* detection of Abrikosov vortices is possible. H is aligned along the z direction, with a possible tilt of a few degrees. The trapping of a vortex appears as a voltage jump in the periodic $V(H)$ characteristics, when the SQUID voltage is measured directly, rather than using the FLL readout. Note that the SQUID voltage oscillates with increasing H due to the nonperfect alignment of H along the z direction, i.e., H has a finite in-plane component, which induces magnetic flux threading the SQUID loop. From the effective area of the SQUID and the oscillation period of $V(H)$, we estimate a tilt of the applied field of $\approx 2^\circ$ with respect to the z axis. An example for a vortex trapping process is shown in Fig. 6.2(a), where a huge jump in $V(H)$ occurs near $\mu_0 H = 50$ mT. This observation is consistent with a strong jump (decrease) in the critical current versus applied field near $\mu_0 H = 50$ mT, which we observed for another Nb nanoSQUID with the same layout [163]. We note that during the field sweep, the Ni tip was retracted from the SQUID. For further improvement of the SQUID layout the knowledge of the position of trapped vortices is indispensable. The ability of the LTMFM setup to image stray fields can be used to visualize vortices in the superconductors as well as the magnetic field of the screening currents of the nanoSQUID itself. In Fig. 6.2(d), taken at a magnetic field above the jump in $V(H)$, such a vortex is visible in the superconducting lead (top Nb layer) of the nanoSQUID. The vortex appears as a distortion in the otherwise flat resonance

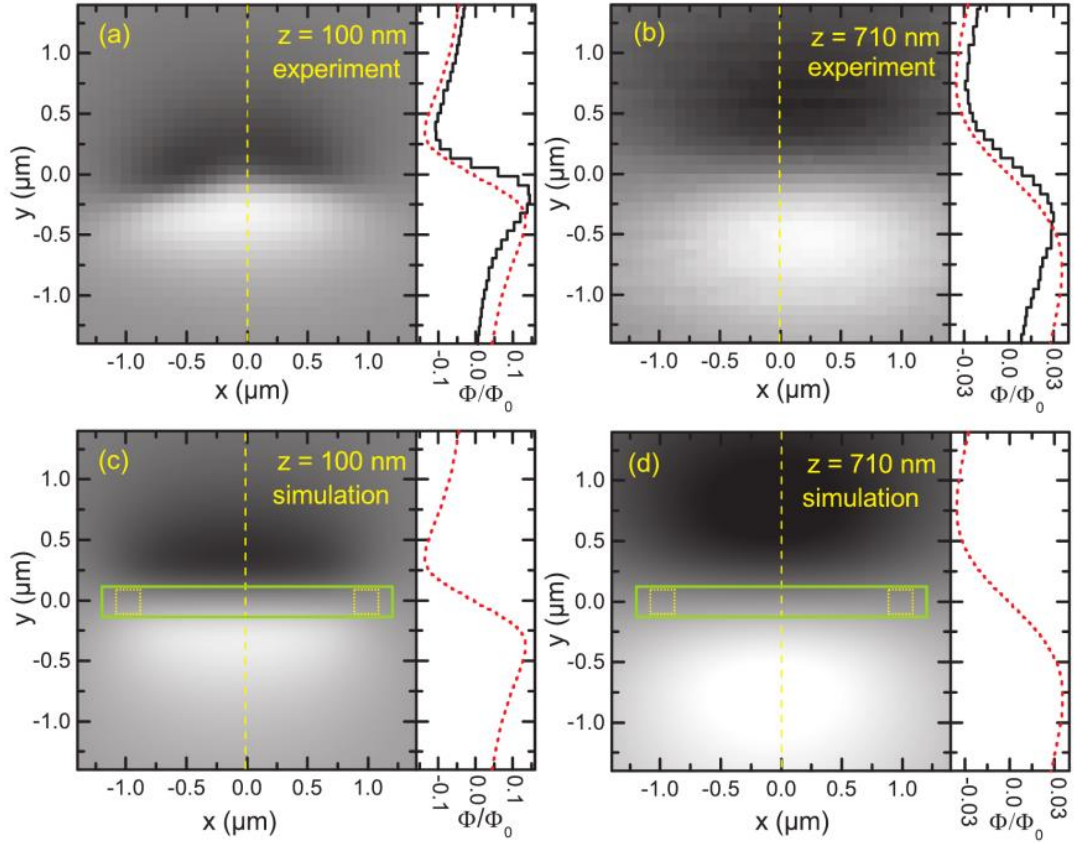


Figure 6.3. | Magnetic flux Φ generated in the SQUID vs $x - y$ position of the Ni NT (magnetized along z axis). In (c) and (d), solid rectangle and dotted squares indicate position of the SQUID and the two JJ, respectively. Vertical dashed lines indicate position of line scans $\Phi(y)$ to the right of each image. (a,b) Upper graphs show experimental results and (c,d) lower graphs show corresponding simulation results, using Eq. 7.1 for $z = 100$ nm (left graphs) and $z = 710$ nm (right graphs). For the simulation we assumed $M_s = 408$ kA/m and $V_{Ni} = 0.047 \mu\text{m}^3$. Line scans in (a,b) also include calculated line scans from (c,d).

frequency f_{res} distribution along the Nb line [cf. line scans in Fig. 6.2(e)]. In the given setup $\Delta f_{res} \propto \partial^2 B_M / \partial y^2$; here B_M is the projection of the flux density along the magnetization axis of the Ni tube, which is very close to the z axis. Hence, for an undisturbed vortex a symmetric tripolar response is expected. The solid red line in Fig. 6.2(e) shows a line scan along the solid line in Fig. 6.2(d) of the expected vortex signal calculated with 3D-MLSI. From this simulation, we identify the origin of the deviations from the expected symmetric tripolar signal to be the current distribution inside the superconducting structures. In contrast, at fields below the jump the trapped vortex is absent [see Fig. 6.2(c)]. For the subsequent investigations, we operate the SQUID in nominally zero field only, i.e., trapped vortices do not play a role.

6.5. Experimental determination of the spatial flux signal dependence

To determine $\Phi(\mathbf{r})$ we measure the nanoSQUID signal, i.e., the magnetic flux Φ through the SQUID loop as a function of the Ni NT position (x, y) for fixed z . Such measurements produce

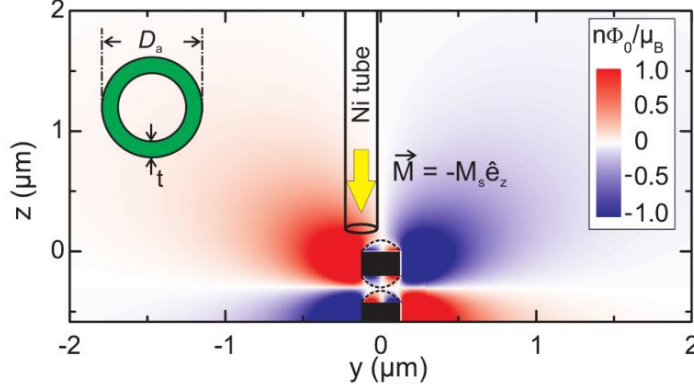


Figure 6.4. | Calculated coupling factor ϕ_μ in the $y-z$ plane ($x=0$) for a point-like magnetic particle with magnetic moment $\boldsymbol{\mu}$ along $-\hat{e}_z$. Black rectangles indicate position of the Nb top and bottom layer; dotted lines include regions for which the simulations produce unphysical results (For simulating the current distribution, we have to assume that the currents are flowing in surface sheets rather than across the entire width of the two Nb lines (in the y direction). This assumption allows for coupling of flux between the surface sheets, which produces the localized minima and maxima very close to the two SQUID arms, as visible here). A sketch of the bottom part of the Ni NT (drawn to scale) is shown within the coupling map to illustrate the spatial dependence of the coupling factor within the volume of the tube. Upper left inset schematically shows a zoomed cross section of the Ni NT.

images $\Phi(x, y)$ of the spatially dependent magnetic coupling of the Ni NT to the nanoSQUID. The experiment was performed in the following way: First, we bring the Ni NT into a well-defined saturated magnetic state along its easy axis. This is done by a half magnetization cycle, i.e., a sweep of H (aligned along z direction, as above) from zero to $\mu_0 H_{max} = -150$ mT and back to $H = 0$. From previous experiments, we know that H_{max} is strong enough to saturate the magnetization of the Ni NT [22, 30]. To avoid trapped flux in the SQUID, the magnetization cycle is performed at $T = 14$ K, i.e., significantly above the transition temperature $T_c \approx 9$ K of the Nb SQUID. Subsequently, we zero-field cool the SQUID to its operation temperature $T = 4.3$ K, and then set up the FLL readout for the SQUID. Even for a worst case scenario, i.e., maximum modulation and screening currents, the resulting magnetic field applied to the NT by the SQUID currents is less than 5 mT, which is well below the coercive field of the NT. We therefore assume a fully saturated NT for subsequent results. For various distances z between the tip and the top Nb layer of the SQUID we make scans in the x - y plane with a scan range of about $6 \times 7 \mu\text{m}^2$ corresponding to 81×81 pixels. The scans start at the largest distance of $z \approx 700$ nm. In steps of 50 nm the distance is subsequently reduced until the tip touches the top Nb layer of the SQUID (at $z = 0$), which is detected as a loss of the oscillation of the cantilever. The touchpoint is also necessary for the calibration of the $z = 0$ position.

Figures 6.3(a) and 6.3(b) shows two representative $\Phi(x, y)$ images taken at (a) $z = 100$ nm and (b) $z = 710$ nm. The images show a bipolar flux response, i.e., when the tip crosses the SQUID loop the flux signal is inverted. For the closer distance [Fig. 6.3(a)] the induced flux is stronger and spatially more confined as compared with the larger distance [Fig. 6.3(b)]. At $z = 100$ nm, we obtain $\Delta\Phi = \Phi_{max} - \Phi_{min} \approx 0.26 \Phi_0$, with the positions of the maximum Φ_{max} and minimum Φ_{min} in the line scan $\Phi(y)$ (at $x = 0$) being separated by $\Delta y = 370$ nm. For $z = 710$ nm, we find $\Delta\Phi \approx 0.06 \Phi_0$ and $\Delta y = 750$ nm [cf. black solid lines in the right panels in Figs. 6.3(a) and 6.3(b)].

6.6. Analysis with spatial dependent coupling factor

To analyze the measured flux signals, we start from numerical simulations of $\phi_\mu(\hat{e}_\mu \mathbf{r}_p)$ for a point-like SMP with orientation \hat{e}_μ of its magnetic moment at position \mathbf{r}_p in the 3D space above the SQUID loop [117, 156]. This routine takes explicitly into account the geometry in the plane of the SQUID loop, and is based on the numerical simulation of the two-dimensional (2D) sheet current density in the SQUID loop, using London theory [174].

Figure 6.4 shows the calculated coupling factor ϕ_μ in the $y-z$ plane, with the SQUID loop in the $x-z$ plane and the magnetic moment pointing along the $-z$ direction. ϕ_μ decreases with increasing distance from the SQUID loop and inverts when crossing the SQUID loop. This spatial dependence has a strong impact on the magnetic flux $\Phi(\mathbf{r})$ which is coupled by a Ni NT (at position \mathbf{r}) with finite size into the SQUID. For the calculation of $\Phi(\mathbf{r})$ we integrate ϕ_μ over the volume V_{Ni} of the Ni NT at position \mathbf{r} and multiply this with the Ni saturation magnetization M_s , i.e.,

$$\Phi(\mathbf{r}) = M_s \int_{V_{Ni}(\mathbf{r})} \phi_\mu(\mathbf{r}_p) dV, \quad (6.1)$$

assuming a homogeneous M_s over the entire volume of the Ni NT. Figures 6.3(c) and 6.3(d) show flux images $\Phi(x, y)$ calculated from Eq. (1) for $z = 100$ and 710 nm, respectively, with a saturation magnetization M_s along the $-z$ direction (cf. Fig. 6.4). The bipolar flux response and the positions of the minima Φ_{min} and maxima Φ_{max} in Φ_y (for $x = 0$) are reproduced well by the simulations [cf. dotted lines in the right panels in Figs. 6.3(c) and 6.3(d), which are also shown for comparison with the experimental data in the right panels of Figs. 6.3(a) and 6.3(b)]. For a quantitative analysis, Fig. 6.5 compares experimentally obtained Φ_{min} and Φ_{max} for all investigated distances to the simulated ones. From previous work on similar Ni NTs [30], we know that the saturation magnetization is equal within the experimental 20 % error to the bulk value known from the literature $M_s = 408$ kA/m (Ref. [34]). A much larger uncertainty in the absolute values for Φ , calculated from Eq. 7.1, comes from the uncertainty in the volume V_{Ni} of the Ni tube due to the large margins for the Ni thickness t and hence the outer diameter D_a . Therefore, we fixed $M_s = 408$ kA/m and used t as an adjustable parameter to obtain the best quantitative agreement between the experiment and calculation, which we obtained for $t = 17.5$ nm, corresponding to $D_a = 160$ nm and $V_{Ni} = 0.047 \mu\text{m}^3$. This value is significantly smaller than the mean value for V_{Ni} of other Ni tubes from the same batch as quoted above. However, it is still within the large uncertainty for V_{Ni} . Furthermore, an independent determination of V_{Ni} on the same Ni tube, via cantilever magnetometry, yields a value which is even somewhat below the one obtained via SQUID measurement. We note that the formation of a multidomain state close to the bottom of the Ni tube is unlikely, as hysteresis curves $M(H)$ measured both with SQUID and cantilever magnetometry indicate no reduction of the magnetic signal upon sweeping H from $+H_{max}$ back to zero. In the experiment we also find an asymmetry in $\Phi(y)$, i.e., $\Phi_{max} \geq |\Phi_{min}|$. This effect is most likely caused by flux focusing effects of the feed lines in the top and bottom Nb layers, which are not considered in the simulations. The flux focusing effects are also visible in the distorted flux image (broken horizontal symmetry) in Fig. 6.3(a). An additional asymmetry may be caused by a slightly tilted tube with respect to the SQUID plane. In our case, however, this effect is considered to be small since the tilt angle is measured to be less than 5° . To conclude this section, we note that the measured flux coupled from the Ni tube to the nanoSQUID confirms our simulation routine for the coupling factor ϕ_μ within the experimental error of ≈ 2 , which is due to the relatively large uncertainty in the thickness of the Ni tube.

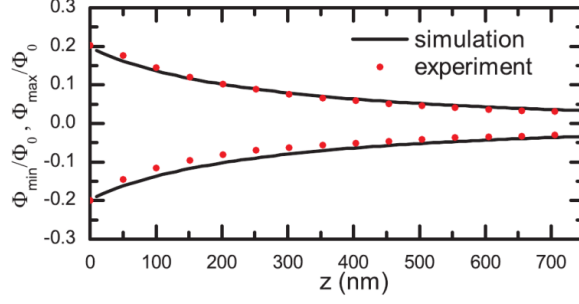


Figure 6.5. | Experimental and simulated minimum and maximum flux signals Φ_{min} and Φ_{max} , versus distance z . For the simulation we assume $M_s = 408$ kA/m and $V_{Ni} = 0.047$ μm^3 .

6.7. Displacement detection

Finally, we discuss the sensitivity of our setup for the detection of the oscillatory motion of the cantilever by the SQUID [175, 176]. While the absolute flux signal from the Ni NT is optimally detected at the positions yielding Φ_{max} and Φ_{min} , for the cantilever displacement detection, a large gradient $\partial\Phi/\partial y$ is required. The line scans in Fig. 6.3 clearly show that the optimum position for displacement detection is directly above the SQUID. For our device, we find for $z = 50$ nm a gradient $\Phi_y \equiv \partial\Phi/\partial y = 2 \times 10^6$ Φ_0/m . With the flux noise $S_\Phi^{1/2} \approx 220$ $n\Phi_0/\sqrt{Hz}$, this yields an extremely low value for the predicted displacement sensitivity $S_r^{1/2} = S_\Phi^{1/2}/\Phi_y = 110$ fm/\sqrt{Hz} , which is already a factor of 2 below the best value found in the literature [175–177]. Still, S_r is by far not optimized and could be further improved by using a reduced linewidth for the SQUID arm in the top Nb layer and by increasing the number of spins in the magnet.

6.8. Conclusion

In conclusion, we experimentally determined the spatial dependence of the magnetic coupling between a Ni NT and a Nb nanoSQUID. Operating the nanoSQUID in a flux locked loop, we measured the flux through the SQUID loop $\Phi(\mathbf{r})$ generated by the Ni NT during the scan of the tip in 3D space above the nanoSQUID. This yields experimental information on the magnetic coupling factor ϕ_μ , which together with the flux sensitivity determines the spin sensitivity as the figure of merit for small magnetic particle detection by a nanoSQUID. Our results are in good agreement with a recently developed routine for numerical calculation of the coupling factor between a small magnetic particle and a nanoSQUID. This provides an important step toward the development of optimized nanoSQUIDs for the investigation of small magnetic particles. With the presented measurement system, we demonstrate a reliable and nondestructive *in situ* tool for the challenging task of positioning a nanoscaled magnet to the position of highest coupling of a nanoSQUID. Furthermore, with a proper readout technique, our highly flux-sensitive nanoSQUID can be used for displacement detection of the cantilever in an MFM with extremely good displacement sensitivity, which still can be further improved. By using an MFM imaging mode, we also demonstrate the imaging of Abrikosov vortices, which are trapped at high magnetic fields in the superconducting leads of the nanoSQUID. This technique is not only useful for the improvement of the high-field suitability of nanoSQUIDs, but even more

importantly allows for the *in situ* differentiation between a signal originating from a SMP and a signal due to the entrance of a spurious Abrikosov vortex. Finally, we demonstrate the use of a nanoSQUID as a local probe of the stray fields produced by the Ni NT, which may be of great importance in understanding magnetization reversal in these magnetic nanostructures [178]. Such investigations will be the subject of future work as will investigations of other SMPs.

7. Reversal mechanism of an individual Ni nanotube simultaneously studied by torque and SQUID magnetometry

Adapted from:

A. Buchter, J. Nagel, D. Ruffer, F. Xue, D. P. Weber, O. F. Kieler, T. Weimann, J. Kohlmann, A. B. Zorin, E. Russo-Averchi, R. Huber, P. Berberich, A. Fontcuberta i Morral, M. Kemmler, R. Kleiner, D. Koelle, D. Grundler, and M. Poggio,
”Reversal mechanism of an individual Ni nanotube simultaneously studied by torque and SQUID magnetometry”,
Phys. Rev. Lett. **111**, 067202 (2013)

Using an optimally coupled nanometer-scale SQUID, we measure the magnetic flux originating from an individual ferromagnetic Ni NT attached to a Si cantilever. At the same time, we detect the NT’s volume magnetization using torque magnetometry. We observe both the predicted reversible and irreversible reversal processes. A detailed comparison with micromagnetic simulations suggests that vortex-like states are formed in different segments of the individual NT. Such stray-field free states are interesting for memory applications and non-invasive sensing.

7.1. Introduction

Recent experimental and theoretical work has demonstrated that nanometer-scale magnets, as a result of their low-dimensionality, display magnetic configurations not present in their macroscopic counterparts [148, 150, 151]. Such work is driven by both fundamental questions about nanometer-scale magnetism and the potential for applying nanomagnets as elements in high-density memories [7], in high-resolution imaging [179–181], or as magnetic sensors [182]. Compared to nanowires, ferromagnetic NTs are particularly interesting for magnetization reversal as they avoid the Bloch point structure [9]. Different reversal processes via curling, vortex wall formation, and propagation have been predicted [12, 13, 24, 183]. Due to their inherently small magnetic moment, experimental investigations have often been conducted on large ensembles. The results, however, are difficult to interpret due to stray-field interactions and the distribution in size and orientation of the individual NTs [15, 16, 24, 26, 184, 185]. In a pioneering work, Wernsdorfer *et al.* [31] investigated the magnetic reversal of an individual Ni nanowire at 4 K using a miniaturized SQUID. Detecting the stray magnetic flux Φ from one end of the nanowire as a function of magnetic field \mathbf{H} , Φ was assumed to be approximately proportional to the projection of the total magnetization \mathbf{M} along the nanowire axis. At the time, $M(H)$ of the individual nanowire was not accessible and micromagnetic simulations were conducted only a decade later [9].

Here we present a technique to simultaneously measure $\Phi(H)$ and $M(H)$ of a single low-dimensional magnet. Using a scanning nanoSQUID and a cantilever-based torque magnetometer (Fig. 7.1) [186], we investigate a Ni NT producing $\Phi(H)$ with a nearly square hysteresis, similar to the Ni nanowire of Ref. [31]. $M(H)$, however, displays a more complex behavior composed of reversible and irreversible contributions, which we interpret in detail with micromagnetic simulations. In contrast to theoretical predictions, the experiment suggests that magnetization reversal is not initiated from both ends. If nanomagnets are to be optimized for storage or sensing applications, such detailed investigations of nanoscale properties are essential.

7.2. Setup and methods

We use a direct current nanoSQUID formed by a loop containing two superconductor-normal-superconductor Josephson junctions (JJs) (see Appendix A) [117, 163] (Fig. 7.1 (a)). Two T-shaped superconducting Nb arms are sputtered on top of each other separated by an insulating layer of SiO₂. The Nb arms are connected via two planar 225-nm-thick Nb/HfTi/Nb JJs each with an area of 200×200 nm². These JJs and the 1.8- μ m-long Nb leads form a SQUID loop in the xz -plane (shown in yellow in Fig. 7.1 (a)), through which we measure Φ . Atomic layer deposition of Ni is used to prepare the NT around a GaAs nanowire template grown by molecular beam epitaxy (MBE) [22, 30]. The GaAs core supports the structure, making it mechanically robust. The polycrystalline NT, which does not exhibit magneto-crystalline anisotropy, has a 140 ± 20 -nm outer diameter, a 70 ± 10 -nm inner diameter, and a 6.0 ± 0.5 - μ m length. The error in the diameters results from the roughness of the Ni film (see Appendix A). The Ni NT is affixed to the end of an ultrasoft Si cantilever [30], such that it protrudes from the tip by 4 μ m. The cantilever is 120- μ m-long, 4- μ m-wide and 0.1- μ m-thick. It hangs above the nanoSQUID in the pendulum geometry, inside a vacuum chamber (pressure $< 10^{-6}$ mbar) at the bottom of a cryostat. A 3D piezo-electric positioning stage moves the nanoSQUID relative

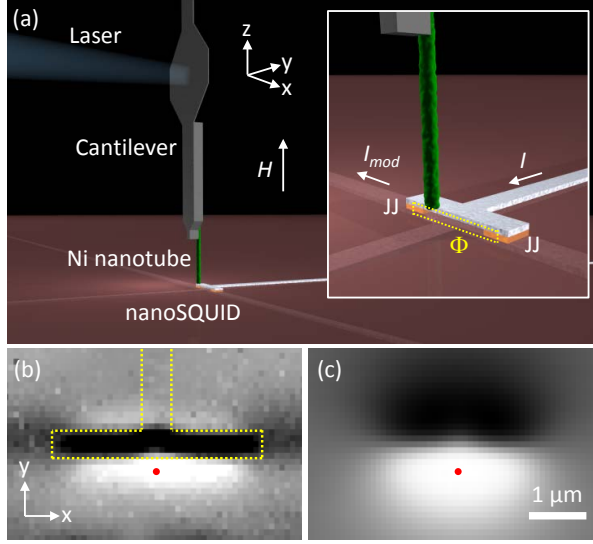


Figure 7.1. | (a) Sketch of the apparatus (inset: zoomed-in view; dashed line indicates SQUID loop). Gray-scale maps of (b) $\Delta f(x, y)$ and (c) $\Phi(x, y)$ taken simultaneously at a distance $z = 280$ nm with $H = 0$. Δf (Φ) ranges from -170 to 430 Hz ($-0.08 \Phi_0$ to $0.08 \Phi_0$). Dashed lines indicate the T-shaped SQUID arm and dots the operating position.

to the Ni NT and an optical fiber interferometer is used to detect deflections of the cantilever along \hat{y} [171].

Fast and accurate measurement of the cantilever's fundamental resonance frequency f_c is realized by self-oscillation at a fixed amplitude. An external field $\mu_0 \mathbf{H}$ of up to 2.8 T can be applied along the cantilever axis \hat{z} using a superconducting magnet. At 4.3 K and $\mu_0 H = 0$, the cantilever, loaded with the Ni NT and far from any surfaces, has an intrinsic resonance frequency $f_c = f_0 = 3413$ Hz, a quality factor $Q = Q_0 = 3.4 \times 10^4$, and spring constant of $k_0 = 90 \pm 10 \mu\text{N/m}$.

The magnetic flux due the Ni NT $\Phi_{\text{NN}}(H)$ is evaluated from $\Phi_{\text{NN}}(H) = \Phi(H) - \Phi_{\text{ref}}(H)$, where the flux $\Phi(H)$ is measured with the NT close to the nanoSQUID, while $\Phi_{\text{ref}}(H)$ is measured with the NT several μm away such that the stray flux is negligible. Therefore $\Phi_{\text{ref}}(H) \propto H$, due to the small fraction of \mathbf{H} that couples through the nanoSQUID given its imperfect alignment with \hat{z} . Once calibrated, we also use $\Phi_{\text{ref}}(H)$ to measure the $\mu_0 H$ axis of our plots, removing effects due to hysteresis in the superconducting magnet. Such a field calibration was not possible for the integrated SQUID of Ref. [31]. We also perform dynamic-mode cantilever magnetometry [28], which is sensitive to the dynamic component of the magnetic torque acting between \mathbf{H} and the magnetization \mathbf{M} of the Ni NT. In order to extract $M(H)$, we measure the field-dependent frequency shift $\Delta f(H) = f_c(H) - f_0$. Micromagnetic simulations are performed with NMAG [187] which provides finite-element modeling by adapting a mesh to the curved inner and outer surfaces of the NT. We simulate 30-nm thick NTs of different lengths l and the same 70-nm inner diameter. We assume magnetically isotropic Ni consistent with earlier studies [22], a saturation magnetization $M_S = 406$ kA/m [34], and exchange coupling constant of 7×10^{12} J/m [188].

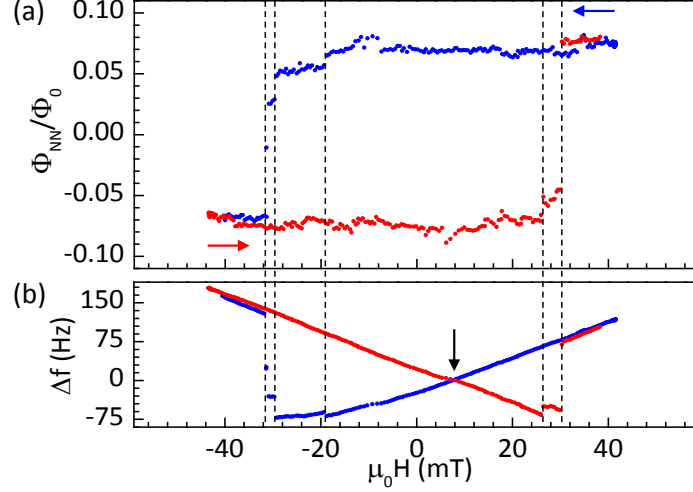


Figure 7.2. | Simultaneously measured hysteresis loops of (a) $\Phi_{\text{NN}}(H)$ and (b) $\Delta f(H)$ at $z = 450$ nm. Red (blue) points represent data taken while sweeping H in the positive (negative) direction. Dashed lines indicate discontinuities (magnetic switching fields $H_{\text{sw},e}$) appearing in both $\Phi_{\text{NN}}(H)$ and $\Delta f(H)$.

7.3. SQUID magnetometry

We first scan the nanoSQUID under the cantilever with attached Ni NT, to map the coupling between them. To ensure that the scan is done with the NT in a well-defined magnetic state, we first saturate it along its easy axis (\hat{z}). Scans are then made at $H = 0$ in the xy -plane at a fixed height z , i.e. for a fixed distance between the top of the SQUID device and the bottom end of the Ni NT. $\Delta f(x, y) = f_c(x, y) - f_0$ and $\Phi(x, y)$ are measured simultaneously, as shown in Fig. 7.1 (b) and (c) respectively. $\Delta f(x, y)$ is proportional to the force gradient $\partial F_y / \partial y$ acting on the cantilever and is sensitive to both the topography of the sample and to the magnetic field profile in its vicinity. Raised features such as the T-shaped top-electrode of the nanoSQUID are visible. $\Phi(x, y)$ shows a bipolar flux response. The change in sign of $\Phi(x, y)$ occurs as the Ni NT crosses the xz -plane (defined by the SQUID loop) above the nanoSQUID, matching the expected response. Such images allow us to identify the nanoSQUID and to position the Ni NT at a maximum of $|\Phi(x, y)|$. Given a constant z , the NT stray flux optimally couples through the nanoSQUID loop at such positions, resulting in the maximum signal-to-noise ratio for flux measurements.

At one such position, indicated by the dot in Fig. 7.1, we record $\Phi(H)$ by sweeping $\mu_0 H$ from 41 mT to -41 mT and vice versa. A representative hysteresis curve $\Phi_{\text{NN}}(H) = \Phi(H) - \Phi_{\text{ref}}(H)$ is shown in Fig. 7.2 (a) where $\Phi(H)$ is measured at $z = 450$ nm. $\mu_0 |H|$ is incremented in steps of 0.2 mT with a wait time of 1 s before each acquisition. The hysteresis has an almost square shape with a maximum flux $\Phi_{\text{NN}} = 75 \text{ m}\Phi_0$ coupled into the nanoSQUID. The loop appears similar to stray-field hysteresis loops obtained from a bistable Ni nanomagnet [189] and the Ni nanowire of Ref. [31], where H was collinear with the long axis. Such a shape may suggest that at $H = 0$ the remanent magnetization $M_{\text{R}} \approx M_{\text{S}}$. Increasing H from zero (see red branch in Fig. 7.2 (a)), we first observe a nearly constant flux, then a variation by about 30 % along with tiny jumps in a small field regime, and finally a large jump occurring near 30 mT. Similar to Ref. [31], our SQUID data suggest that almost all magnetic moments are reversed at once near 30 mT via a large irreversible jump, i.e. via domain nucleation and propagation.

7.4. High and low field characterization with DCM

We now turn to cantilever magnetometry, which is sensitive to $M(H)$. Δf is first measured simultaneously with $\Phi(H)$ at $z = 450$ nm, as shown in Fig. 7.2 (b). The torque measured via Δf is found to exhibit tiny jumps and large abrupt changes at exactly the same switching fields $H_{\text{sw,e}}$ as $\Phi_{\text{NN}}(H)$. We note that switching fields vary from sweep to sweep (compare Appendix A) as was observed in the Ni nanowire of Ref. [31]; such behavior is expected if nucleation is involved, given its stochastic nature. Importantly, there is always a one-to-one correspondence between switching fields observed in Δf and flux Φ_{NN} as highlighted by the dashed lines in Fig. 7.2. This correlation confirms that the changes in Δf and Φ_{NN} have a single origin: the reversal of magnetic moments within the Ni NT.

In order to analyze $\Delta f(H)$ in terms of $M(H)$ it is important to retract the Ni NT from the nanoSQUID by several μm . We therefore avoid magnetic interactions with both the diamagnetic superconducting leads and the modulation current of the nanoSQUID. These interactions lead to an enhanced Δf and a branch crossing (indicated by an arrow in Fig. 7.2 (b)) occurring at finite H rather than at $H = 0$ as was reported in Ref. [22]. After retracting the NT from the nanoSQUID, we measure $\Delta f(H) = f_c(H) - f_0$ as shown in Fig. 7.3. We start the acquisition at a large positive field ($\mu_0 H = 2.8$ T), where the NT is magnetized to saturation and then reduce H to zero as shown in Fig. 7.3 (a). In large fields, the NT behaves as a single-domain magnetic particle, i.e. it is magnetized uniformly and M rotates in unison as the cantilever oscillates in the magnetic field. Based on this assumption, we fit the results with an analytical model for $\Delta f(H)$ [30]. The volume of the Ni NT V_{Ni} , ω_0 , and k_0 are set to their measured values, while the saturation magnetization $M_S = 300 \pm 200$ kA/m and the anisotropy parameter $K = 40 \pm 20$ kJ/m³ are extracted as fit parameters. The error in these parameters is dominated by the error associated with the measurement of the NT's exact geometry and therefore of V_{Ni} (see Appendix A). M_S is consistent with the findings of Ref. [30] on similar NTs and with 406 kA/m, known as the saturation magnetization for bulk crystalline Ni at low temperature [34]. Figure 7.3 (b) shows $\Delta f(H)$ taken in the low-field regime. In an opposing field, we observe discrete steps in $\Delta f(H)$ indicating abrupt changes in the volume magnetization M . As expected the branch crossing (arrow) occurs at $H = 0$ and the overall behavior is consistent with measurements of similar NTs [30]. To analyze the low field data, we adapt the analytical model to extract the dependence of the volume magnetization M on H , i.e. the field dependence of magnetization averaged over the entire volume of the NT. Solving the equations of Ref. [30] describing the frequency shift for M , we find:

$$M = \frac{2k_0 l_e^2 K \Delta f}{H (K V_{\text{Ni}} f_0 - k_0 l_e^2 \Delta f)}, \quad (7.1)$$

where $l_e = 85$ μm is the effective cantilever length for the fundamental mode. $M(H)$ extracted from Fig. 7.3 (b) is plotted in Fig. 7.3 (c). In both field sweep directions, the magnetization is seen to first undergo a gradual decrease as $|H|$ decreases. Starting from ~ 300 kA/m at +40 mT, M reduces to ~ 200 kA/m at 0 mT. We find $M_R \approx 0.65 M_S$, in contrast with the SQUID data suggesting $M_R \approx M_S$. However, this gradual change of M at small $|H|$ in the initial stage of the reversal is consistent with the gradually changing anisotropic magnetoresistance observed in a similar NT of larger diameter in nearly the same field regime [22]. At -15 mT, just before the first of three discontinuous jumps, M is only ~ 100 kA/m. Note that jumps are seen after the magnetization has decreased to a value of about $0.3 M_S$. Two further jumps occur at $\mu_0 H_{\text{sw,e}} = -28$ and -33 mT. For $\mu_0 H < -40$ mT, the NT magnetization is completely reversed.

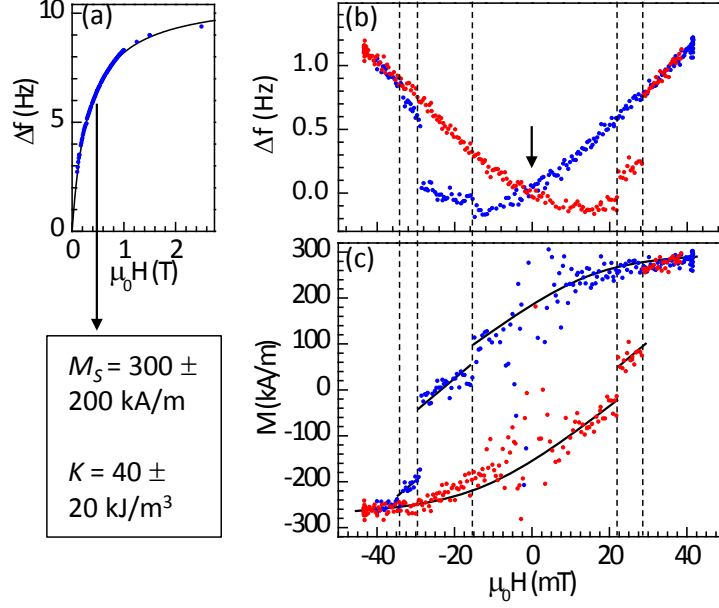


Figure 7.3. | (a) Cantilever magnetometry (points) and fit (solid line) in large magnetic fields. (b) Cantilever magnetometry at small fields. (c) Volume magnetization M extracted from (b) according to (7.1). Solid lines guide the eye. Red (blue) points represent data taken while sweeping H in the positive (negative) direction. Dashed lines highlight switching fields $H_{sw,e}$. The error in M scales with $1/|H|$, explaining the scatter near $H = 0$.

We observe a somewhat asymmetric behavior at positive and negative fields. This asymmetry may be due to an anti-ferromagnetic NiO surface layer providing exchange interaction with the Ni NT [190, 191]. Irreversible jumps in M are observed for $15 \text{ mT} < \mu_0 |H_{sw,e}| < 35 \text{ mT}$ in Fig. 7.3, in perfect agreement with the range over which jumps occur in Φ_{NN} with the NT close to the nanoSQUID in Fig. 7.2.

The observed magnetization steps suggest the presence of 2 to 4 intermediate magnetic states or 2 to 4 segments in the NT that switch at different H . Calculations for ideal NTs [183] suggest that the intermediate states should be multi-domain, consisting of uniform axially saturated domains separated by azimuthal or vortex-like domain walls. The preferred sites for domain nucleation are expected to be the two ends of the NT [9, 183]. As the field is reduced after saturation, magnetic moments should gradually curl or tilt away from the field direction. The torque magnetometry measurements, which show both gradual and abrupt changes in $M(H)$, are consistent with such gradual tilting; the SQUID data, showing only abrupt changes in $\Phi_{NN}(H)$, are not. In the following we present micromagnetic simulations performed on Ni NTs of different lengths l to further analyze our data.

7.5. Micromagnetic simulations

In Fig. 7.4 (a) we show simulated hysteresis loops $M(H)$ with \mathbf{H} applied along the long axis of NTs with l between 250 nm and 2 μm . For $l = 2 \mu\text{m}$ the $M(H)$ loop is almost square, but the switching field is $\sim 8 \text{ mT}$. This value is much smaller than the regime of $H_{sw,e}$ observed experimentally. NTs with $250 \text{ nm} < l < 1 \mu\text{m}$ are consistent with $15 \text{ mT} < \mu_0 |H_{sw,e}| < 35 \text{ mT}$. For $l = 500 \text{ nm}$ the simulation provides a switching field $\mu_0 H_{sw} = 28 \text{ mT}$. At the same time,

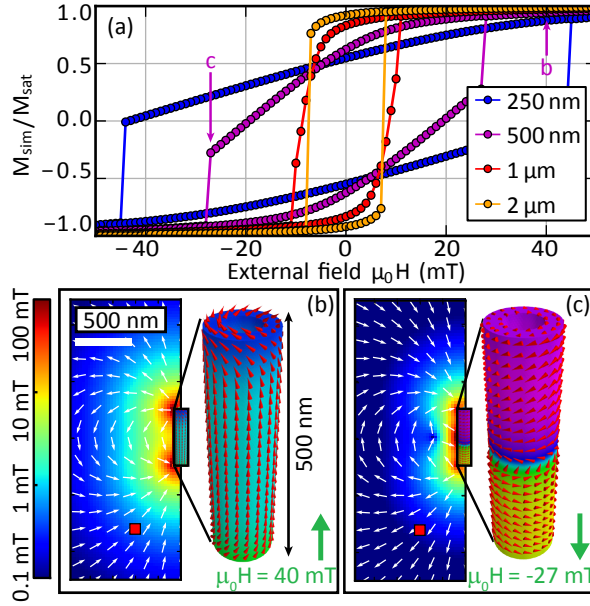


Figure 7.4. | (a) Simulated hysteresis loops $M(H)$ for NTs of four different l . H_{sw} increases with decreasing l . Magnetic configurations (right) and stray-field distribution (left) for $l = 500$ nm at (b) 40 mT and (c) -27 mT as indicated by the labels in (a). Cones (arrows) indicate the local direction of the magnetic moments (stray field). The stray fields H_{str} are color coded as depicted. The red squares indicate the position of the center of the nanoSQUID loop.

M is almost zero for $|H|$ just below $|H_{sw}|$. Such behavior is consistent with the overall shape of the measured $M(H)$ loop in Fig. 7.3 (c), where the largest jumps in M take place at about ± 30 mT. Comparing Fig. 7.4 (a) and Fig. 7.3 (c), we conclude that the superposition of a few segments with $250 \text{ nm} < l < 1 \text{ }\mu\text{m}$ could account for the measured $M(H)$. For such segments, Fig. 7.4 (b) and (c) (right panels) show characteristic spin configurations (cones) well above and near H_{sw} , respectively. We observe the gradual tilting of spins at both ends in (b) and two tubular-like vortex domains with opposite circulation direction in (c) [192]. Between the domains a Néel-type wall exists. For each l and $M(H)$, we simulate the relevant stray field at the position of the nanoSQUID (red squares in the left panels of Fig. 7.4 (b) and (c)) providing the predicted $\Phi_{NN}(H)$ (see Appendix A) The shapes of the simulated $\Phi_{NN}(H)$ are nearly proportional to and thus closely follow the shape of $M(H)$ shown in Fig. 7.4 (a). Thus the simulations allow us to explain the measured torque magnetometry data, although they are inconsistent with the nanoSQUID data.

7.6. Comparison of DCM and SQUID magnetometry data

The contrast between hysteresis traces obtained by the nanoSQUID and torque magnetometry shows that $\Phi(H)$ is not the projection of \mathbf{M} along the NT axis. This finding contradicts the assumption of Ref. [31]; we attribute this discrepancy to the fact that while cantilever magnetometry measures the entire volume magnetization, the nanoSQUID is most sensitive to the magnetization at the bottom end of the NT, as shown in calculations of the coupling factor $\phi_\mu = \Phi/\mu$ (flux Φ coupled to nanoSQUID by a point-like particle with magnetic moment μ) [186]. Still, we find a one-to-one correspondence between switching fields $H_{sw,e}$ detected by

either the nanoSQUID or cantilever magnetometry. This experimentally verified consistency substantiates the reversal field analysis performed in Ref. [31]. In Fig. 7.2 (a), we find no clear evidence for curling or gradual tilting at small H . The reversal process thus does not seem to start from the end closest to the nanoSQUID, but rather from a remote segment. This is an important difference compared to the ideal NTs considered thus far in the literature, in which both ends share the same fate in initiating magnetization reversal. The unintentional roughness of real NTs might be relevant here. In an experiment performed on a large ensemble of NTs, one would have not been able to judge whether a gradual decrease in $M(H)$ [26] originated from a very broad switching field distribution or from the gradual tilting of magnetic moments in the individual NTs. Our combination of nano-magnetometry techniques thus represents a powerful method for unraveling hidden aspects of nanoscale reversal processes. In order to optimize NTs for sensing and memory applications, such understanding is critical.

7.7. Conclusion

In summary, we have presented a technique for measuring magnetic hysteresis curves of nanometer-scale structures using a piezo-electrically positioned nanoSQUID and a cantilever operated as a torque magnetometer. This dual functionality provides two independent and complementary measurements: one of local stray magnetic flux and the other of volume magnetization. Using this method we gain microscopic insight into the reversal mechanism of an individual Ni NT, suggesting the formation of vortex-like tubular domains with Néel type walls.

8. Magnetization reversal nucleating at the end of a CoFeB nanotube detected with SQUID and torque magnetometry

R. Woelbing, A. Buchter, M. Wyss, O. F. Kieler, T. Weimann, J. Kohlmann, A. B. Zorin, D. Ruffer, F. Matteini, G. Tütüncüoğlu, F. Heimbach, A. Fontcuberta i Morral, D. Grundler, R. Kleiner, D. Koelle, M. Poggio

”Magnetization reversal nucleating at the end of a CoFeB nanotube detected with SQUID and torque magnetometry”,

in preparation

The magnetization reversal mechanism in an individual CoFeB nanotube (NT) is investigated using a hybrid magnetometer. It consists of a nanometer-scale SQUID (nanoSQUID) and a cantilever torque sensor. With the CoFeB NT at the tip of a Si cantilever we are able to measure both the NT’s volume magnetization by dynamic cantilever magnetometry (DCM) and position dependent stray flux using the nanoSQUID. We find proportionality between the NT’s volume magnetization measured by torque magnetometry and the generated stray flux which is probed with the nanoSQUID. With the nanoSQUID we detect the magnetization reversal to start at lower fields than with DCM. This indicates that reversal starts from the NT’s end.

8.1. Introduction

Research during the last decade on ferromagnetic NTs has found evidence for outstanding properties making them an interesting subject for fundamental studies and applications. Theoretical investigations suggest geometry dependent fast and controllable magnetization reversal and vortex-like magnetization states leading to vanishing stray flux [10, 12]. These properties make them ideal candidates for future memory devices [7]. To get from theoretical findings to applications, the properties of real nanoscale structures have to be thoroughly investigated and understood. Key to tackle this challenge is investigation on the single particle scale to avoid averaging and interaction effects present in ensemble measurements [15, 24]. Measurements on single particle level avoid these problems, but are challenging due to the inherently small magnetic moment. There have been successful demonstrations of anisotropic magnetoresistance measurements of Co and Ni nanowires [27] and Ni and CoFeB NTs [21, 22]. Also cantilever torque magnetometry has been demonstrated on Fe filled carbon nanotubes (CNT) [29], Co nanowires [28] and Ni NTs [30] whereas SQUIDs proved their capability on Ni nanowires [31] and Fe filled CNT [33]. By combining the latter devices in a hybrid magnetometer, in a previous work we were able to identify surface roughness to influence magnetization reversal of a Ni NT [178]. Having improved the sensitivity of our nanoSQUID read-out since then and mastered fabrication of smooth CoFeB NT we demonstrate in this letter proportionality between NT's volume magnetization and its stray flux.

8.2. Setup

The setup consists of a single CoFeB NT attached to the tip of an ultrasoft Si cantilever hanging in the pendulum geometry above a dc nanoSQUID as imaged in Fig. 8.1 [178, 186]. The cantilever consists of a 90 μm long and 4 μm wide shaft followed by a 12 μm wide paddle, both 0.1 μm thick. The tip of the cantilever is formed by a 18 μm long and 1 μm thick mass to suppress higher order mechanical modes [119]. Read-out of the cantilever displacement is achieved with a temperature controlled 1550 nm DFB laser integrated in a fibre-optical interferometer [171]. At $T = 4.2$ K far from the nanoSQUID we determine the cantilever's resonance frequency $f_0 = 3194.7$ Hz, its spring constant $k_0 = (195 \pm 40)$ $\mu\text{N}/\text{m}$ and quality factor $Q_0 = 25 \times 10^3$.

The dc nanoSQUID is formed by two 250 nm wide Nb strips sandwiching a 224 nm thick SiO_2 layer. Top and bottom layer are electrically connected by two fingers made of 200 nm thick Nb and 24 nm thick HfTi forming the two Nb/HfTi/Nb Josephson junctions (JJs) with individual area of 200×200 nm^2 and a lateral distance of 1.6 μm [117, 167]. Thus, the area of the SQUID loop is 1.6×0.22 μm^2 . The device is flux-biased by a modulation current I_{mod} flowing in the bottom electrode and at the optimum working point achieves a rms flux noise $S_{\Phi}^{1/2} = 190$ $\text{n}\Phi_0/\text{Hz}^{1/2}$ [117, 163]. Read-out is performed with a series SQUID array as a cryogenic amplifier, strongly improving effective sensitivity compared to previous experiments (compare [178, 186]). The nanoSQUID is placed on a stack of xyz piezo-electric motors to allow its three dimensional positioning relative to the cantilever. The whole setup is housed in a vacuum chamber (pressure $< 10^{-6}$ mbar) at the bottom of a temperature variable He^3 cryostat equipped with a superconducting magnet generating up to 6 T.

The 14.8 μm long NT with a diameter of ~ 200 nm consists of a non-magnetic GaAs nanowire serving as template. A (30 ± 2) nm thick film of CoFeB showing no magnetocrystalline

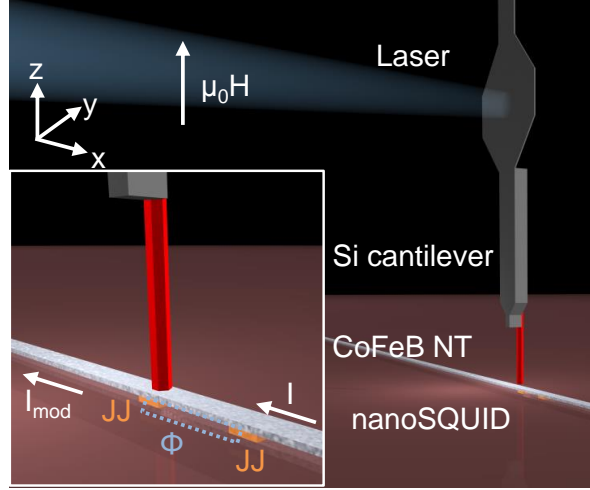


Figure 8.1. | Image (not to scale) of the cantilever with attached CoFeB NT hanging in pendulum geometry above the nanoSQUID. The inset shows more details of the nanoSQUID including paths for bias current I , modulation current I_{mod} as well as an indication of the SQUID loop.

anisotropy is applied in a sputtering process using a $\text{Co}_{20}\text{Fe}_{60}\text{B}_{20}$ target resulting in a magnetic volume $V = (3.18 \pm 0.60)10^{-19} \text{ m}^3$ of the investigated NT [21]. The NT is attached to the cantilever's tip using hydraulic micromanipulators placed under an optical microscope. The NT's end is cut flat using a focussed ion beam (FIB) to ensure ideal tubular geometry close to the nanoSQUID.

8.3. High and low field characterization with DCM

In a first step we analyze the CoFeB NT's high field characteristics, its saturation magnetization M_s and its effective anisotropy given by the demagnetization factor D_u . Therefore, the cantilever is retracted several tens of μm away from the nanoSQUID avoiding any possible interaction with the superconducting structures. Then the magnetic field is ramped in 20 mT increments from 0 to 2 T. The measured frequency shift Δf of the cantilever versus applied field $\mu_0 H$ is plotted in Fig. 8.2a). Employing an analytical model described in detail elsewhere [30, 93] in the limit of high applied fields, where magnetization is forced to align either parallel or anti-parallel to the applied field the DCM frequency shift is predicted as

$$\Delta f = \frac{f_0 \mu_0 V}{2k_0 l_e^2} \left(\frac{-D_u M_s^2 H}{H \mp D_u M_s} \right), \quad (8.1)$$

where μ_0 is the vacuum permeability, V is the CoFeB NT's volume and M_s its saturation magnetization, k_0 and f_0 are the cantilever's spring constant and resonance frequency and l_e is its effective length in the fundamental mode. The two solutions are valid for $H > D_u M_s$ and $H < -D_u M_s$ respectively, which for the NT's easy-axis anisotropy ($D_u < 0$) results in a region of bistability, allowing for magnetic hysteresis. Setting V , l_e , f_0 and k_0 to their previously measured values we obtain the saturation magnetization $\mu_0 M_s = (1.37 \pm 0.24) \text{ T}$ and demagnetization factor $D_u = 0.497 \pm 0.001$.

We now turn to the analysis of the NT's magnetization in low applied fields. With the cantilever still retracted from the surface, the applied field is swept in increments of 1 mT in

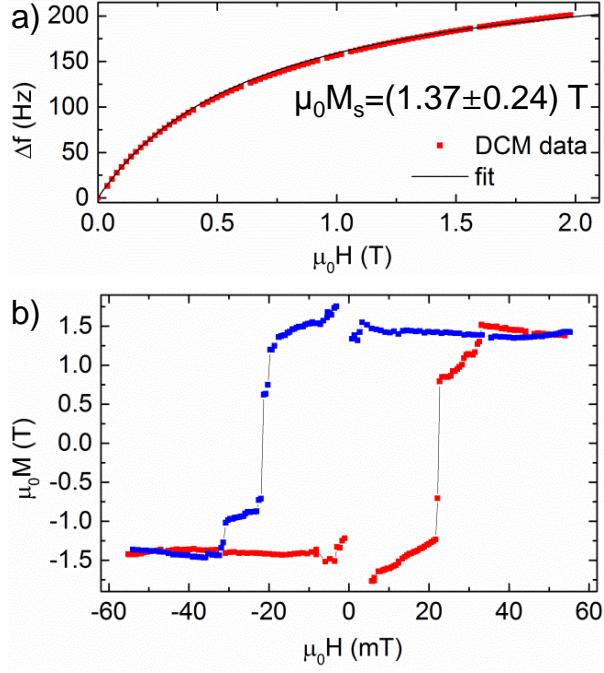


Figure 8.2. | a) Frequency shift of the cantilever during a sweep of the applied field from 0 – 2 T far from the nanoSQUID, fitted to Eq. 8.1. b) NT’s hysteresis loop with DCM data converted according to Eq. (8.2).

the range of ± 55 mT. The measured frequency shift Δf of the cantilever is again analysed using the above mentioned analytical model. In the limit of low magnetic fields ($H \ll D_u M_s$) the obtained equation for the frequency shift can be solved for the z-component of magnetization

$$M_z = \frac{2k_0 l_e^2}{f_0 \mu_0 V H} \Delta f. \quad (8.2)$$

With the aid of this model the measured frequency shift Δf is converted into the NT’s magnetization z-component M_z , providing the hysteresis loop of the NT’s volume magnetization plotted in Fig. 8.2b). The up- and down-sweep is marked with red and blue circles. The hysteresis is of generally square shape, reversing its magnetization not in a single step but via intermediate states. Note, the missing data points around zero field are due to the divergence for $H \approx 0$ in the conversion and have been removed.

Following the down sweep (blue circles) starting from 55 mT, the magnetization remains approximately constant until the applied field is reversed. The exact onset of the coherent magnetization reversal is unfortunately obscured due to the Δf to M conversion procedure. However, it can roughly be located around -10 mT. This coherent reduction of magnetization is then followed by multiple abrupt switching processes with intermediate states, starting at 20 mT. The behavior for the reverse field sweep is comparable.

8.4. SQUID magnetometry

After having described the CoFeB NT’s integrated volume magnetization in the limit of high and low applied fields, in the next step DCM low field data is compared to NT’s stray field detected with the nanoSQUID.

Therefore, at zero-field, the sample chamber is heated well above the critical temperature of Nb ($T_c \approx 9$ K) and subsequently cooled down to operation temperature $T = 4.2$ K to ensure that the nanoSQUID is free of Abrikosov vortices hindering the experiment.

We first approach the NT to the nanoSQUID, then we probe the spatial coupling map. Therefore, the NT, magnetized along \hat{z} in remanence, is scanned at a fixed height $z = 1$ μm in a 7×7 μm plane above the nanoSQUID. The resulting coupling map including the nanoSQUID loop's position marked in yellow is shown in the inset of Fig. 8.3a). The bipolar signal detected from the NT magnetized along \hat{z} fully corresponds to our previous findings [178]. Note, that coupling maps for magnetization along \hat{y} would look different and show a maximum right above the nanoSQUID rather than beside it [117, 156]. The NT is now positioned in a suitable position of high coupling, marked in red for the following hysteresis measurement. The field is initially ramped to 55 mT before the hysteresis loop is measured between ± 55 mT with increments of 1 mT. The overall detected flux level accounts to $130 m\Phi_0$ peak to peak. Following the blue data points, the detected flux is constant between 55 to 6 mT within the next 27 mT a steady decrease by 30 % is monitored, followed by several abrupt switching events to conclude the magnetization reversal. The sweep back shows qualitatively the same behavior, the switching however is more abrupt with less distinct intermediate states.

Comparing the hysteresis loops of the volume magnetization $M(H)$ measured with DCM and the stray flux $\Phi(H)$ detected by the nanoSQUID, very similar behaviour is apparent. Reproducing most important features like squareness of the loop and existence of intermediate magnetization reversal states, we conclude $\Phi(H)$ is approximately proportional to $M(H)$. This finding is in contrast to our previous results obtained on Ni NTs, where increased surface roughness was identified to influence magnetization reversal and ultimately led to significant deviations between $\Phi(H)$ and $M(H)$ [178].

Having verified the consistency of $\Phi(H)$ and $M(H)$ we now turn to further exploring the NT's magnetization reversal by varying its position relative to the nanoSQUID. To do so, the NT is positioned almost on top of the SQUID loop as marked in the inset of Fig. 8.3b), still at $z = 1$ μm . The applied field is swept between ± 55 mT in 1 mT increments. The resulting $\Phi(H)$ hysteresis loop is plotted in Fig. 8.3b) and will be compared to the hysteresis in Fig. 8.3a). The change of the NT's position leads to an increased peak-to-peak flux signal of $222 m\Phi_0$ which indicates an increased sensitivity of the nanoSQUID to the NT's stray field compared to the measurement shown in Fig. 8.3a). Together with an overall increase of the signal, also a stark change in the shape of the hysteresis loop is apparent. Following the blue data points Φ is constant between 55 – 20 mT, from 20 to –20 mT a steady decrease by ≈ 50 % is detected before abrupt switching concludes the magnetization reversal. Very similar behaviour is detected on the reverse field sweep. We notice that, compared to Figs.8.3a) and 8.2b), the onset of the field range showing coherent reversal now starts at lower fields, is more pronounced and the width of the range is increased by ~ 13 mT.

From earlier work, simulating the reversal process in ferromagnetic NT [183], reversal is expected to be moderated by vortices nucleating at the NT's ends. As the nanoSQUID is most sensitive to changes of the magnetization at the NT's end, our data can be interpreted as detection of the reversal nucleating at the NT's end close to the nanoSQUID.

The measured data supports the finding of reversal starting at the NT's end, it however, does not unambiguously support the predicted reversal being mediated by tubular vortex-like domain walls. The increased signal level for the NT being positioned closer to the nanoSQUID can be interpreted as magnetization along \hat{y} (as occurring in the vortex configuration) coupling flux into the signal. Also the detected intermediate switching states, coupling no flux in the

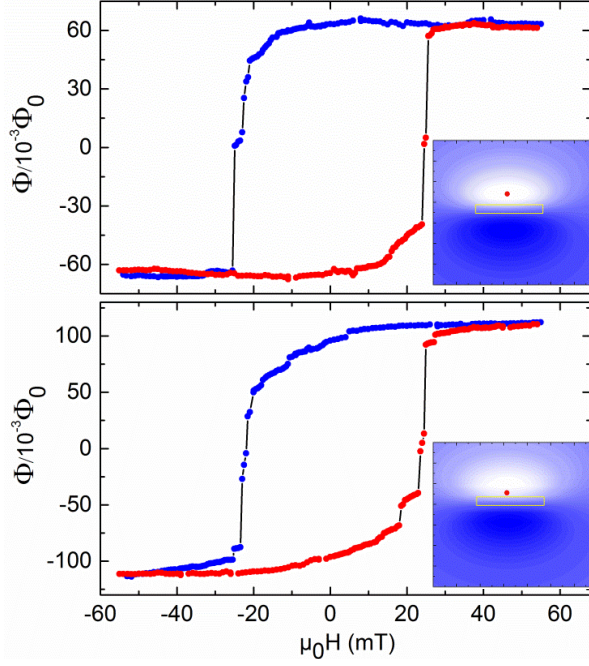


Figure 8.3. | nanoSQUID-detected hysteresis loop at height $z = 1 \mu\text{m}$ above the top electrode, with the NT placed at the position marked on the coupling map shown in the inset a) beside the SQUID loop and b) almost on top of the SQUID loop. The coupling map cover a $7 \times 7 \mu\text{m}^2$ area and signal level is $\Phi = \pm 100 \text{ m}\Phi_0$.

nanoSQUID, might be interpreted as signature of a global vortex state. It has to be emphasized however, that the last points are purely speculative and could also be explained e.g. by multi-domain states with alternating magnetization.

To verify the exact nature of the reversal process micromagnetic simulations are necessary. Such simulations provide a clearer picture of the magnetization dynamics, taking into account the specific geometry and material's parameters of the measured CoFeB NT. Furthermore, simulations would allow to simulate the stray field generated by the NT at the position of the SQUID loop allowing a more direct and reliable interpretation of the data measured.

8.5. Conclusion and outlook

In summary we have presented hysteresis measurements of a single CoFeB NT, conducted with a combined magnetometer consisting of a cantilever and a nanoSQUID, sensitive to the NT's volume magnetization and its stray field. The saturation magnetization of the NT is determined to be $\mu_0 M_s = (1.37 \pm 0.24) \text{ T}$ and its demagnetization factor $D_u = (0.497 \pm 0.001)$. Comparing the volume magnetization and the stray field we find strong evidence for the magnetization reversal to nucleate at the NT's end close to the nanoSQUID. The presence of vortex-like magnetization states can not unambiguously be confirmed. However, the presence of intermediate states generating no stray field and the position dependent nanoSQUID data of the stray field hint towards such a behavior. To clarify these speculative findings, micromagnetic simulations of a NT with the same geometry and material's parameters are necessary.

9. Magnetization reversal of an individual exchange biased permalloy nanotube

Adapted from:

A. Buchter, R. Woelbing, M. Wyss, O. F. Kieler, T. Weimann, J. Kohlmann, A. B. Zorin, D. Ruffer, F. Matteini, G. Tütüncüoğlu, F. Heimbach, A. Kleibert, A. Fontcuberta i Morral, D. Grundler, R. Kleiner, D. Koelle, M. Poggio

”Magnetization reversal of an individual exchange biased permalloy nanotube”,
accepted in Phys. Rev. B (arXiv:1512.00199)

We investigate the magnetization reversal mechanism in an individual permalloy (Py) nanotube (NT) using a hybrid magnetometer consisting of a nanometer-scale SQUID (nanoSQUID) and a cantilever torque sensor. The Py NT is affixed to the tip of a Si cantilever and positioned in order to optimally couple its stray flux into a Nb nanoSQUID. We are thus able to measure both the NT’s volume magnetization by dynamic cantilever magnetometry and its stray flux using the nanoSQUID. We observe a training effect and temperature dependence in the magnetic hysteresis, suggesting an exchange bias. We find a low blocking temperature $T_B = 18 \pm 2$ K, indicating the presence of a thin antiferromagnetic native oxide, as confirmed by X-ray absorption spectroscopy on similar samples. Furthermore, we measure changes in the shape of the magnetic hysteresis as a function of temperature and increased training. These observations show that the presence of a thin exchange-coupled native oxide significantly alters the magnetization reversal process in magnetic NTs at low temperatures, but has little effect at room temperature.

9.1. Introduction

Fabrication and characterization of magnetic nanostructures is motivated by a wide range of applications, including their use as media in dense magnetic memories [7], as magnetic sensors [182], or as probes in high resolution magnetic imaging [179–181]. The desire for higher density memories, more sensitive sensors, and higher resolution imaging has pushed magnet size deep into the nanometer-scale. At these length scales, the stability of magnetization configurations strongly depends on geometry, defects, and minute levels of contamination. This sensitivity to imperfection makes the experimental realization of idealized systems such as ferromagnetic rods and tubes particularly challenging. Furthermore, due to the small total magnetic moment of each nanomagnet, conventional magnetometry techniques do not have the necessary sensitivity to measure individual nanostructures. As a result, measurements of their magnetic properties are often carried out on large ensembles, whose constituent nanomagnets have a distribution of size, shape, and orientation and – depending on the density – may interact with each other [24, 184]. These complications conspire to make accurate characterization of the stable magnetization configurations and reversal processes difficult.

In order to obtain a clear understanding of the magnetic properties of ferromagnetic nanotubes (NTs), it is therefore advantageous to investigate individual specimens. Ferromagnetic NTs are particularly interesting nanomagnets because of their lack of a magnetic core. This geometry can make flux-closure magnetization configurations more favorable than single-domain states [193]. Flux-closure configurations are predicted to enable fast and reproducible magnetization reversal and they produce minimal stray magnetic fields, thereby reducing interactions between nearby nanomagnets. We therefore measure the magnetization and stray field hysteresis of an individual permalloy (Py) NT using a hybrid magnetometer. The magnetometer combines a sensitive mechanical sensor for dynamic cantilever magnetometry (DCM) and a nanometer-scale SQUID (nanoSQUID) for the measurement of stray magnetic fields. This measurement technique was first demonstrated on individual Ni NTs by Buchter et al. [178], who revealed the importance of morphological defects in altering the reversal process in real ferromagnetic NTs from the theoretical ideal.

Here, we study individual Py NTs. The fabrication process is based on evaporation instead of atomic layer deposition as used for Ni NTs [22] and provides polycrystalline Py NTs with smooth surface that are morphologically closer to an idealized tube. Despite the geometrical perfection of the Py NTs, the measured low-temperature hysteresis curves reveal, that a thin exchange-coupled native oxide changes the reversal process. Since the oxide is thin – likely less than 5 nm – these effects only appear at temperatures below 20 K. The role of the oxide is only apparent due to the sensitivity of the hybrid magnetometer to single NTs, since averaging effects would likely obscure the behavior in conventional measurements of NT ensembles. The strong effect of such a thin oxide layer on magnetic reversal, points to the importance of gaining further control of the fabrication of ferromagnetic NTs. At the same time, the results indicate that engineered oxide layers could be used to pin or otherwise control the magnetic configurations of magnetic NTs.

9.2. Setup

In order to fabricate the Py NTs, GaAs nanowires grown by molecular beam epitaxy are used as templates. These nanowires are 10 to 20 μm long and have hexagonal cross-sections with

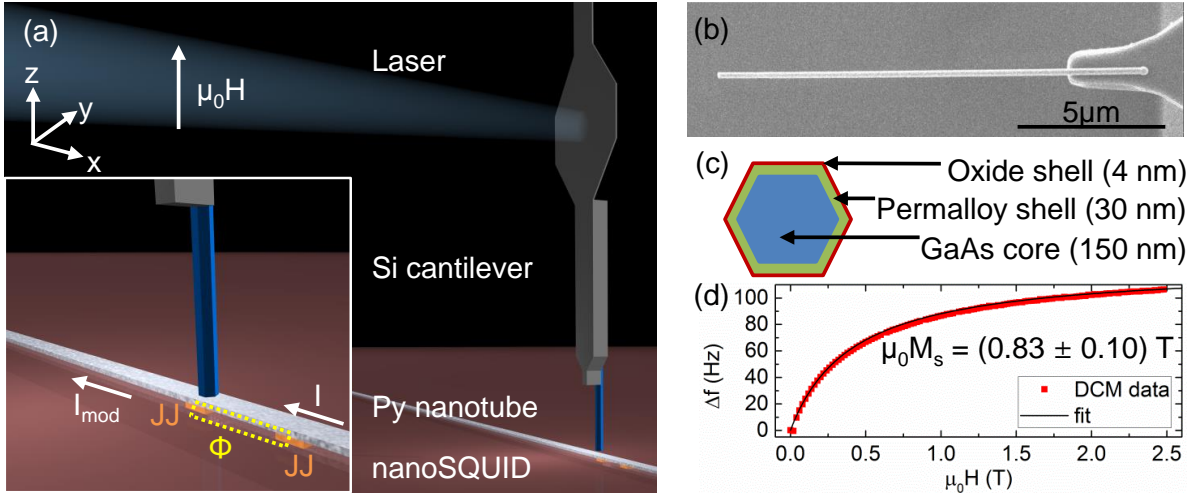


Figure 9.1. | a) Image of the hybrid magnetometer including a close-up inset showing the nanoSQUID. b) SEM of the investigated Py NT on cantilever. c) Schematic cross-section of a Py NT as inferred from the measurements. d) Measurement of $\Delta f(H)$ of a Py NT by DCM. The saturation magnetization $\mu_0 M_s = 0.83 \pm 0.10$ T is determined by fitting the data to Eq. 9.1.

a width $d = 150 \pm 20$ nm at their widest point. Tubes of magnetic material are formed by thermally evaporating a 30 nm polycrystalline Py shell onto the template nanowires. For this deposition, the low density GaAs nanowire wafer is mounted under 35° angle and continuously rotated in order to achieve a conformal coating. The films fabricated in this process are very smooth, show no discontinuities and the roughness is less than 5 nm. Individual Py NTs are then selected and transferred from the wafer to the end of a Si cantilever using high precision hydraulic micro-manipulators (Narishige MMO-202ND) mounted under an optical microscope. Each NT is attached parallel to the cantilever's long axis, such that it protrudes from its end by $\sim 12 \mu\text{m}$. The NT studied in this work is $14.8 \mu\text{m}$ long, and has a magnetic volume $V = (2.46 \pm 0.18) \cdot 10^{-19} \text{ m}^3$.

In our hybrid magnetometer, the single-crystal Si cantilever serves two purposes: 1) as the torque transducer in DCM measurements of the NT and 2) as a platform for positioning the NT such that stray magnetic fields from its tip couple to the nanoSQUID. It is $105 \mu\text{m}$ long, $4 \mu\text{m}$ wide and $0.1 \mu\text{m}$ thick and has a $1 \mu\text{m}$ thick and $18 \mu\text{m}$ long mass at its end to suppress higher order modes [119]. The NT-tipped cantilever hangs in the pendulum geometry above the nanoSQUID in a vacuum chamber at the bottom of a temperature variable He^3 cryostat. This system is capable of temperatures down to 0.3 K and magnetic fields up to 6 T along the long axis of the cantilever (\hat{z}). The read-out of the cantilever deflection is achieved through a laser interferometer. We use a temperature controlled 1550 nm fiber-coupled DFB laser diode and an interferometer cavity formed between the cleaved end of an optical fibre and the $12 \mu\text{m}$ wide paddle of the Si cantilever [171]. By feeding the measured displacement signal through a field-programmable gate array (National Instruments) and back to a piezoelectric actuator mechanically coupled to the cantilever, we self-oscillate the cantilever at its mechanical resonance frequency f_c . The oscillation amplitude is stabilized to $x_{rms} = 10$ nm, for which the deflection angle $\theta_{rms} \ll 1$, allowing for fast and accurate determination of f_c . At a temperature of 3.8 K and far from any surface the cantilever has an intrinsic resonance

frequency of $f_c = f_0 = 3980$ Hz and a quality factor $Q_0 = 41 \cdot 10^3$. The spring constant $k_0 = 185 \mu\text{N/m}$ is determined by thermal noise measurements at different temperatures.

In order to control the relative position of the NT and the nanoSQUID, the nanoSQUID is mounted on a three dimensional piezoelectric positioning stage (Attocube). We use a direct current nanoSQUID containing two superconductor-normal metal-superconductor Josephson junctions (JJs) in a microstrip geometry [163]. Two 250 nm wide and 200 nm thick Nb strips lie on top of each other and are separated by a 224 nm thick SiO_2 insulating layer. To form the $1.6 \times 0.224 \mu\text{m}^2$ SQUID loop, the Nb strips are connected by two Nb/HfTi/Nb JJs with $200 \times 200 \text{ nm}^2$ area and a 24 nm thick HfTi barrier. Using a cryogenic series SQUID array as a low noise amplifier in a magnetically and electrically shielded environment and Magnicon XXF-1 read-out electronics, the described nanoSQUID shows a rms flux noise $S_{\Phi}^{1/2} = 190 \text{ n}\Phi_0/\text{Hz}^{1/2}$.

9.3. DCM high field characterization

We first investigate the NT sample through high-field DCM as plotted in Fig. 9.1d). The field $\mu_0 H$ is swept from 0 T to 2.5 T in 20 mT increments, while the frequency shift of the cantilever $\Delta f(H) = f_c(H) - f_0$ is measured. The NT is composed of a Py shell that is known to be magnetically isotropic at room temperature. At small T , the polycrystalline morphology is expected to average out any magnetocrystalline anisotropy. Given the latter and given the large aspect ratio of the NT, its anisotropy energy is dominated by shape effect. Therefore, the data are fit to an analytical model describing a Stoner-Wohlfarth particle with shape anisotropy [30]. In this model, the NT is idealized as a uniformly magnetized magnet whose magnetization rotates in unison. For H applied along the easy axis of a sample with large shape anisotropy – as in this case – the magnetization is forced to be either parallel or anti-parallel to the applied field. As a result, this model is an excellent approximation for most of the field range, except in the regions of magnetic reversal. The model predicts a DCM frequency shift given by,

$$\Delta f = \frac{f_0 \mu_0 V}{2k_0 l_e^2} \left(\frac{-D_u M_s^2 H}{H \mp D_u M_s} \right), \quad (9.1)$$

where μ_0 is the permeability of free space, V is the volume of the Py NT, l_e is the effective length of the cantilever for its fundamental mode, M_s is the saturation magnetization, and D_u is the effective uniaxial demagnetization factor along \hat{z} [30, 93]. The two solutions are valid for $H > D_u M_s$ and $H < -D_u M_s$ respectively, which for the NT's easy-axis anisotropy ($D_u < 0$) results in a region of bistability, allowing for magnetic hysteresis. By fitting the measurements shown in Fig.9.1d) with this expression, we extract $\mu_0 M_s = (0.83 \pm 0.10)$ T and $D_u = -0.496 \pm 0.001$ as fit parameters. Input parameters are f_0 , k_0 , l_e , and V , which are all set to their measured values. The saturation magnetization measured for the Py NT is smaller than the literature value $\mu_0 M_{Py} = 1$ T for bulk Py [129]. This discrepancy may be the result of an overestimation of the NT volume due to the oxide layer present on the surface or due to other imperfections in the growth of the film. The measured demagnetization factor, however, is in excellent agreement with what can be calculated by approximating the NT as a hollow cylinder, ignoring its hexagonal cross-section. The main contribution to the error in the extracted values stems from the NT volume, which is difficult to determine precisely. We calculate V using the NT dimensions extracted from scanning electron micrographs (SEMs) of the Py shell thickness. A further source of error is the determination of the cantilever's spring constant.

9.4. Training effect

We now turn to the low-field behavior of the sample and the investigation of exchange bias. As key feature of exchange bias systems, we start by exploring the training effect of our sample. For initialization, the sample chamber is heated above 110 K. The subsequent cool-down to 3.4 K is done with an applied magnetic field of +200 mT, in order to create a defined state of magnetization in the NT. Exploiting the duality of our hybrid magnetometer, we measure both the stray magnetic flux generated by the NT with the nanoSQUID and the integrated magnetization by DCM. For the nanoSQUID measurements, the NT-tipped cantilever is positioned for optimal coupling at height $z = 1.1 \mu\text{m}$ above the nanoSQUID's top electrode [178, 186]. Despite this proximity of the nanoSQUID to the NT, the magnetic fields produced by the bias and modulation currents running through the nanoSQUID and its superconducting leads are much less than 1 mT at the position of the NT tip and do not significantly influence its magnetization state. Measurements of DCM, on the other hand, are carried out with the NT several tens of μm away from the nanoSQUID in \hat{z} . This large spacing avoids spurious magnetic torque generated by the magnetic field gradients of the nanoSQUID, which otherwise complicate conversion of $\Delta f(H)$ measured by DCM into magnetization $M(H)$.

In both cases, the magnetic field is swept first from 0 mT to +55 mT and subsequently between ± 55 mT until ten full hysteresis loops are completed. Fig. 9.2a) shows several iterations of magnetic hysteresis of the stray flux emanating from the NT measured by the nanoSQUID. In order to isolate the magnetic flux emerging from the Py NT from the spurious flux due to the external field threading through the slightly misaligned nanoSQUID, we record a reference sweep with the NT retracted tens of μm from the substrate. These reference data, which excludes effects due to the NT, are then used both to subtract spurious flux and as a calibration of the magnetic field-axis [178]. The blue triangles show the first sweep from 55 mT to -55 mT. The flux from the NT starts at $30 \text{ m}\Phi_0$ and slightly increases to $38 \text{ m}\Phi_0$ at -25 mT. This measurement artefact is the result of a slight temperature difference between the $n = 1$ loop and the reference sweep. Thermal drift developing in the timespan of approximately 10 hours between the two measurements alters the nanoSQUID's response. Magnetization reversal takes place in a field range from -31.1 mT to -36.9 mT with a coercive field of $\mu_0 H_{c-} = -36.5$ mT. The reversal sets in by a steady decrease in flux of $6.9 \text{ m}\Phi_0$ followed by a large, abrupt jump of $59.6 \text{ m}\Phi_0$. Following the subsequent up-sweep (red triangles), the temperature-induced slope can again be identified. In this case, reversal takes place over a wider field range than in the down-sweep, from -12.0 mT to 11.2 mT with a coercive field $\mu_0 H_{c+} = 9.4$ mT. We first observe a steady decrease of $9.0 \text{ m}\Phi_0$ of flux followed by four smaller jumps (in the range of $6 \text{ m}\Phi_0$), ending with a larger jump of $33 \text{ m}\Phi_0$. The total width of the loop is identified as the coercivity $\mu_0 H_c = \mu_0(H_{c+} - H_{c-})/2 = 23$ mT. We attribute the strong asymmetry of the hysteresis along the field axis to the exchange bias effect as will be detailed below. The corresponding parameter, the exchange bias field, is defined as $\mu_0 H_{EB} = \mu_0(H_{c+} + H_{c-})/2 = -13.5$ mT.

Subsequent sweeps show similar behavior, although with a progressive decrease in $|\mu_0 H_{c-}|$, as seen in the representative sweeps of Fig. 9.2a). Following the blue dots of the $n = 10$ sweep, we observe a smaller thermal drift effect than in the $n = 1$ -loop due to the proximity in time between the $n = 10$ -loop and the reference sweep taken at the end of the series. On the down-sweep, from 0 mT to -17.8 mT, the flux coupled into the nanoSQUID steadily decreases by $12.5 \text{ m}\Phi_0$, followed by two abrupt switching events until the reversal process completes at -20.0 mT. The reversal process on the up-sweep starts at -14.2 mT with a continuous reduction of stray field of $14.7 \text{ m}\Phi_0$ over a range of 9.0 mT. This continuous reversal is then followed by

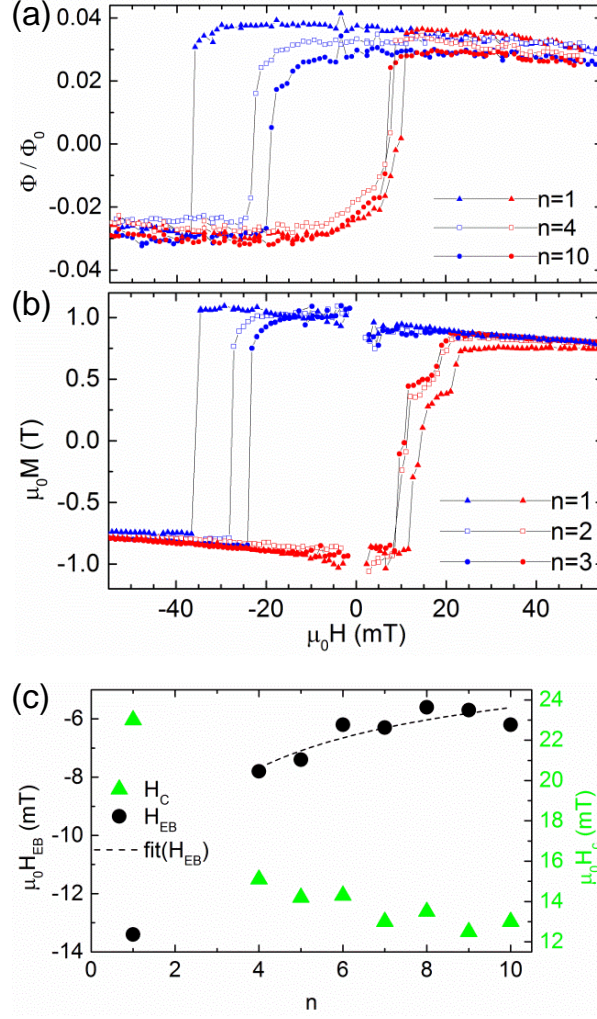


Figure 9.2. | Training effect: a) SQUID and b) DCM hysteresis loops for different loop number n . Red and blue curves indicate up- and down-sweep respectively. c) Evolution of exchange field and coercivity with increasing loop number n extracted from SQUID dataset. Dashed line fits the the data according to Eq. (9.2).

abrupt switching events until the process completes at 10 mT. The most striking deviations from the first loop are the reduced width of the hysteresis loop – now $\mu_0 H_c = 13.0$ mT – and the reduction of the exchange bias field $\mu_0 H_{EB} = -6.2$ mT. These findings are summarized in Fig. 9.2c), where $\mu_0 H_{EB}$ and $\mu_0 H_c$ for $n = 1 - 10$ are plotted. $|\mu_0 H_{EB}|$ decreases by ~ 7.2 mT until $n = 6$ after which point it stabilizes at -6 ± 0.5 mT. $\mu_0 H_c$ reduces by ~ 10 mT within the first seven loops until a saturation at 13 ± 0.5 mT. Past studies showed that the evolution of $\mu_0 H_{EB}$ can be described by the following formula especially in the case of a polycrystalline antiferromagnet [45, 54, 194]:

$$\mu_0 H_{EB}^n - \mu_0 H_{EB}^\infty = \frac{\kappa}{\sqrt{n}}, \quad (9.2)$$

where κ is a system dependent parameter and $\mu_0 H_{EB}^n$ and $\mu_0 H_{EB}^\infty$ are the exchange bias fields after n loops and in the limit of infinite number of loops respectively. The fit for $3 < n < 11$ is shown as dashed line in Fig. 9.2c). The data are reasonably described by this power-

law with deviations likely due to the inhomogeneity (in composition and thickness) of the naturally oxidized antiferromagnetic layer. As fit parameters we obtain $\kappa = -11.3$ mT and $\mu_0 H_{EB}^\infty = -2.0$ mT, whose magnitudes are of the same order as seen in literature [195]. Note also that as a function of training (increasing n), the hysteresis loop becomes more symmetric, losing the difference in the shape of the magnetization reversal for up- and down-sweeps. In particular, the abrupt reversal seen on the initial down-sweep is in stark contrast with the rounded transitions of later sweeps.

DCM data taken further away from the nanoSQUID, under otherwise identical conditions are shown in Fig. 9.2b). The magnetization hysteresis can be extracted from measurements of $\Delta f(H)$ at low applied magnetic fields, by taking the limit of (8.2) for $H \ll D_u M_s$ and solving for M_z : $M_z = \frac{2k_0 l_e^2}{f_0 \mu_0 V H} \Delta f$. Such data reflect the integrated magnetization of the entire NT, rather than the magnetization of the NT end closest to the substrate, as do the nanoSQUID measurements. The behavior of H_{EB} and H_c reproduces what we observe with the nanoSQUID. Nevertheless, differences are observable in the appearance of the magnetization reversals. For the $n = 1$ down-sweep, the single step magnetization reversal measured by DCM resembles that measured by the nanoSQUID. The reversal on the up-sweep shows a two-stage behavior, including an intermediate plateau, different than the continuous reversal followed by an abrupt switching seen in the corresponding nanoSQUID data. For $n > 1$, the down-sweep reversal gradually develops an initial stage of coherent reversal before discontinuous switching. Most strikingly, the coherent reversal seen in the nanoSQUID measurements, precedes the beginnings of any reversal observed by DCM. The discontinuous steps seen in the nanoSQUID sweeps coincide with the first discontinuous steps observed in DCM. The plateau and second discontinuous reversal measured in DCM corresponds to a portion of the nanoSQUID hysteresis that has already reached saturation.

These findings lead us to two conclusions. First, the differences observed in the hysteresis measured by the nanoSQUID and by DCM indicate that magnetization reversal likely nucleates at the ends of the NT and subsequently propagates throughout its length, as predicted by theory [183]. In this picture, vortex configurations form at the NT ends, begin tilting in the direction of the applied field, and subsequently cause magnetization reversal by propagating throughout the length of the tube and discontinuously switching to a uniform configuration aligned along the applied field. This kind of reversal is consistent with nanoSQUID measurements that show a smooth reversible reduction in stray field, which precede any deviation of M_z from saturation registered by DCM. The subsequent irreversible jump in the hysteresis is then registered both in the nanoSQUID and DCM measurements, thus apparently occurring throughout the NT and not only at the ends. The final stages of reversal seen in DCM, i.e. the plateau and second discontinuous step, appear to occur far from the NT end, since at this stage the nanoSQUID already shows a saturated signal. In short, the measurements appear consistent with the theoretical picture of reversal nucleation at the NT ends considering that the nanoSQUID is sensitive to magnetization located at the NT end and DCM is sensitive to the total magnetization integrated throughout the NT. Unlike the Ni NTs measured by Buchter et al. [178], whose reversal did not nucleate at the ends most likely due to imperfections in their structure, these Py NTs appear to behave like the idealized magnetic NTs considered in theoretical calculations.

Second, the exchange bias effect influences the nature of the reversal process of the NT, as manifested in the changing shape of the hysteresis as a function of training. In particular, for small n , the down-sweep magnetization reversal occurs almost exclusively through a single

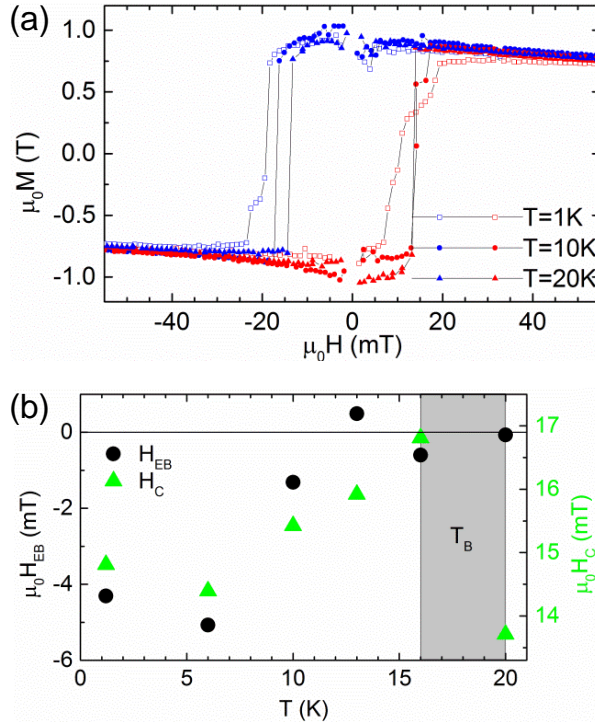


Figure 9.3. | Temperature dependence: a) DCM hysteresis loops for different temperatures in a trained out state ($n > 10$). b) Evolution of exchange field and coercivity with temperature. Gray area indicates range of T_B .

irreversible jump, while the up-sweep reversal and both reversals for large n contain both reversible rotation of magnetization and irreversible switching. The antiferromagnetic layer, in its initial configuration, appears therefore to pin the magnetization of the NT on the down-sweep, favoring reversal by abrupt domain nucleation and propagation. The exchange-coupled layer may thus suppress nucleation and initial coherent reversal through vortex configurations at the NT's ends.

9.5. Temperature dependence

We next investigate the temperature dependence of the exchange bias effect in the Py NT. Hysteresis loops are measured by DCM in a temperature range between 1 K and 20 K. Concurrent measurements with the nanoSQUID are not possible since the device's performance is strongly temperature dependent and above the critical temperature of Nb ($T_C \approx 9$ K), operation of the nanoSQUID is impossible. In order to ensure that our measurements are not obscured by training effects, we measure the temperature dependence after the extensive training of the NT, such that H_{EB} and H_C are constant with increasing n . In Fig. 9.3a), we plot three representative data sets at $T = 1, 10, 20$ K for convenient comparison. For each temperature, a hysteresis loop is measured for a field interval of ± 70 mT. Following the blue open squares – representing $T = 1$ K – between $70 - 5$ mT, magnetization remains constant around $\mu_0 M = 0.85$ T. At ≈ -5 mT the magnetization reversal process sets in by a continuous decrease of magnetization by 0.19 T followed by an abrupt irreversible reversal step. Then

over a range of 3 mT a plateau forms which is followed by a smaller jump in magnetization to complete the magnetization reversal. This second stage of reversal vanishes at higher temperatures, resulting in a reversal which occurs almost exclusively through a single irreversible jump for both down- and up-sweeps. Proenca et al. observe a similar two-stage reversal in an ensemble of Co NTs [195], with the second harder process also vanishing at high temperature. They thus connect this second stage of reversal to the exchange bias coupling. In contrast to our observations on a single Py NT, the coherent rotation measured in the Co/CoO arrays was extended over a much wider field range. Averaging over a distribution of different NTs in the array provides a possible explanation for this difference. In particular, NTs in the array appear in a distribution of shapes and sizes. In addition, NTs in both studies are oxidized naturally in an uncontrolled manner, allowing for a distribution of oxide thicknesses within an array. Since exchange bias crucially depends on film characteristics, including graininess and thickness, the hysteresis loops of the NT arrays are likely broadened by the distribution of different NTs in the array. For a detailed understanding, measurements of single NTs are therefore critical.

At $T = 20$ K (filled triangles) the hysteresis loop measured in the Py NT shows perfectly symmetric behavior. This symmetry, combined with the observed reduction of H_c and vanishing H_{EB} , indicates that the NT has reached the Py/oxide system's blocking temperature T_B . $\mu_0 H_c$ and $\mu_0 H_{EB}$ are plotted over the whole temperature range in Fig. 9.3b) allowing for the determination of $T_B \approx 18$ K. After $|H_{EB}|$ decreases with rising temperature we find $\mu_0 H_{EB} = 0 \pm 0.5$ mT above 12 K, indicating a blocking temperature T_B in this regime. A more precise determination is possible, taking $\mu_0 H_c$ into account. With increasing temperature the coercivity shows a steady increase from 14.5 mT to 17 mT until 16 K. At 20 K, the next investigated temperature, $\mu_0 H_c$ drops below 14 mT. This overall behavior is in line with previous studies [196] and allows us to determine a blocking temperature $T_B = 18 \pm 2$ K.

This very low blocking temperature deviates drastically from the bulk values of the Néel temperatures T_N of all the possible native oxides of Py, which are all well above 20 K. This deviation suggests that the oxide layer is very thin – in the range of 3 – 5 nm – and has a grainy and non-homogeneous structure [44, 45, 197]. Indeed, similar blocking temperatures around $T \approx 30$ K have been previously found for naturally oxidized Py thin films [198]. The decreasing extent of the continuous reversal region with increasing temperature could be the result of the inhomogeneity and graininess of the oxide shell. Assuming grains of different dimensions, the anti-ferromagnetic order could be gradually lost in different sections of the shell with increasing temperature, thus leading to a gradual temperature-dependent change in the reversal behavior. Note that the temperature dependence of the reversal process provides further evidence that the exchange bias has a direct influence on the nature of the magnetization reversal in the Py NT.

9.6. X-ray absorption spectroscopy of permalloy oxides

Given the measured exchange coupling, we investigate the nature of the native oxide present on the Py NTs using spatially resolved X-ray absorption spectroscopy (XAS) by means of X-ray photo-emission electron microscopy (PEEM). The experiments are performed using the PEEM instrument at the surface/interface:microscopy beamline of the Swiss Light Source at Paul Scherrer Institute [199]. NTs from the same growth wafer as the one used in the magnetometry experiment are investigated. For the PEEM study the NTs are transferred to a Si substrate with the aid of the aforementioned micromanipulators and transferred into the

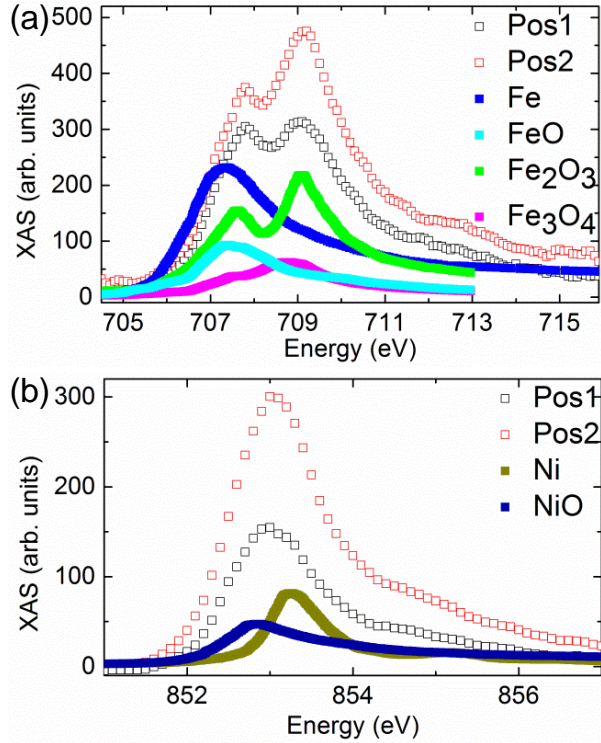


Figure 9.4. | a) Measured XAS of Fe L_3 edge and reference data for Fe and some of its oxides taken from reference [202]. b) Measured XAS of Ni L_3 edge and reference data for Ni and its oxide NiO taken from reference [202].

microscope. X-ray PEEM provides a spatial map of the local X-ray absorption cross section. By recording such maps as a function of the photon energy it is possible to record local X-ray absorption spectra. Details are described, e.g., in Refs. [200, 201]. The spatial resolution of the instrument is about 50 – 100 nm, and thus, enables us to perform XAS at various positions along the NT. We focus on XAS in the vicinity of the L_3 edges of Fe and Ni to study possible oxidation of the Py at different positions along the NT. Two measurement positions along a NT are chosen (at Pos 1: the NT’s broken end and another at Pos 2: close to the tip). One additional section on the substrate is chosen to allow for background subtraction. The spectra are recorded using circularly polarized X-rays. σ^+ polarized light is used first, then after correcting for mechanical drift, the polarization is changed to σ^- [203]. This procedure is repeated successively for each position on the NT. Isotropic spectra are obtained by averaging data according to $(\sigma^+ + \sigma^-)/2$. Two representative data curves measured at Pos 1 and at Pos 2 are plotted in Fig. 9.4a). The spectra resemble typical spectra of oxidized Fe and thus suggest the presence of a Py oxide layer on the Py NT. The spectra reveal Fe in different oxidation states in the Py oxide shell in addition to metallic Fe in the Py core, similar to what is observed in oxidized Fe surfaces, cf. Ref. [201]. For comparison, reference data of pure Fe, FeO, Fe₂O₃ and Fe₃O₄ taken from Regan et al. [202] are also plotted in Fig. 9.4a). The oxidation state of the present NT as seen at the Fe L_3 edge is compatible with previous reports on comparable Py systems, which identify FeO or α -Fe₂O₃ in the native oxide of Py [204, 205]. However, comparing the spectra measured at Pos 1 and 2 further shows that the oxide layer is not homogeneous in composition as indicated by the different ratio of the peaks at 707.8 and

709.2 eV and by the varying signal amplitude, which we assign to the differences in mechanical treatment when picking up the NT. In order to resolve the presence of NiO, we also measure spectra at the Ni L_3 edge between 850 – 858 eV. In Fig.9.4b) two representative curves are plotted for Pos 1 and 2 along with reference data for Ni and NiO from Regan et al. [202]. The Py NT's data are compatible with a superposition of spectra of NiO and metallic Ni, which suggests the presence of a layer of NiO, in agreement with previous studies [204, 205]. The latter conclude a layered composition of oxidized Py in the following sequence: Py/ $(\alpha$ -Fe₂O₃ or FeO)/NiO [205]. All three oxides are antiferromagnetically ordered below a certain ordering temperature (FeO: 198 K, α -Fe₂O₃: 95 K, NiO: 525 K) in the bulk [39]. The overall thickness of the oxide layer is estimated to be in the range of 2 – 5 nm. This estimate is based on previous studies in literature [204, 205] and consistent with the fact that we detect a XAS signature from the metallic Py in our sample with the typical probing depth of X-PEEM being about 5 nm. In such thin layers magnetic order temperatures are usually strongly reduced when compared to the bulk, and thus, might explain, why exchange bias in the present Py NTs is only observed at temperatures below 20 K.

9.7. Conclusion

In conclusion, in the absence of an exchange bias coupling with an unintentional antiferromagnetic oxide shell, we find strong evidence that the Py NT reverses its magnetization through the nucleation of a vortex configuration at its end followed by an irreversible switching process, as predicted by theory. However, below $T_B \approx 18$ K and before field training, we observe that the few-nanometer-thick native oxide on the NT alters the process of magnetization reversal. In particular, the non-equilibrium antiferromagnetic configuration of the oxide appears to pin the magnetization of the NT and suppresses the nucleation of the magnetic vortices at the NT ends for one of the sweep directions. Therefore, in order to control magnetization reversal in Py NTs, one must control either the nature of the oxide capping layer or work well above the determined blocking temperature $T_B = 18$ K, where exchange bias is not effective. These insights come as a direct result of our hybrid magnetometer's ability to measure both the behavior of the magnetic moments at the end of the NT and the magnetization integrated throughout its volume. Applying this technique for the investigation of reversal processes in other types of nanomagnets appears to be a promising path for future experiments.

10. Conclusions & Outlook

For the experiments presented in this thesis, a hybrid magnetometer sensitive enough to measure a single nanoscale magnetic particle has been developed. The setup allows for two simultaneous and complementary measurements on individual nanoscale magnets. With DCM the NT's magnetization integrated over its whole volume is determined. The nanoSQUID conversely is sensitive to the stray field emerging from the particle's lower end close to the nanoSQUID. This combination allows for extensive insight in the magnetic behaviour of individual magnetic NT.

DCM is a highly sensitive technique to measure the magnetization and anisotropy of small magnetic particles. The technique relies on the torque arising between an applied magnetic field and the magnetic moment of the particle under investigation, attached to the cantilever's tip. The torque leads to a virtual change of the cantilever's spring constant, effectively stiffening or softening the cantilever, depending on the applied field and the magnetization. This change of the spring constant then results in a measurable shift of the cantilever's resonant frequency that can be analyzed.

SQUIDs in general are the devices with highest sensitivity to magnetic flux. nanoSQUIDs in particular are additionally optimized to the detection of small magnetic particles by matching their loop size to the size of the detected particles. Magnetic field lines emerging from a particle's magnetization, that enclose the SQUID loop, lead to a voltage change across the device. The nanoSQUID is most sensitive to areas of the investigated elongated particle that are closest to it.

Among nanoscale magnetic particles, NTs are a particularly interesting example. Due to their geometry they support magnetic configurations not present in bulk or other nanoparticle geometries. They avoid point singularities of magnetization that occur in solid cylinders and thus their magnetization is proposed to reverse fast and reproducibly. Furthermore, theoretical analysis predicts a global vortex state. In this flux closure state, the NT's stray field is minimized that would allow for densely packing them without magnetic interference with neighbouring NTs.

The high aspect ratio NTs investigated in this thesis are all grown on a GaAs nanowire serving as template for structural support. Magnetic films are deposited onto the nanowires to obtain magnetically hollow tubes. In the course of this thesis Ni, CoFeB and Py magnetic films were investigated. The magnetic films are all isotropic and thus exhibit only shape anisotropy.

The NTs are attached to the tip of the cantilever with the aid of hydraulic micromanipulators under an optical microscope in ambient conditions. A single, as-grown NT is picked up from the wafer and then glued with the NT's easy-axis along the cantilever's long axis. All experiments are then performed in UHV at the bottom of a temperature variable He³ cryostat equipped with a superconducting magnet.

We use piezo-electric scanners that allow for free positioning of the nanoSQUID located below the cantilever hanging in pendulum-geometry to precisely map out the nanoSQUID's coupling characteristics in a $6 \times 7 \times 0.7 \mu\text{m}^3$ half space above the nanoSQUID. We then take advantage of this information to optimally position the NT relative to the nanoSQUID in order

to maximize the signal-to-noise ratio and consequently the sensitivity. Also the detection of an Abrikosov vortex trapped in the nanoSQUID structure by scanning probe microscopy is demonstrated. This information is of great importance to verify that detected signals solely originate from the NT and thus rule out spurious magnetic signals coupling to the nanoSQUID.

The torque magnetometry data is evaluated using an analytical model for ellipsoidal magnetic particles on the basis of the Stoner-Wohlfarth model. The magnetization is assumed to be constant throughout the magnet and magnetic moments to reverse in unison. Based on these assumptions the energy of the magnet-on-cantilever system can be minimized to obtain an expression for the cantilever frequency shift, which ultimately depends on the magnetic energy's curvature. With this model, in the limit of high applied fields, the saturation magnetization of the three investigated NT samples can be extracted to $\mu_0 M_s^{Ni} = (0.38 \pm 0.25)$ T, $\mu_0 M_s^{CoFeB} = (1.37 \pm 0.24)$ T and $\mu_0 M_s^{Py} = (0.83 \pm 0.10)$ T. In the limit of low applied fields, the frequency shift can be converted to the magnet-on-cantilever's magnetization. This allows to obtain $M(H)$ hysteresis data of the volume magnetization. $M(H)$ can then directly be compared to the stray flux $\Phi(H)$ measured by the nanoSQUID.

Exploiting the setup's duality to obtain volume magnetization $M(H)$ and stray flux $\Phi(H)$ and comparing this to micromagnetic simulations provides a powerful toolbox for analysis of magnetic properties. In the experiments on Ni NT we come to the conclusion that the film morphology and especially the distinct surface roughness has a significant influence on magnetization reversal. Comparing our data with micromagnetic simulations suggests the formation of vortex-like tubular domains in different segments of the NT instead of domains nucleating solely at the NT's ends.

On the other hand, comparing $M(H)$, $\Phi(H)$ in the case of the CoFeB NT, leads to the conclusion that the smooth CoFeB NT reverses by domain nucleation at the NT's end as theory predicts. This finding is supported by spatially dependent measurements which hint towards vortex domain nucleation at the NT's end and extending along the NT. This speculation however, needs further support by micromagnetic simulations.

Taking advantage of the temperature control in the cryostat, the exchange bias of a naturally oxidized Py NT is investigated. We explore the training effect and the temperature dependence of the NT's magnetization. We find a blocking temperature $T_B = 18 \pm 2$ K suggesting the presence of a thin oxide layer with thickness < 5 nm. The composition of the Py's oxide layer is analyzed with XAS and we find evidence for the possible presence of NiO, FeO, α -Fe₂O₃ and Fe₃O₄. Additionally, comparison of $M(H)$ and $\Phi(H)$ provides insight in EB influencing the NT magnetization reversal. However, at elevated temperatures, where EB is suppressed, reversal as expected from theoretical predictions can be verified with our hybrid magnetometer.

Results presented in this thesis have solely been obtained by experiments on magnetic NT. However, the setup in general is able to apply to a wide range of materials and geometries and is not restricted to such kind of magnetic NTs. Further interesting samples to investigate are for example rolled-up NTs [150], magnetic molecules [138], small particles in the superparamagnetic limit [206] or more complex multilayer cylindrical structures [207, 208].

The presented setup already provides deep insight in the reversal process of magnetic NTs on the single particle level. The system however has its limitations to unambiguously determine microscopic magnetization states. Employing scanning probe techniques can be a way to obtain information on magnetization with much higher spatial resolution. MFM has already proven its capability to resolve domains and domain walls in thin film samples by mapping the gradients of stray fields emerging from magnetic structures at the micromagnetic level.

Another promising technique involves diamond NV centres, with a high magnetic field sensitivity and spatial resolution on the subnanometer scale. Its advantage over MFM is the minimal invasiveness, because of the optical NV read-out, while the MFM's tip produces stray fields that might alter sensitive magnetic configurations in the sample under investigation.

A third and very promising scanning probe experiment is the SQUID-on-tip. These SQUIDs are very sensitive and small, thus should be able to detect small changes of magnetization down to single electron spins flipping with high spatial resolution and are furthermore minimally invasive to not perturb the sample's magnetic configuration.

Moving away from scanning probe methods towards synchrotron based techniques, XMCD analysis integrated in a X-PEEM is a promising method to resolve domain structures of magnetic samples on the nanoscale.

Apart from moving to other methods, the setup presented in this thesis also has room for improvement to widen the field of potential studies. The spatially resolved information obtainable with the nanoSQUID is limited due to the geometry of the magnet on cantilever in the pendulum geometry. Attaching the NT perpendicularly to the tip of the cantilever allows to scan the NT along its full length parallel to the SQUID loop. In this way it should be possible to obtain information on regions of the NT on the same length scale as the SQUID's loop width which currently is $1.6 \mu\text{m}$. Main challenge is the fact that higher magnetic fields will be necessary to access interesting magnetic configurations due to the increased anisotropy.

With the Nb nanoSQUIDs used in this thesis, not only the field range at which the device can be operated is limited, but also the temperature range. To overcome these limitations to a certain degree, the use of high- T_c YBCO nanoSQUIDs might provide a powerful extension of the possibilities of the presented setup. Having access to a wider temperature and field range makes the setup a valid candidate for the investigation of phase diagrams of more complex material samples like e.g. Skyrmions, Heusler compounds or further exchange bias systems [44, 209–212]. Due to the processing of the YBCO nanoSQUIDs, the SQUID loop is in the plane of the substrate. To avoid coupling a field in the loop, the SQUID has to be mounted with a 90° tilt compared to the present Nb devices. This perpendicular setup has already been demonstrated for MRFM experiments [213] and should pose no fundamental difficulties. The read-out between YBCO and Nb SQUIDs is compatible and would not demand for big changes.

The newly developed setup presented in this thesis has proven its ability to characterize various kinds of single magnetic NTs. The extension of its capabilities to access a wider parameter range is certainly possible. Having demonstrated the setup's ability not only on pure ferromagnetic samples but also on the more complicated phenomenon of exchange bias proves its future applicability to new and possibly more exotic samples to investigate.

References

- [1] J. M. D. Coey. *Magnetism and Magnetic Materials*. Cambridge University Press, 2009. ISBN 978-0-521-816144-4.
- [2] M. N. Baibich, J. M. Broto, A. Fert, F. Nguyen Van Dau, F. Petroff, P. Etienne, G. Creuzet, A. Friederich, and J. Chazelas. “Giant Magnetoresistance of (001)Fe/(001)Cr Magnetic Superlattices”. *Phys. Rev. Lett.*, **61**(21):2472–2475, November 1988. doi: 10.1103/PhysRevLett.61.2472.
- [3] G. Binasch, P. Grünberg, F. Saurenbach, and W. Zinn. “Enhanced magnetoresistance in layered magnetic structures with antiferromagnetic interlayer exchange”. *Phys. Rev. B*, **39**(7):4828–4830, March 1989. doi: 10.1103/PhysRevB.39.4828.
- [4] S. S. P. Parkin, Z. G. Li, and D. J. Smith. “Giant magnetoresistance in antiferromagnetic Co/Cu multilayers”. *Applied Physics Letters*, **58**(23):2710–2712, June 1991. doi: 10.1063/1.104765.
- [5] S. S. P. Parkin. “Giant Magnetoresistance in Magnetic Nanostructures”. *Annual Review of Materials Science*, **25**(1):357–388, 1995. doi: 10.1146/annurev.ms.25.080195.002041.
- [6] D. Weller and A. Moser. “Thermal effect limits in ultrahigh-density magnetic recording”. *IEEE Transactions on Magnetics*, **35**(6):4423–4439, November 1999. doi: 10.1109/20.809134.
- [7] S. S. P. Parkin, M. Hayashi, and L. Thomas. “Magnetic Domain-Wall Racetrack Memory”. *Science*, **320**(5873):190–194, November 2008. doi: 10.1126/science.1145799.
- [8] D. A. Allwood, G. Xiong, C. C. Faulkner, D. Atkinson, D. Petit, and R. P. Cowburn. “Magnetic Domain-Wall Logic”. *Science*, **309**(5741):1688–1692, September 2005. doi: 10.1126/science.1108813.
- [9] R. Hertel and J. Kirschner. “Magnetic drops in a soft-magnetic cylinder”. *Journal of Magnetism and Magnetic Materials*, **278**(3):L291–L297, July 2004. doi: 10.1016/j.jmmm.2004.02.032.
- [10] M. Yan, C. Andreas, A. Kákay, F. García-Sánchez, and R. Hertel. “Fast domain wall dynamics in magnetic nanotubes: Suppression of Walker breakdown and Cherenkov-like spin wave emission”. *Applied Physics Letters*, **99**(12):122505, September 2011. doi: 10.1063/1.3643037.
- [11] J. Escrig, P. Landeros, D. Altbir, E.E. Vogel, and P. Vargas. “Phase diagrams of magnetic nanotubes”. *Journal of Magnetism and Magnetic Materials*, **308**(2):233–237, January 2007. doi: 10.1016/j.jmmm.2006.05.019.
- [12] P. Landeros, S. Allende, J. Escrig, E. Salcedo, D. Altbir, and E. E Vogel. “Reversal modes in magnetic nanotubes”. *Applied Physics Letters*, **90**(10):102501–102501–3, March 2007. doi: 10.1063/1.2437655.

- [13] P. Landeros and A. S. Núñez. “Domain wall motion on magnetic nanotubes”. *Journal of Applied Physics*, **108**(3):033917–033917–10, August 2010. doi: doi:10.1063/1.3466747.
- [14] J A Otálora, J A López-López, A S Núñez, and P Landeros. “Domain wall manipulation in magnetic nanotubes induced by electric current pulses”. *Journal of Physics: Condensed Matter*, **24**(43):436007, October 2012. doi: 10.1088/0953-8984/24/43/436007.
- [15] M. Daub, M. Knez, U. Goesele, and K. Nielsch. “Ferromagnetic nanotubes by atomic layer deposition in anodic alumina membranes”. *Journal of Applied Physics*, **101**(9):09J111, May 2007. doi: 10.1063/1.2712057.
- [16] J. Bachmann, Jing, M. Knez, S. Barth, H. Shen, S. Mathur, U. Gösele, and K. Nielsch. “Ordered Iron Oxide Nanotube Arrays of Controlled Geometry and Tunable Magnetism by Atomic Layer Deposition”. *J. Am. Chem. Soc.*, **129**(31):9554–9555, August 2007. doi: 10.1021/ja072465w.
- [17] J. Meier, B. Doudin, and J.-Ph Ansermet. “Magnetic properties of nanosized wires”. *Journal of Applied Physics*, **79**(8):6010–6012, April 1996. doi: 10.1063/1.362136.
- [18] F. Tao, M. Guan, Y. Jiang, J. Zhu, Z. Xu, and Z. Xue. “An Easy Way to Construct an Ordered Array of Nickel Nanotubes: The Triblock-Copolymer-Assisted Hard-Template Method”. *Adv. Mater.*, **18**(16):2161–2164, August 2006. doi: 10.1002/adma.200600275.
- [19] Z. Liu, D. Zhang, S. Han, C. Li, B. Lei, W. Lu, J. Fang, and C. Zhou. “Single Crystalline Magnetite Nanotubes”. *J. Am. Chem. Soc.*, **127**(1):6–7, January 2005. doi: 10.1021/ja0445239.
- [20] D. Zhang, Z. Liu, S. Han, C. Li, B. Lei, M. P. Stewart, J. M. Tour, and C. Zhou. “Magnetite Fe₃O₄ coreshell nanowires:synthesis and magnetoresistance”. *Nano Lett.*, **4**(11):2151–2155, November 2004. doi: 10.1021/nl048758u.
- [21] D. Ruffer, M. Slot, R. Huber, T. Schwarze, F. Heimbach, G. Tütüncüoğlu, F. Matteini, E. Russo-Averchi, A. Kovács, R. Dunin-Borkowski, R. R. Zamani, J. R. Morante, J. Arbiol, A. Fontcuberta i Morral, and D. Grundler. “Anisotropic magnetoresistance of individual CoFeB and Ni nanotubes with values of up to 1.4% at room temperature”. *APL Materials*, **2**(7):076112, July 2014. doi: 10.1063/1.4891276.
- [22] D. Ruffer, R. Huber, P. Berberich, S. Albert, E. Russo-Averchi, M. Heiss, J. Arbiol, A. Fontcuberta i Morral, and D. Grundler. “Magnetic states of an individual Ni nanotube probed by anisotropic magnetoresistance”. *Nanoscale*, June 2012. doi: 10.1039/C2NR31086D.
- [23] G. C. Han, B. Y. Zong, P. Luo, and Y. H. Wu. “Angular dependence of the coercivity and remanence of ferromagnetic nanowire arrays”. *Journal of Applied Physics*, **93**(11):9202–9207, June 2003. doi: 10.1063/1.1572197.
- [24] J. Escrig, J. Bachmann, J. Jing, M. Daub, D. Altbir, and K. Nielsch. “Crossover between two different magnetization reversal modes in arrays of iron oxide nanotubes”. *Phys. Rev. B*, **77**(21):214421, June 2008. doi: 10.1103/PhysRevB.77.214421.
- [25] D. Li, R. S. Thompson, G. Bergmann, and J. G. Lu. “Template-based Synthesis and Magnetic Properties of Cobalt Nanotube Arrays”. *Adv. Mater.*, **20**(23):4575–4578, December 2008. doi: 10.1002/adma.200801455.

- [26] O. Albrecht, R. Zierold, S. Allende, J. Escrig, C. Patzig, B. Rauschenbach, K. Nielsch, and D. Görlitz. “Experimental evidence for an angular dependent transition of magnetization reversal modes in magnetic nanotubes”. *Journal of Applied Physics*, **109**(9): 093910, May 2011. doi: 10.1063/1.3583666.
- [27] J-E. Wegrowe, D. Kelly, A. Franck, S. E. Gilbert, and J.-Ph. Ansermet. “Magnetoresistance of Ferromagnetic Nanowires”. *Phys. Rev. Lett.*, **82**(18):3681–3684, May 1999. doi: 10.1103/PhysRevLett.82.3681.
- [28] B. C. Stipe, H. J. Mamin, T. D. Stowe, T. W. Kenny, and D. Rugar. “Magnetic Dissipation and Fluctuations in Individual Nanomagnets Measured by Ultrasensitive Cantilever Magnetometry”. *Phys. Rev. Lett.*, **86**(13):2874–2877, March 2001. doi: 10.1103/PhysRevLett.86.2874.
- [29] P. Banerjee, F. Wolny, D. V Pelekhov, M. R Herman, K. C Fong, U. Weissker, T. Mühl, Yu Obukhov, A. Leonhardt, B. Büchner, and P. Chris Hammel. “Magnetization reversal in an individual 25 nm iron-filled carbon nanotube”. *Applied Physics Letters*, **96**(25): 252505–252505–3, June 2010. doi: doi:10.1063/1.3440951.
- [30] D. P. Weber, D. Ruffer, A. Buchter, F. Xue, E. Russo-Averchi, R. Huber, P. Berberich, J. Arbiol, A. Fontcuberta i Morral, D. Grundler, and M. Poggio. “Cantilever Magnetometry of Individual Ni Nanotubes”. *Nano Lett.*, **12**(12):6139–6144, December 2012. doi: 10.1021/nl302950u.
- [31] W. Wernsdorfer, B. Doudin, D. Mailly, K. Hasselbach, A. Benoit, J. Meier, J. Ph. Ansermet, and B. Barbara. “Nucleation of Magnetization Reversal in Individual Nanosized Nickel Wires”. *Phys. Rev. Lett.*, **77**(9):1873–1876, 1996. doi: 10.1103/PhysRevLett.77.1873.
- [32] L. Hao, C. Aßmann, J. C Gallop, D. Cox, F. Ruede, O. Kazakova, P. Josephs-Franks, D. Drung, and Th Schurig. “Detection of single magnetic nanobead with a nano-superconducting quantum interference device”. *Applied Physics Letters*, **98**(9):092504, March 2011. doi: doi:10.1063/1.3561743.
- [33] T. Schwarz, R. Wölbing, C.F. Reiche, B. Müller, M.J. Martínez-Pérez, T. Mühl, B. Büchner, R. Kleiner, and D. Koelle. “Low-noise YBa₂Cu₃O₇ Nano-SQUIDS for Performing Magnetization-Reversal Measurements on Magnetic Nanoparticles”. *Phys. Rev. Applied*, **3**(4):044011, April 2015. doi: 10.1103/PhysRevApplied.3.044011.
- [34] C. Kittel. *Introduction to Solid State Physics*. Wiley, 8th edition, 2004. ISBN 978-0471415268.
- [35] R. Skomski and J. M. D. Coey. *Permanent Magnetism*. Institute of Physics Publishing, January 1999. ISBN 9780750304788.
- [36] A. Aharoni. *Introduction to the Theory of Ferromagnetism*. Oxford University Press, 2000. ISBN 9780198508090.
- [37] D. P. Weber. *Dynamic Cantilever Magnetometry of Individual Ferromagnetic Nanotubes*. PhD thesis, Universität Basel, Basel, Switzerland, 2014.
- [38] F. Reif. *Fundamentals of Statistical and Thermal Physics*. Waveland Press, Inc., 2009. ISBN 978-1-57766-612-7.

- [39] L. Duó, M. Finazzi, and F. Ciccacci (Eds.). *Magnetic properties of Antiferromagnetic Oxide Materials*. WILEY-VCH, 2010. ISBN 978-3-527-40881-8.
- [40] W. H. Meiklejohn and C. P. Bean. “New Magnetic Anisotropy”. *Phys. Rev.*, **102**(5): 1413–1414, June 1956. doi: 10.1103/PhysRev.102.1413.
- [41] W. H. Meiklejohn and C. P. Bean. “New Magnetic Anisotropy”. *Phys. Rev.*, **105**(3): 904–913, February 1957. doi: 10.1103/PhysRev.105.904.
- [42] M.P. Sharrock. “Recent advances in metal particulate recording media: toward the ultimate particle”. *IEEE Transactions on Magnetics*, **36**(5):2420–2425, September 2000. doi: 10.1109/20.908453.
- [43] S. A. Wolf, D. D. Awschalom, R. A. Buhrman, J. M. Daughton, S. von Molnár, M. L. Roukes, A. Y. Chtchelkanova, and D. M. Treger. “Spintronics: A Spin-Based Electronics Vision for the Future”. *Science*, **294**(5546):1488–1495, November 2001. doi: 10.1126/science.1065389.
- [44] J. Nogués, J. Sort, V. Langlais, V. Skumryev, S. Suriñach, J. S. Muñoz, and M. D. Baró. “Exchange bias in nanostructures”. *Physics Reports*, **422**(3):65–117, December 2005. doi: 10.1016/j.physrep.2005.08.004.
- [45] J Nogués and I K Schuller. “Exchange bias”. *Journal of Magnetism and Magnetic Materials*, **192**(2):203–232, February 1999. doi: 10.1016/S0304-8853(98)00266-2.
- [46] M. Kiwi. “Exchange bias theory”. *Journal of Magnetism and Magnetic Materials*, **234**(3):584–595, September 2001. doi: 10.1016/S0304-8853(01)00421-8.
- [47] C. Leighton, M. R. Fitzsimmons, A. Hoffmann, J. Dura, C. F. Majkrzak, M. S. Lund, and Ivan K. Schuller. “Thickness-dependent coercive mechanisms in exchange-biased bilayers”. *Phys. Rev. B*, **65**(6):064403, January 2002. doi: 10.1103/PhysRevB.65.064403.
- [48] T. J. Moran, J. M. Gallego, and Ivan K. Schuller. “Increased exchange anisotropy due to disorder at permalloy/CoO interfaces”. *Journal of Applied Physics*, **78**(3):1887–1891, August 1995. doi: 10.1063/1.360225.
- [49] D. Lederman, C. A. Ramos, V. Jaccarino, and J. L. Cardy. “Finite-size scaling in $\text{Fe}_2/\text{ZnFe}_2$ superlattices”. *Phys. Rev. B*, **48**(11):8365–8375, September 1993. doi: 10.1103/PhysRevB.48.8365.
- [50] T. Ambrose and C. L. Chien. “Finite-Size Effects and Uncompensated Magnetization in Thin Antiferromagnetic CoO Layers”. *Phys. Rev. Lett.*, **76**(10):1743–1746, March 1996. doi: 10.1103/PhysRevLett.76.1743.
- [51] C.-H. Lai, T. J. Regan, R. L. White, and T. C. Anthony. “Temperature dependence of magnetoresistance in spin valves with different thicknesses of NiO”. *Journal of Applied Physics*, **81**(8):3989–3991, April 1997. doi: 10.1063/1.364916.
- [52] S. Soeya, T. Imagawa, K. Mitsuoka, and S. Narishige. “Distribution of blocking temperature in bilayered $\text{Ni}_{81}\text{Fe}_{19}/\text{NiO}$ films”. *Journal of Applied Physics*, **76**(9):5356–5360, November 1994. doi: 10.1063/1.358488.
- [53] A. Hoffmann. “Symmetry Driven Irreversibilities at Ferromagnetic-Antiferromagnetic Interfaces”. *Phys. Rev. Lett.*, **93**(9):097203, August 2004. doi: 10.1103/PhysRevLett.93.097203.

- [54] D. Paccard, C. Schlenker, O. Massenet, R. Montmory, and A. Yelon. “A New Property of Ferromagnetic-Antiferromagnetic Coupling”. *phys. stat. sol. (b)*, **16**(1):301–311, January 1966. doi: 10.1002/pssb.19660160131.
- [55] T. Gredig, I. N. Krivorotov, and E. D. Dahlberg. “Magnetization reversal in exchange biased Co/CoO probed with anisotropic magnetoresistance”. *Journal of Applied Physics*, **91**(10):7760–7762, May 2002. doi: 10.1063/1.1447181.
- [56] A. P. Guimarães. *Principles of Nanomagnetism*. Springer Berlin Heidelberg, 2004. ISBN 978-3-642-01481-9.
- [57] A. H. Morrish. *The Physical Principles of Magnetism*. Wiley, January 2001. ISBN 9780780360297.
- [58] E. C. Stoner and E. P. Wohlfarth. “A Mechanism of Magnetic Hysteresis in Heterogeneous Alloys”. *Philosophical Transactions of the Royal Society of London A: Mathematical, Physical and Engineering Sciences*, **240**(826):599–642, May 1948. doi: 10.1098/rsta.1948.0007.
- [59] W. Wernsdorfer, C. Thirion, N. Demoncey, H. Pascard, and D. Mailly. “Magnetisation reversal by uniform rotation (Stoner–Wohlfarth model) in FCC cobalt nanoparticles”. *Journal of Magnetism and Magnetic Materials*, **242–245, Part 1**:132–138, April 2002. doi: 10.1016/S0304-8853(01)01153-2.
- [60] C. Thirion, W. Wernsdorfer, and D. Mailly. “Switching of magnetization by nonlinear resonance studied in single nanoparticles”. *Nat Mater*, **2**(8):524–527, August 2003. doi: 10.1038/nmat946.
- [61] L.-M. Lacroix, R. Bel Malaki, J. Carrey, S. Lachaize, M. Respaud, G. F. Goya, and B. Chaudret. “Magnetic hyperthermia in single-domain monodisperse FeCo nanoparticles: Evidences for Stoner–Wohlfarth behavior and large losses”. *Journal of Applied Physics*, **105**(2):023911, January 2009. doi: 10.1063/1.3068195.
- [62] E. H. Frei, S. Shtrikman, and D. Treves. “Critical Size and Nucleation Field of Ideal Ferromagnetic Particles”. *Phys. Rev.*, **106**(3):446–455, May 1957. doi: 10.1103/PhysRev.106.446.
- [63] J. A. Otálora, J. A. López-López, P. Vargas, and P. Landeros. “Chirality switching and propagation control of a vortex domain wall in ferromagnetic nanotubes”. *Applied Physics Letters*, **100**(7):072407, February 2012. doi: 10.1063/1.3687154.
- [64] T. Lottermoser, T. Lonkai, U. Amann, D. Hohlwein, J. Ihringer, and M. Fiebig. “Magnetic phase control by an electric field”. *Nature*, **430**(6999):541–544, July 2004. doi: 10.1038/nature02728.
- [65] P. Gambardella, S. S. Dhesi, S. Gardonio, C. Grazioli, P. Ohresser, and C. Carbone. “Localized Magnetic States of Fe, Co, and Ni Impurities on Alkali Metal Films”. *Phys. Rev. Lett.*, **88**(4):047202, January 2002. doi: 10.1103/PhysRevLett.88.047202.
- [66] K H J Buschow. “Intermetallic compounds of rare-earth and 3d transition metals”. *Reports on Progress in Physics*, **40**(10):1179–1256, October 1977. doi: 10.1088/0034-4885/40/10/002.
- [67] J. Stöhr, H. A. Padmore, S. Anders, T. Stammler, and M. R. Scheinfein. “Principles of X-Ray Magnetic Dichroism Spectromicroscopy”. *Surf. Rev. Lett.*, **05**(06):1297–1308,

December 1998. doi: 10.1142/S0218625X98001638.

- [68] P. Srivastava, F. Wilhelm, A. Ney, M. Farle, H. Wende, N. Haack, G. Ceballos, and K. Baberschke. “Magnetic moments and Curie temperatures of Ni and Co thin films and coupled trilayers”. *Phys. Rev. B*, **58**(9):5701–5706, September 1998. doi: 10.1103/PhysRevB.58.5701.
- [69] R. Hertel, O. Fruchart, S. Cherifi, P.-O. Jubert, S. Heun, A. Locatelli, and J. Kirschner. “Three-dimensional magnetic-flux-closure patterns in mesoscopic Fe islands”. *Phys. Rev. B*, **72**(21):214409, December 2005. doi: 10.1103/PhysRevB.72.214409.
- [70] V. Uhlřr, S. Pizzini, N. Rougemaille, J. Novotný, V. Cros, E. Jiménez, G. Faini, L. Heyne, F. Sirotti, C. Tieg, A. Bendounan, F. Maccherozzi, R. Belkhou, J. Grollier, A. Anane, and J. Vogel. “Current-induced motion and pinning of domain walls in spin-valve nanowires studied by XMCD-PEEM”. *Phys. Rev. B*, **81**(22):224418, June 2010. doi: 10.1103/PhysRevB.81.224418.
- [71] R. Streubel, F. Kronast, P. Fischer, D. Parkinson, O. G. Schmidt, and D. Makarov. “Retrieving spin textures on curved magnetic thin films with full-field soft X-ray microscopies”. *Nat Commun*, **6**, July 2015. doi: 10.1038/ncomms8612.
- [72] Petros N. Argyres. “Theory of the Faraday and Kerr Effects in Ferromagnetics”. *Phys. Rev.*, **97**(2):334–345, January 1955. doi: 10.1103/PhysRev.97.334.
- [73] J. F. Dillon Jr. “Optical Properties of Several Ferrimagnetic Garnets”. *Journal of Applied Physics*, **29**(3):539–541, March 1958. doi: 10.1063/1.1723215.
- [74] G. S. D. Beach, C. Nistor, C. Knutson, M. Tsoi, and J. L. Erskine. “Dynamics of field-driven domain-wall propagation in ferromagnetic nanowires”. *Nat Mater*, **4**(10):741–744, October 2005. doi: 10.1038/nmat1477.
- [75] R. P. Cowburn, D. K. Koltsov, A. O. Adeyeye, M. E. Welland, and D. M. Tricker. “Single-Domain Circular Nanomagnets”. *Phys. Rev. Lett.*, **83**(5):1042–1045, August 1999. doi: 10.1103/PhysRevLett.83.1042.
- [76] M. Schneider, H. Hoffmann, and J. Zweck. “Lorentz microscopy of circular ferromagnetic permalloy nanodisks”. *Applied Physics Letters*, **77**(18):2909–2911, October 2000. doi: 10.1063/1.1320465.
- [77] S. A. Majetich and Y. Jin. “Magnetization Directions of Individual Nanoparticles”. *Science*, **284**(5413):470–473, April 1999. doi: 10.1126/science.284.5413.470.
- [78] H. Lichte and M. Lehmann. “Electron holography—basics and applications”. *Reports on Progress in Physics*, **71**(1):016102, January 2008. doi: 10.1088/0034-4885/71/1/016102.
- [79] R. E. Dunin-Borkowski, M. R. McCartney, R. B. Frankel, D. A. Bazylinski, M. Pósfai, and P. R. Buseck. “Magnetic Microstructure of Magnetotactic Bacteria by Electron Holography”. *Science*, **282**(5395):1868–1870, April 1998. doi: 10.1126/science.282.5395.1868.
- [80] H. J. Hug, B. Stiefel, P. J. A. van Schendel, A. Moser, S. Martin, and H.-J. Güntherodt. “A low temperature ultrahigh vacuum scanning force microscope”. *Review of Scientific Instruments*, **70**(9):3625–3640, September 1999. doi: 10.1063/1.1149970.

- [81] J. J. Sáenz, N. García, P. Grütter, E. Meyer, H. Heinzelmann, R. Wiesendanger, L. Rosenthaler, H. R. Hidber, and H.-J. Güntherodt. “Observation of magnetic forces by the atomic force microscope”. *Journal of Applied Physics*, **62**(10):4293–4295, November 1987. doi: 10.1063/1.339105.
- [82] Y. Martin and H. K. Wickramasinghe. “Magnetic imaging by “force microscopy” with 1000 Å resolution”. *Applied Physics Letters*, **50**(20):1455–1457, May 1987. doi: 10.1063/1.97800.
- [83] D. Rugar, H. J. Mamin, P. Guethner, S. E. Lambert, J. E. Stern, I. McFadyen, and T. Yogi. “Magnetic force microscopy: General principles and application to longitudinal recording media”. *Journal of Applied Physics*, **68**(3):1169–1183, August 1990. doi: 10.1063/1.346713.
- [84] P. Maletinsky, S. Hong, M. S. Grinolds, B. Hausmann, M. D. Lukin, R. L. Walsworth, M. Loncar, and A. Yacoby. “A robust scanning diamond sensor for nanoscale imaging with single nitrogen-vacancy centres”. *Nat Nano*, **7**(5):320–324, May 2012. doi: 10.1038/nnano.2012.50.
- [85] J.-P. Tetienne, T. Hingant, L. J. Martínez, S. Rohart, A. Thiaville, L. Herrera Diez, K. Garcia, J.-P. Adam, J.-V. Kim, J.-F. Roch, I. M. Miron, G. Gaudin, L. Vila, B. Ocker, D. Ravelosona, and V. Jacques. “The nature of domain walls in ultrathin ferromagnets revealed by scanning nanomagnetometry”. *Nat Commun*, **6**:6733, April 2015. doi: 10.1038/ncomms7733.
- [86] M. E. Huber, N. C. Koshnick, H. Bluhm, L. J. Archuleta, T. Azua, P. G. Björnsson, B. W. Gardner, S. T. Halloran, E. A. Lucero, and K. A. Moler. “Gradiometric micro-SQUID susceptometer for scanning measurements of mesoscopic samples”. *Review of Scientific Instruments*, **79**(5):053704, May 2008. doi: 10.1063/1.2932341.
- [87] A. Finkler, Y. Segev, Y. Myasoedov, M. L. Rappaport, L. Neeman, D. Vasyukov, E. Zeldov, M. E. Huber, J. Martin, and A. Yacoby. “Self-Aligned Nanoscale SQUID on a Tip”. *Nano Lett.*, **10**(3):1046–1049, 2010. doi: 10.1021/nl100009r.
- [88] D. Vasyukov, Y. Anahory, L. Embon, D. Halbertal, J. Cuppens, L. Neeman, A. Finkler, Y. Segev, Y. Myasoedov, M. L. Rappaport, M. E. Huber, and E. Zeldov. “A scanning superconducting quantum interference device with single electron spin sensitivity”. *Nat Nano*, **8**(9):639–644, September 2013. doi: 10.1038/nnano.2013.169.
- [89] W. Thomson. “On the Electro-Dynamic Qualities of Metals:—Effects of Magnetization on the Electric Conductivity of Nickel and of Iron”. *Proc. R. Soc. Lond.*, **8**:546–550, January 1856. doi: 10.1098/rspl.1856.0144.
- [90] T. Taniyama, I. Nakatani, T. Namikawa, and Y. Yamazaki. “Resistivity due to Domain Walls in Co Zigzag Wires”. *Phys. Rev. Lett.*, **82**(13):2780–2783, March 1999. doi: 10.1103/PhysRevLett.82.2780.
- [91] C.D. Graham. “High-sensitivity magnetization measurements”. *Journal of Materials Sciences and Technology*, **16**(02):97, 2000.
- [92] J. Jang, R. Budakian, and Y. Maeno. “Phase-locked cantilever magnetometry”. *Applied Physics Letters*, **98**(13):132510–132510–3, March 2011. doi: doi:10.1063/1.3572026.

- [93] B. Gross, D. P. Weber, D. Ruffer, A. Buchter, F. Heimbach, A. Fontcuberta i Morral, D. Grundler, and M. Poggio. “Dynamic cantilever magnetometry of individual CoFeB nanotubes”. *arXiv:1512.00621 [cond-mat]*, December 2015.
- [94] M. Tinkham. *Introduction To Superconductivity*. McGraw-Hill, Inc., 2nd edition, 1996. ISBN 0-07-064878-6.
- [95] J. Clarke and A. I. Braginski. *The SQUID Handbook Vol. I*. Wiley, 2004. ISBN 3-527-40229-2.
- [96] J. File and R. G. Mills. “Observation of Persistent Current in a Superconducting Solenoid”. *Phys. Rev. Lett.*, **10**(3):93–96, February 1963. doi: 10.1103/PhysRevLett.10.93.
- [97] J. Bardeen, L. N. Cooper, and J. R. Schrieffer. “Theory of Superconductivity”. *Phys. Rev.*, **108**(5):1175–1204, December 1957. doi: 10.1103/PhysRev.108.1175.
- [98] W. Meissner and R. Ochsenfeld. “Ein neuer Effekt bei Eintritt der Supraleitfähigkeit”. *Naturwissenschaften*, **21**(44):787–788, November 1933. doi: 10.1007/BF01504252.
- [99] F. London and H. London. “The Electromagnetic Equations of the Supraconductor”. *Royal Society of London Proceedings Series A*, **149**:71–88, March 1935. doi: 10.1098/rspa.1935.0048.
- [100] D. K. Finnemore, T. F. Stromberg, and C. A. Swenson. “Superconducting Properties of High-Purity Niobium”. *Phys. Rev.*, **149**(1):231–243, September 1966. doi: 10.1103/PhysRev.149.231.
- [101] A.A. Abrikosov. “The magnetic properties of superconducting alloys”. *Journal of Physics and Chemistry of Solids*, **2**(3):199–208, January 1957. doi: 10.1016/0022-3697(57)90083-5.
- [102] P. Schmüser. “Superconductivity”. URL <http://www.desy.de/~pschmues/Superconductivity.pdf>.
- [103] B. S. Deaver and W. M. Fairbank. “Experimental Evidence for Quantized Flux in Superconducting Cylinders”. *Phys. Rev. Lett.*, **7**(2):43–46, July 1961. doi: 10.1103/PhysRevLett.7.43.
- [104] H. F. Hess, R. B. Robinson, R. C. Dynes, J. M. Valles, and J. V. Waszczak. “Scanning-Tunneling-Microscope Observation of the Abrikosov Flux Lattice and the Density of States near and inside a Fluxoid”. *Phys. Rev. Lett.*, **62**(2):214–216, January 1989. doi: 10.1103/PhysRevLett.62.214.
- [105] E H Brandt. “The flux-line lattice in superconductors”. *Reports on Progress in Physics*, **58**(11):1465–1594, November 1995. doi: 10.1088/0034-4885/58/11/003.
- [106] M. Kemmler, C. Gürlich, A. Sterck, H. Pöhler, M. Neuhaus, M. Siegel, R. Kleiner, and D. Koelle. “Commensurability Effects in Superconducting Nb Films with Quasiperiodic Pinning Arrays”. *Phys. Rev. Lett.*, **97**(14):147003, October 2006. doi: 10.1103/PhysRevLett.97.147003.
- [107] B. D. Josephson. “Possible new effects in superconductive tunnelling”. *Physics Letters*, **1**(7):251–253, July 1962. doi: 10.1016/0031-9163(62)91369-0.

- [108] A. Steinbach, P. Joyez, A. Cottet, D. Esteve, M. H. Devoret, M. E. Huber, and J. M. Martinis. “Direct Measurement of the Josephson Supercurrent in an Ultra-small Josephson Junction”. *Phys. Rev. Lett.*, **87**(13):137003, September 2001. doi: 10.1103/PhysRevLett.87.137003.
- [109] T J Quinn. “News from the BIPM”. *Metrologia*, **26**(1):69–74, January 1989. doi: 10.1088/0026-1394/26/1/006.
- [110] R. Behr, O. Kieler, J. Kohlmann, F. Müller, and L. Palafox. “Development and metrological applications of Josephson arrays at PTB”. *Measurement Science and Technology*, **23**(12):124002, December 2012. doi: 10.1088/0957-0233/23/12/124002.
- [111] T. Ryhänen, H. Seppä, R. Ilmoniemi, and J. Knuutila. “SQUID magnetometers for low-frequency applications”. *J Low Temp Phys*, **76**(5-6):287–386, September 1989. doi: 10.1007/BF00681735.
- [112] D. E. McCumber. “Effect of ac Impedance on dc Voltage Current Characteristics of Superconductor Weak Link Junctions”. *Journal of Applied Physics*, **39**(7):3113–3118, June 1968. doi: 10.1063/1.1656743.
- [113] W. C. Stewart. “CURRENT VOLTAGE CHARACTERISTICS OF JOSEPHSON JUNCTIONS”. *Applied Physics Letters*, **12**(8):277–280, April 1968. doi: 10.1063/1.1651991.
- [114] K. Sternickel and A. I. Braginski. “Biomagnetism using SQUIDs: status and perspectives”. *Supercond. Sci. Technol.*, **19**(3):S160, March 2006. doi: 10.1088/0953-2048/19/3/024.
- [115] R. Wölbing. *NanoSQUIDs for Studies on the Magnetization Reversal of Individual Magnetic Nanoparticles*. PhD thesis, Universität Tübingen, Tübingen, Germany, 2015.
- [116] M. S. Colclough G. Zaharchuk R. W. Simon, M. J. Burns and R. Cantor. “Mr. squid user’s guide”, August 2003. URL <http://www.starcryo.com/mrsqm622.pdf>.
- [117] J. Nagel, O. F. Kieler, T. Weimann, R. Wölbing, J. Kohlmann, A. B. Zorin, R. Kleiner, D. Koelle, and M. Kemmler. “Superconducting quantum interference devices with submicron nb/hfti/nb junctions for investigation of small magnetic particles”. *Applied Physics Letters*, **99**:032506, 2011. doi: 10.1063/1.3614437.
- [118] T. Schwarz, J. Nagel, R. Wölbing, M. Kemmler, R. Kleiner, and D. Koelle. “Low-Noise Nano Superconducting Quantum Interference Device Operating in Tesla Magnetic Fields”. *ACS Nano*, **7**(1):844–850, January 2013. doi: 10.1021/nn305431c.
- [119] B.W. Chui, Y. Hishinuma, R. Budakian, H.J. Mamin, T.W. Kenny, and D. Rugar. “Mass-loaded cantilevers with suppressed higher-order modes for magnetic resonance force microscopy”. In *TRANSDUCERS, Solid-State Sensors, Actuators and Microsystems, 12th International Conference on, 2003*, volume 2, pages 1120–1123 vol.2, June 2003. doi: 10.1109/SENSOR.2003.1216966.
- [120] F. Xue, D. P. Weber, P. Peddibhotla, and M. Poggio. “Measurement of statistical nuclear spin polarization in a nanoscale GaAs sample”. *Phys. Rev. B*, **84**(20):205328, November 2011. doi: 10.1103/PhysRevB.84.205328.
- [121] M. Montinaro. *Coupling of Nanomechanical Resonators to Controllable Quantum Systems*. PhD thesis, Universität Basel, Basel, Switzerland, 2014.

- [122] A. N. Cleland. *Foundations of Nanomechanics From Solid-State Theory to Device Applications*. Springer Berlin Heidelberg, 2003. ISBN 9783662052877 3662052873.
- [123] P. Peddibhotla. *Magnetic Resonance Force Microscopy: Harnessing Nuclear Spin Fluctuations*. PhD thesis, Universität Basel, Basel, Switzerland, 2013.
- [124] D. Ruffer. *Magnetic States and Spin-Wave Modes in Single Ferromagnetic Nanotubes*. PhD thesis, EPFL, Lausanne, Switzerland, 2014.
- [125] Haiming Yu, R. Huber, T. Schwarze, F. Brandl, T. Rapp, P. Berberich, G. Duerr, and D. Grundler. “High propagating velocity of spin waves and temperature dependent damping in a CoFeB thin film”. *Applied Physics Letters*, **100**(26):262412, June 2012. doi: 10.1063/1.4731273.
- [126] T. Schwarze and D. Grundler. “Magnonic crystal wave guide with large spin-wave propagation velocity in CoFeB”. *Applied Physics Letters*, **102**(22):222412, June 2013. doi: 10.1063/1.4809757.
- [127] L. Heyne, M. Kläui, D. Backes, P. Möhrke, T. A. Moore, J. G. Kimling, O. Boulle, U. Rüdiger, L. J. Heyderman, A. Fraile Rodríguez, F. Nolting, K. Kirsch, and R. Mattheis. “Direct imaging of current-induced domain wall motion in CoFeB structures”. *Journal of Applied Physics*, **103**(7):07D928, April 2008. doi: 10.1063/1.2836326.
- [128] L. F. Yin, D. H. Wei, N. Lei, L. H. Zhou, C. S. Tian, G. S. Dong, X. F. Jin, L. P. Guo, Q. J. Jia, and R. Q. Wu. “Magnetocrystalline Anisotropy in Permalloy Revisited”. *Phys. Rev. Lett.*, **97**(6):067203, August 2006. doi: 10.1103/PhysRevLett.97.067203.
- [129] A. Thiaville, Y. Nakatani, J. Miltat, and Y. Suzuki. “Micromagnetic understanding of current-driven domain wall motion in patterned nanowires”. *EPL*, **69**(6):990, March 2005. doi: 10.1209/epl/i2004-10452-6.
- [130] R. Ranchal, C. Aroca, and E. López. “Domain walls and exchange-interaction in Permalloy/Gd films”. *New J. Phys.*, **10**(1):013013, January 2008. doi: 10.1088/1367-2630/10/1/013013.
- [131] Narishige. “Setting values in the pc-10 puller (revised)”, May 2011. URL <http://news.narishige-group.com/pdf/news051en.pdf>.
- [132] Narishige. “Setting values in the pc-10 puller”, March 2007. URL <http://news.narishige-group.com/pdf/news001en.pdf>.
- [133] S. Blomeier, D. McGrouther, R. O’Neill, S. McVitie, J. N. Chapman, M. C. Weber, B. Hillebrands, and J. Fassbender. “Modification of the magnetic properties of exchange coupled NiFe/FeMn films by Ga⁺ ion irradiation”. *Journal of Magnetism and Magnetic Materials*, **290–291, Part 1**:731–734, April 2005. doi: 10.1016/j.jmmm.2004.11.278.
- [134] D Hagedorn, O Kieler, R Dolata, R Behr, F Müller, J Kohlmann, and J Niemeyer. “Modified fabrication of planar sub- μm superconductor–normal metal–superconductor Josephson junctions for use in a Josephson arbitrary waveform synthesizer”. *Superconductor Science and Technology*, **19**(4):294–298, April 2006. doi: 10.1088/0953-2048/19/4/009.
- [135] L. Thomas, F. Lioni, R. Ballou, D. Gatteschi, R. Sessoli, and B. Barbara. “Macroscopic quantum tunnelling of magnetization in a single crystal of nanomagnets”. *Nature*, **383** (6596):145–147, September 1996. doi: 10.1038/383145a0.

- [136] D. Gatteschi and R. Sessoli. “Quantum Tunneling of Magnetization and Related Phenomena in Molecular Materials”. *Angewandte Chemie International Edition*, **42**(3):268–297, January 2003. doi: 10.1002/anie.200390099.
- [137] L. Bogani and W. Wernsdorfer. “Molecular spintronics using single-molecule magnets”. *Nat Mater*, **7**(3):179–186, March 2008. doi: 10.1038/nmat2133.
- [138] L. Bogani, A. Vindigni, R. Sessoli, and D. Gatteschi. “Single chain magnets: where to from here?”. *J. Mater. Chem.*, **18**(40):4750–4758, October 2008. doi: 10.1039/B807824F.
- [139] P. Bushev, D. Bothner, J. Nagel, M. Kemmler, K. B. Konovalenko, A. Lörincz, K. Ilin, M. Siegel, D. Koelle, R. Kleiner, and F. Schmidt-Kaler. “Trapped electron coupled to superconducting devices”. *Eur. Phys. J. D*, **63**(1):9–16, April 2011. doi: 10.1140/epjd/e2011-10517-6.
- [140] J. Fortágh and C. Zimmermann. “Toward Atom Chips”. *Science*, **307**(5711):860–861, November 2005. doi: 10.1126/science.1107348.
- [141] J. R. Maze, P. L. Stanwix, J. S. Hodges, S. Hong, J. M. Taylor, P. Cappellaro, L. Jiang, M. V. Gurudev Dutt, E. Togan, A. S. Zibrov, A. Yacoby, R. L. Walsworth, and M. D. Lukin. “Nanoscale magnetic sensing with an individual electronic spin in diamond”. *Nature*, **455**(7213):644–647, October 2008. doi: 10.1038/nature07279.
- [142] G. Balasubramanian, I. Y. Chan, R. Kolesov, M. Al-Hmoud, J. Tisler, C. Shin, C. Kim, A. Wojcik, P. R. Hemmer, A. Krueger, T. Hanke, A. Leitenstorfer, R. Bratschitsch, F. Jelezko, and J. Wrachtrup. “Nanoscale imaging magnetometry with diamond spins under ambient conditions”. *Nature*, **455**(7213):648–651, October 2008. doi: 10.1038/nature07278.
- [143] D. Rugar, R. Budakian, H. J. Mamin, and B. W. Chui. “Single spin detection by magnetic resonance force microscopy”. *Nature*, **430**(6997):329–332, July 2004. doi: 10.1038/nature02658.
- [144] Y. Manassen, R. J. Hamers, J. E. Demuth, and A. J. Castellano Jr. “Direct observation of the precession of individual paramagnetic spins on oxidized silicon surfaces”. *Phys. Rev. Lett.*, **62**(21):2531–2534, May 1989. doi: 10.1103/PhysRevLett.62.2531.
- [145] C. Durkan and M. E. Welland. “Electronic spin detection in molecules using scanning-tunneling-microscopy-assisted electron-spin resonance”. *Applied Physics Letters*, **80**(3):458–460, January 2002. doi: 10.1063/1.1434301.
- [146] W. Wernsdorfer. “Classical and Quantum Magnetization Reversal Studied in Nanometer-Sized Particles and Clusters”. In I. Prigogine and S. A. Rice, editors, *Advances in Chemical Physics*, pages 99–190. John Wiley & Sons, Inc., 2001.
- [147] J. Gallop. “SQUIDS: some limits to measurement”. *Superconductor Science and Technology*, **16**(12):1575–1582, December 2003. doi: 10.1088/0953-2048/16/12/055.
- [148] Z. K. Wang, M. H. Kuok, S. C. Ng, D. J. Lockwood, M. G. Cottam, K. Nielsch, R. B. Wehrspohn, and U. Gösele. “Spin-Wave Quantization in Ferromagnetic Nickel Nanowires”. *Phys. Rev. Lett.*, **89**(2):027201, June 2002. doi: 10.1103/PhysRevLett.89.027201.
- [149] J. Topp, J. Podbielski, D. Heitmann, and D. Grundler. “Internal spin-wave confinement in magnetic nanowires due to zig-zag shaped magnetization”. *Phys. Rev. B*, **78**(2):

- 024431, July 2008. doi: 10.1103/PhysRevB.78.024431.
- [150] R. Streubel, D. J. Thurmer, D. Makarov, F. Kronast, T. Kosub, V. Kravchuk, D. D. Sheka, Y. Gaididei, R. Schäfer, and O. G. Schmidt. “Magnetically Capped Rolled-up Nanomembranes”. *Nano Lett.*, **12**(8):3961–3966, August 2012. doi: 10.1021/nl301147h.
- [151] R. Streubel, V. P. Kravchuk, D. D. Sheka, D. Makarov, F. Kronast, O. G. Schmidt, and Y. Gaididei. “Equilibrium magnetic states in individual hemispherical permalloy caps”. *Applied Physics Letters*, **101**(13):132419, September 2012. doi: 10.1063/1.4756708.
- [152] R. Kleiner, D. Koelle, F. Ludwig, and J. Clarke. “Superconducting quantum interference devices: State of the art and applications”. *Proceedings of the IEEE*, **92**(10):1534–1548, October 2004. doi: 10.1109/JPROC.2004.833655.
- [153] C P Foley and H Hilgenkamp. “Why NanoSQUIDs are important: an introduction to the focus issue”. *Superconductor Science and Technology*, **22**(6):064001, June 2009. doi: 10.1088/0953-2048/22/6/064001.
- [154] M.B. Ketchen, D.D. Awschalom, W.J. Gallagher, A.W. Kleinsasser, R.L. Sandstrom, J.R. Rozen, and B. Bumble. “Design, fabrication, and performance of integrated miniature SQUID susceptometers”. *IEEE Transactions on Magnetism*, **25**(2):1212–1215, March 1989. doi: 10.1109/20.92513.
- [155] V Bouchiat. “Detection of magnetic moments using a nano-SQUID: limits of resolution and sensitivity in near-field SQUID magnetometry”. *Superconductor Science and Technology*, **22**(6):064002, June 2009. doi: 10.1088/0953-2048/22/6/064002.
- [156] J Nagel, K B Konovalenko, M Kemmler, M Turad, R Werner, E Kleisz, S Menzel, R Klingeler, B Büchner, R Kleiner, and D Koelle. “Resistively shunted YBa₂Cu₃O₇ grain boundary junctions and low-noise SQUIDs patterned by a focused ion beam down to 80 nm linewidth”. *Superconductor Science and Technology*, **24**:015015, January 2011. doi: 10.1088/0953-2048/24/1/015015.
- [157] R. F. Voss, R. B. Laibowitz, and A. N. Broers. “Niobium nanobridge dc SQUID”. *Applied Physics Letters*, **37**(7):656–658, October 1980. doi: 10.1063/1.92026.
- [158] A. G. P. Troeman, H. Derking, B. Borger, J. Pleikies, D. Veldhuis, and H. Hilgenkamp. “NanoSQUIDs Based on Niobium Constrictions”. *Nano Lett.*, **7**(7):2152–2156, July 2007. doi: 10.1021/nl070870f.
- [159] L. Hao, J. C. Macfarlane, J. C. Gallop, D. Cox, J. Beyer, D. Drung, and T. Schurig. “Measurement and noise performance of nano-superconducting-quantum-interference devices fabricated by focused ion beam”. *Applied Physics Letters*, **92**(19):192507, May 2008. doi: 10.1063/1.2917580.
- [160] V. Bouchiat, M. Faucher, C. Thirion, W. Wernsdorfer, T. Fournier, and B. Pannetier. “Josephson junctions and superconducting quantum interference devices made by local oxidation of niobium ultrathin films”. *Applied Physics Letters*, **79**(1):123–125, July 2001. doi: 10.1063/1.1382626.
- [161] M Faucher, P O Jubert, O Fruchart, W Wernsdorfer, and V Bouchiat. “Optimizing the flux coupling between a nanoSQUID and a magnetic particle using atomic force microscope nanolithography”. *Superconductor Science and Technology*, **22**(6):064010, June 2009. doi: 10.1088/0953-2048/22/6/064010.

- [162] J.-P. Cleuziou, W. Wernsdorfer, V. Bouchiat, T. Ondarçuhu, and M. Monthieux. “Carbon nanotube superconducting quantum interference device”. *Nat Nano*, **1**(1):53–59, October 2006. doi: 10.1038/nnano.2006.54.
- [163] R. Wölbling, J. Nagel, T. Schwarz, O. Kieler, T. Weimann, J. Kohlmann, A. B. Zorin, M. Kemmler, R. Kleiner, and D. Koelle. “Nb nano superconducting quantum interference devices with high spin sensitivity for operation in magnetic fields up to 0.5 T”. *Applied Physics Letters*, **102**(19):192601–192601–4, May 2013. doi: doi:10.1063/1.4804673.
- [164] C. Granata, A. Vettoliere, R. Russo, E. Esposito, M. Russo, and B. Ruggiero. “Supercurrent decay in nano-superconducting quantum interference devices for intrinsic magnetic flux resolution”. *Applied Physics Letters*, **94**(6):062503, February 2009. doi: 10.1063/1.3078519.
- [165] A. Moser, H. J. Hug, I. Parashikov, B. Stiefel, O. Fritz, H. Thomas, A. Baratoff, H.-J. Güntherodt, and P. Chaudhari. “Observation of Single Vortices Condensed into a Vortex-Glass Phase by Magnetic Force Microscopy”. *Phys. Rev. Lett.*, **74**(10):1847–1850, March 1995. doi: 10.1103/PhysRevLett.74.1847.
- [166] A Volodin, K Temst, C. Van Haesendonck, Y Bruynseraede, M. I Montero, and I. K Schuller. “Magnetic-force microscopy of vortices in thin niobium films: Correlation between the vortex distribution and the thickness-dependent film morphology”. *Europhysics Letters (EPL)*, **58**(4):582–588, May 2002. doi: 10.1209/epl/i2002-00435-1.
- [167] D Hagedorn, R Dolata, F.-Im Buchholz, and J Niemeyer. “Properties of SNS Josephson junctions with HfTi interlayers”. *Physica C: Superconductivity*, **372–376**, Part 1(0): 7–10, August 2002. doi: 10.1016/S0921-4534(02)00688-3.
- [168] D. J. Van Harlingen, Roger H. Koch, and J. Clarke. “Superconducting quantum interference device with very low magnetic flux noise energy”. *Applied Physics Letters*, **41**(2):197–199, July 1982. doi: 10.1063/1.93460.
- [169] U. Gysin, S. Rast, M. Kisiel, C. Werle, and E. Meyer. “Low temperature ultrahigh vacuum noncontact atomic force microscope in the pendulum geometry”. *Review of Scientific Instruments*, **82**(2):023705, February 2011. doi: 10.1063/1.3551603.
- [170] H. J. Mamin, R. Budakian, B. W. Chui, and D. Rugar. “Detection and Manipulation of Statistical Polarization in Small Spin Ensembles”. *Phys. Rev. Lett.*, **91**(20):207604, November 2003. doi: 10.1103/PhysRevLett.91.207604.
- [171] D. Rugar, H. J. Mamin, and P. Guethner. “Improved fiber-optic interferometer for atomic force microscopy”. *Appl. Phys. Lett.*, **55**(25):2588, 1989. doi: 10.1063/1.101987.
- [172] S Kuehn, R. F. Loring, and J. A. Marohn. “Dielectric Fluctuations and the Origins of Noncontact Friction”. *Phys. Rev. Lett.*, **96**(15):156103, April 2006. doi: 10.1103/PhysRevLett.96.156103.
- [173] K. Kim, Y. Seo, H. Jang, S. Chang, M.-H. Hong, and W. Jhe. “Shear-mode magnetic force microscopy with a quartz tuning fork in ambient conditions”. *Nanotechnology*, **17**(7):S201–S204, April 2006. doi: 10.1088/0957-4484/17/7/S17.
- [174] M.M. Khapaev, A.Yu. Kidiyarova-Shevchenko, P. Magnelind, and M.Yu. Kupriyanov. “3d-MLSI: software package for inductance calculation in multilayer superconducting integrated circuits”. *IEEE Transactions on Applied Superconductivity*, **11**(1):1090–1093,

March 2001. doi: 10.1109/77.919537.

- [175] O. Usenko, A. Vinante, G. Wijts, and T. H. Oosterkamp. “A superconducting quantum interference device based read-out of a subattonewton force sensor operating at millikelvin temperatures”. *Applied Physics Letters*, **98**(13):133105, March 2011. doi: 10.1063/1.3570628.
- [176] A. Vinante, G. Wijts, O. Usenko, L. Schinkelshoek, and T. H. Oosterkamp. “Magnetic resonance force microscopy of paramagnetic electron spins at millikelvin temperatures”. *Nat Commun*, **2**:572, December 2011. doi: 10.1038/ncomms1581.
- [177] A. Vinante, A. Kirste, A. den Haan, O. Usenko, G. Wijts, E. Jeffrey, P. Sonin, D. Bouwmeester, and T. H. Oosterkamp. “High sensitivity SQUID-detection and feedback-cooling of an ultrasoft microcantilever”. *Applied Physics Letters*, **101**(12):123101–123101–4, September 2012. doi: doi:10.1063/1.4752766.
- [178] A. Buchter, J. Nagel, D. Ruffer, F. Xue, D. P. Weber, O. F. Kieler, T. Weimann, J. Kohlmann, A. B. Zorin, E. Russo-Averchi, R. Huber, P. Berberich, A. Fontcuberta i Morral, M. Kemmler, R. Kleiner, D. Koelle, D. Grundler, and M. Poggio. “Reversal Mechanism of an Individual Ni Nanotube Simultaneously Studied by Torque and SQUID Magnetometry”. *Phys. Rev. Lett.*, **111**(6):067202, August 2013. doi: 10.1103/PhysRevLett.111.067202.
- [179] S. Khizroev, M. H. Kryder, D. Litvinov, and D. A. Thompson. “Direct observation of magnetization switching in focused-ion-beam-fabricated magnetic nanotubes”. *Applied Physics Letters*, **81**(12):2256–2257, September 2002. doi: 10.1063/1.1508164.
- [180] M Poggio and C L Degen. “Force-detected nuclear magnetic resonance: recent advances and future challenges”. *Nanotechnology*, **21**(34):342001, August 2010. doi: 10.1088/0957-4484/21/34/342001.
- [181] H Campanella, M Jaafar, J Llobet, J Esteve, M Vázquez, A Asenjo, R P del Real, and J A Plaza. “Nanomagnets with high shape anisotropy and strong crystalline anisotropy: perspectives on magnetic force microscopy”. *Nanotechnology*, **22**(50):505301, December 2011. doi: 10.1088/0957-4484/22/50/505301.
- [182] M. M. Maqableh, X. Huang, S.-Y. Sung, K. S. M. Reddy, G. Norby, R. H. Victora, and B. J. H. Stadler. “Low-Resistivity 10 nm Diameter Magnetic Sensors”. *Nano Lett.*, **12**(8):4102–4109, August 2012. doi: 10.1021/nl301610z.
- [183] P. Landeros, O. J. Suarez, A. Cuchillo, and P. Vargas. “Equilibrium states and vortex domain wall nucleation in ferromagnetic nanotubes”. *Phys. Rev. B*, **79**(2):024404, January 2009. doi: 10.1103/PhysRevB.79.024404.
- [184] J. Escrig, S. Allende, D. Altbir, and M. Bahiana. “Magnetostatic interactions between magnetic nanotubes”. *Applied Physics Letters*, **93**(2):023101, July 2008. doi: 10.1063/1.2956681.
- [185] J. Bachmann, J. Escrig, K. Pitzschel, J. M. Montero Moreno, J. Jing, D. Görlitz, D. Altbir, and K. Nielsch. “Size effects in ordered arrays of magnetic nanotubes: Pick your reversal mode”. *Journal of Applied Physics*, **105**(7):07B521, April 2009. doi: 10.1063/1.3074109.

- [186] J. Nagel, A. Buchter, F. Xue, O. F. Kieler, T. Weimann, J. Kohlmann, A. B. Zorin, D. Ruffer, E. Russo-Averchi, R. Huber, P. Berberich, A. Fontcuberta i Morral, D. Grundler, R. Kleiner, D. Koelle, M. Poggio, and M. Kemmler. “Nanoscale multifunctional sensor formed by a Ni nanotube and a scanning Nb nanoSQUID”. *Phys. Rev. B*, **88**(6):064425, August 2013. doi: 10.1103/PhysRevB.88.064425.
- [187] T. Fischbacher, M. Franchin, G. Bordignon, and H. Fangohr. “A Systematic Approach to Multiphysics Extensions of Finite-Element-Based Micromagnetic Simulations: Nmag”. *IEEE Transactions on Magnetics*, **43**(6):2896–2898, June 2007. doi: 10.1109/TMAG.2007.893843.
- [188] A. Knittel. *Micromagnetic simulations of three dimensional core-shell nanostructures*. PhD thesis, University of Southampton, Southampton, UK, 2011.
- [189] G Meier, D Grundler, K. B Brooks, Ch Heyn, and D Heitmann. “Effect of tilted magnetic fields on bistable nanomagnets in hybrid semiconductor/ferromagnet devices”. *Journal of Magnetism and Magnetic Materials*, **210**(1–3):138–142, February 2000. doi: 10.1016/S0304-8853(99)00625-3.
- [190] P Zhang, F Zuo, F. K Urban III, A Khabari, P Griffiths, and A Hosseini-Tehrani. “Irreversible magnetization in nickel nanoparticles”. *Journal of Magnetism and Magnetic Materials*, **225**(3):337–345, 2001. doi: 10.1016/S0304-8853(00)01379-2.
- [191] M. Gierlings, M. J. Prandolini, H. Fritzsche, M. Gruyters, and D. Riegel. “Change and asymmetry of magnetization reversal for a Co/CoO exchange-bias system”. *Phys. Rev. B*, **65**(9):092407, February 2002. doi: 10.1103/PhysRevB.65.092407.
- [192] A.-P. Chen, J. M. Gonzalez, and K. Y. Guslienko. “Magnetization configurations and reversal of magnetic nanotubes with opposite chiralities of the end domains”. *Journal of Applied Physics*, **109**(7):073923, April 2011. doi: 10.1063/1.3562190.
- [193] J. Escrig, P. Landeros, D. Altbir, and E.E. Vogel. “Effect of anisotropy in magnetic nanotubes”. *Journal of Magnetism and Magnetic Materials*, **310**(2, Part 3):2448–2450, March 2007. doi: 10.1016/j.jmmm.2006.10.910.
- [194] C. Binek. “Training of the exchange-bias effect: A simple analytic approach”. *Phys. Rev. B*, **70**(1):014421, July 2004. doi: 10.1103/PhysRevB.70.014421.
- [195] M. P. Proenca, J. Ventura, C. T. Sousa, M. Vazquez, and J. P. Araujo. “Exchange bias, training effect, and bimodal distribution of blocking temperatures in electrodeposited core-shell nanotubes”. *Phys. Rev. B*, **87**(13):134404, April 2013. doi: 10.1103/PhysRevB.87.134404.
- [196] T. Kosub, A. Bachmatiuk, D. Makarov, S. Baunack, V. Neu, A. Wolter, M. H. Rummeli, and O. G. Schmidt. “Exchange bias related coercivity enhancement as a characterization tool”. *Journal of Applied Physics*, **112**(12):123917, December 2012. doi: 10.1063/1.4770223.
- [197] D. L. Cortie, K.-W. Lin, C. Shueh, H.-F. Hsu, X. L. Wang, M. James, H. Fritzsche, S. Brück, and F. Klose. “Exchange bias in a nanocrystalline hematite/permalloy thin film investigated with polarized neutron reflectometry”. *Phys. Rev. B*, **86**(5):054408, August 2012. doi: 10.1103/PhysRevB.86.054408.

- [198] E. Fulcomer and S. H. Charap. “Temperature and frequency dependence of exchange anisotropy effects in oxidized NiFe films”. *Journal of Applied Physics*, **43**(10):4184–4190, October 1972. doi: 10.1063/1.1660893.
- [199] L. Le Guyader, A. Kleibert, A. Fraile Rodríguez, S. El Moussaoui, A. Balan, M. Buzzi, J. Raabe, and F. Nolting. “Studying nanomagnets and magnetic heterostructures with X-ray PEEM at the Swiss Light Source”. *Journal of Electron Spectroscopy and Related Phenomena*, **185**(10):371–380, October 2012. doi: 10.1016/j.elspec.2012.03.001.
- [200] A. Fraile Rodríguez, F. Nolting, J. Bansmann, A. Kleibert, and L. J. Heyderman. “X-ray imaging and spectroscopy of individual cobalt nanoparticles using photoemission electron microscopy”. *Journal of Magnetism and Magnetic Materials*, **316**(2):426–428, September 2007. doi: 10.1016/j.jmmm.2007.03.093.
- [201] C. a. F. Vaz, A. Balan, F. Nolting, and A. Kleibert. “In situ magnetic and electronic investigation of the early stage oxidation of Fe nanoparticles using X-ray photo-emission electron microscopy”. *Phys. Chem. Chem. Phys.*, **16**(48):26624–26630, November 2014. doi: 10.1039/C4CP02725F.
- [202] T. J. Regan, H. Ohldag, C. Stamm, F. Nolting, J. Lüning, J. Stöhr, and R. L. White. “Chemical effects at metal/oxide interfaces studied by x-ray-absorption spectroscopy”. *Phys. Rev. B*, **64**(21):214422, November 2001. doi: 10.1103/PhysRevB.64.214422.
- [203] A Fraile Rodríguez, A Kleibert, J Bansmann, and F Nolting. “Probing single magnetic nanoparticles by polarization-dependent soft x-ray absorption spectromicroscopy”. *Journal of Physics D: Applied Physics*, **43**(47):474006, December 2010. doi: 10.1088/0022-3727/43/47/474006.
- [204] M. Salou, B. Lescop, S. Rioual, A. Lebon, J. Ben Youssef, and B. Rouvellou. “Initial oxidation of polycrystalline Permalloy surface”. *Surface Science*, **602**(17):2901–2906, September 2008. doi: 10.1016/j.susc.2008.07.012.
- [205] M. R. Fitzsimmons, T. J. Silva, and T. M. Crawford. “Surface oxidation of Permalloy thin films”. *Phys. Rev. B*, **73**(1):014420, January 2006. doi: 10.1103/PhysRevB.73.014420.
- [206] A. Balan, P. M. Derlet, A. F. Rodríguez, J. Bansmann, R. Yanes, U. Nowak, A. Kleibert, and F. Nolting. “Direct Observation of Magnetic Metastability in Individual Iron Nanoparticles”. *Phys. Rev. Lett.*, **112**(10):107201, March 2014. doi: 10.1103/PhysRevLett.112.107201.
- [207] R F Neumann, M Bahiana, S Allende, D Altbir, D Görlitz, and K Nielsch. “Tailoring the nucleation of domain walls along multi-segmented cylindrical nanoelements”. *Nanotechnology*, **26**(21):215701, May 2015. doi: 10.1088/0957-4484/26/21/215701.
- [208] J. Cantu-Valle, E. Díaz Barriga-Castro, V. Vega, J. García, R. Mendoza-Reséndez, C. Luna, V. Manuel Prida, K. Nielsch, F. Mendoza-Santoyo, M. I. Jose-Yacaman, and A. Ponce. “Quantitative magnetometry analysis and structural characterization of multisegmented cobalt–nickel nanowires”. *Journal of Magnetism and Magnetic Materials*, **379**:294–299, April 2015. doi: 10.1016/j.jmmm.2014.12.022.
- [209] S. Mühlbauer, B. Binz, F. Jonietz, C. Pfleiderer, A. Rosch, A. Neubauer, R. Georgii, and P. Böni. “Skyrmion Lattice in a Chiral Magnet”. *Science*, **323**(5916):915–919, February 2009. doi: 10.1126/science.1166767.

- [210] A. Mehlin, F. Xue, D. Liang, H. F. Du, M. J. Stolt, S. Jin, M. L. Tian, and M. Poggio. “Stabilized Skyrmion Phase Detected in MnSi Nanowires by Dynamic Cantilever Magnetometry”. *Nano Lett.*, **15**(7):4839–4844, July 2015. doi: 10.1021/acs.nanolett.5b02232.
- [211] C. Felser, L. Wollmann, S. Chadov, G. H. Fecher, and S. S. P. Parkin. “Basics and prospective of magnetic Heusler compounds”. *APL Materials*, **3**(4):041518, April 2015. doi: 10.1063/1.4917387.
- [212] T. Graf, C. Felser, and S. S. P. Parkin. “Simple rules for the understanding of Heusler compounds”. *Progress in Solid State Chemistry*, **39**(1):1–50, May 2011. doi: 10.1016/j.progsolidstchem.2011.02.001.
- [213] F. Xue, P. Peddibhotla, M. Montinaro, D. P. Weber, and M. Poggio. “A geometry for optimizing nanoscale magnetic resonance force microscopy”. *Applied Physics Letters*, **98**(16):163103, April 2011. doi: 10.1063/1.3579521.

Appendix A.

Supplement to chapter 7

The nanoSQUID Device

The small loop-size of the nanometer-scale superconducting quantum interference device (nanoSQUID), as shown in Fig. S A.1, encloses an area $\approx 0.4 \mu\text{m}^2$, resulting in an inductance of about 2 pH. In a shielded environment [163], the nanoSQUID used here has a rms flux noise $S_{\Phi}^{1/2} = 200 \text{ n}\Phi_0/\sqrt{\text{Hz}}$ above $\sim 1 \text{ kHz}$, where $\Phi_0 = \frac{h}{2e}$, h is Planck's constant, and e is the fundamental charge. An on-chip modulation line in the bottom Nb layer along \hat{x} is used to couple a magnetic flux $\Phi_{\text{mod}} \propto I_{\text{mod}}$ to the SQUID, where I_{mod} is the modulation current. A flux-locked-loop (FLL) locks the nanoSQUID to its optimal working point and linearizes its output voltage $V_{\text{out}}/\Phi = 2.55 \text{ V}/\Phi_0$.

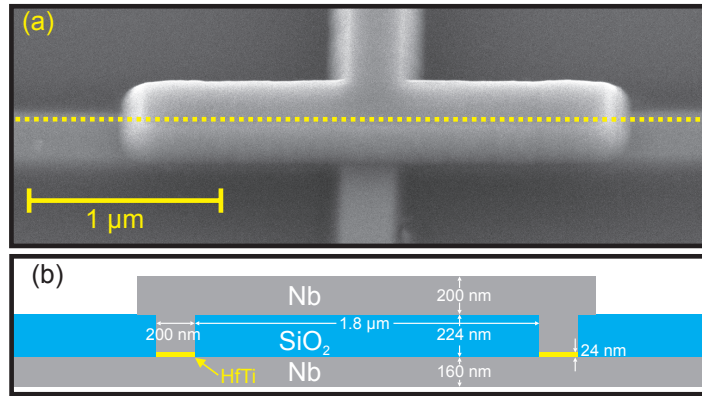


Figure A.1. | The nanoSQUID device. (a) A scanning electron micrograph (SEM) of the device and (b) a cross-sectional diagram of its structure in the plane of constant y defined by the dotted line in (a).

Cantilever Frequency Measurement

The 10- μm -wide paddle near the cantilever tip is used as one reflector of the optical fiber interferometer; the other is the cleaved end of an optical fiber, on which a thin layer of Si has been evaporated in order to match the cantilever reflectivity. 100 nW of laser light at a wavelength of 1550 nm are used in the interferometer in order to detect deflections of the cantilever along \hat{y} . The interferometric signal is fed through a field programmable gate array circuit back to a piezoelectric element which is mechanically coupled to the cantilever. This feedback is used to self-oscillate the cantilever at a given amplitude (typically 50 nm_{rms}), enabling fast and accurate measurement of its fundamental resonance frequency f_c .

Experimental Protocol

To ensure that the experiments – especially scans of $\Phi(x, y)$ and $\Delta f(x, y)$ – start with the nanotube in a well-defined magnetic state, we first saturate it along its easy axis (\hat{z}) by applying $\mu_0 H = 150$ mT. To avoid trapped flux in the nanoSQUID, this saturation is performed at $T = 14$ K, above its transition temperature $T_c = 9$ K. Then, before scanning, which is performed at $\mu_0 H = 0$, the nanoSQUID is zero-field cooled to $T = 4.3$ K and locked to its working point using the FLL.

Ni Nanotube Fabrication

The Ni nanotubes are fabricated by atomic layer deposition (ALD). The reaction chamber and the ALD substrate holder containing the GaAs nanotemplate are heated to 300 °C. As a first step, a 20-nm-thick layer of Al₂O₃ is deposited using trimethylaluminium and water with standard ALD process parameters. Second, for the deposition of Ni, the precursor material NiCp₂ is heated to a temperature of about 130 °C to provide the relevant vapor pressure in the source container. The ALD process flow for Ni consists of a sequence of injection and purging pulses using inert Ar gas, which is repeated 800 times to form a Ni layer of 40 nm. The sequentially injected materials and gases are NiCp₂, ozone, and hydrogen, each followed by a purging process to remove residuals from the gas atmosphere of the ALD reaction chamber. The process reads as follows:

$$800 \times (0.8 \text{ s} | 4 \text{ s} + 10 \text{ s} | 10.0 \text{ s} + 16 \text{ s} | 20 \text{ s}), \quad (\text{A.1})$$

Here, the first two numbers give the durations of the injection and purge pulses of precursor NiCp₂ and Ar, respectively. The third and fourth numbers provide the injection and purge time of O₃ and Ar, respectively; the fifth and sixth numbers define the hydrogen injection and Ar purge time, respectively. Long purging times are used to avoid an explosive mixture of H₂ and O₃ in the pumping line. On a flat substrate, smooth thin films are obtained. On curved nanotemplates, such as the GaAs template nanowires, the shell material shows more roughness than observed in flat films. The smoothness of these shells may be improved by both increasing the injection times of NiCp₂ and decreasing the substrate temperature. We expect the surface of the Ni to oxidize in ambient atmosphere.

Measurement of Ni Nanotube Volume

In Fig. S A.2, we show a transmission electron micrograph (TEM) and a SEM of a Ni nanotube similar to that measured in our measurements. Grown in the same batch and on the same wafer, this nanotube should have identical properties as the measured tube within the natural variation of the growth process. Note the surface roughness, which is responsible for the error in the determination of the Ni nanotube's outer diameter. An average outer and inner diameter is determined by measuring many nanotubes in TEMs and SEMs such as these. The length of the Ni nanotube is determined with an optical microscope. Its volume V_{Ni} is then calculated from these parameters with the uncertainty in outer diameter contributing the largest error. This error is eventually responsible for most of the uncertainty in the saturation magnetization M_S and anisotropy parameters K , which we extract for the Ni nanotube.

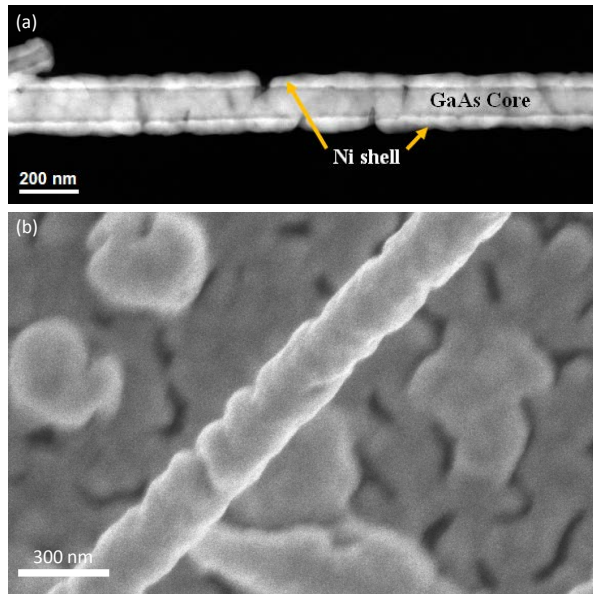


Figure A.2. | (a) TEM and (b) SEM of Ni nanotubes grown in the same batch and on the same wafer as that measured in the experiments.

Further Flux Hysteresis Loops

We record further hysteresis loops of $\Phi_{\text{NN}}(H)$ under similar conditions to that shown in Fig. 2 of the main text and plot them in Fig. S A.3. The switching fields $H_{\text{sw},e}$ are seen to vary from sweep to sweep. Nevertheless, as in the main text, they are observed to occur for $15 \text{ mT} < \mu_0|H_{\text{sw},e}| < 35 \text{ mT}$. The consistently asymmetric behavior at positive and negative fields may be due to an anti-ferromagnetic NiO surface layer providing exchange interaction with the Ni nanotube [190, 191].

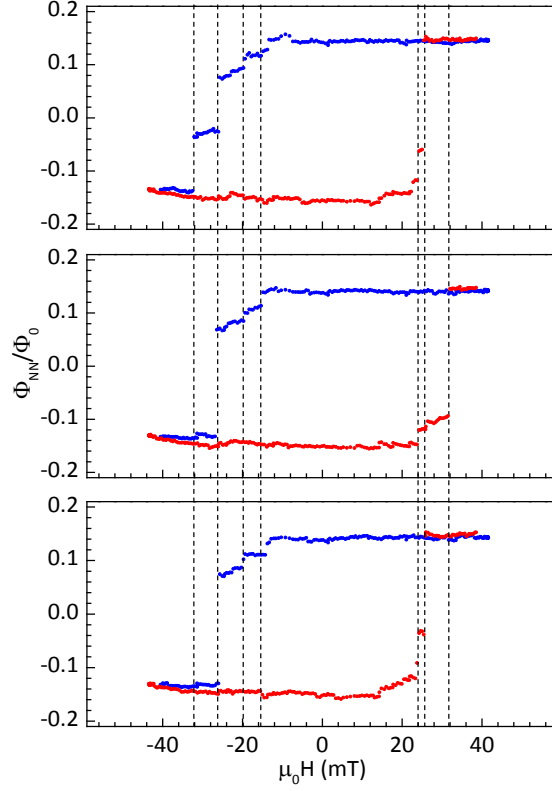


Figure A.3. | Hysteresis loops of $\Phi_{\text{NN}}(H)$ at $z = 280 \text{ nm}$. Red (blue) points represent data taken while sweeping H in the positive (negative) direction. Dashed lines indicate magnetic switching fields $H_{\text{sw},e}$.

Simulated Volume Magnetization and Local Stray Flux

In addition to simulating the volume magnetization $M(H)$ of the Ni nanotubes, we also use the NMAG package [187] to calculate the stray field at the position of the nanoSQUID. The results allow us to determine the predicted stray flux $\Phi_{\text{NN}}(H)$ coupling to the nanoSQUID for each simulated nanotube. The shapes of the simulated $\Phi_{\text{NN}}(H)$ are at all positions and for all nanotube lengths l nearly proportional to $M(H)$ and thus closely follow the shape of the corresponding $M(H)$. An example of a simulated hysteresis loop is plotted together with the measured $M(H)$ in Fig. A.4. Considering a segment of $l = 500$ nml the large jump observed in $M(H)$ near ± 30 mT is reproduced. We expect the further jumps to occur from other segments with slightly longer or shorter l , which contribute to the measured magnetization of the tube.

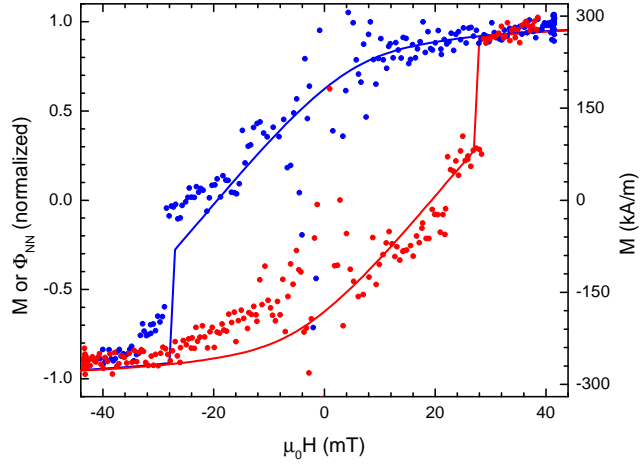


Figure A.4. | Hysteresis loops of $M(H)$ or $\Phi_{\text{NN}}(H)$ simulated by NMAG (lines) and $M(H)$ measured by cantilever magnetometry (points). The Ni nanotube is simulated with $l = 500$ nm and $\Phi_{\text{NN}}(H)$ is calculated with the tube positioned as in the experiments, i.e. at a position of optimal coupling for $z = 450$ nm. The measured data is the same as plotted in Fig. 3 (c). Red (blue) represent sweeps of H in the positive (negative) direction. The left (right) axis corresponds to the simulated (measured) data.

Simultaneous Detection of Switching Events

We further investigate the switching of magnetic domains by sweeping H through the coercive field with the Ni nanotube optimally positioned at $z = 200$ nm. During the sweep, we measure the cantilever displacement y and the flux Φ coupled into the nanoSQUID. To achieve maximum bandwidth the SQUID is operated in open-loop-mode for these experiments, such that a flux Φ produces a response voltage $V_{OL} \approx V_0 \sin(\Phi/\Phi_0 + \theta) + V_{\text{offset}}$, where $V_0 = 20$ μV in our experiment, θ is a phase factor, and V_{offset} is determined by choice of the SQUID's working-point. A peak-to-peak noise amplitude of 4 μV is the result of the room-temperature amplifier used. Fig. A.5 (a) shows y and V_{OL} recorded while $\mu_0 H$ is swept at 1.5 mT/s in a field range where magnetization switching is not expected. V_{OL} undergoes a roughly sinusoidal oscillation of less than one full period, consistent with the change in flux expected from sweeping H . Fluctuations in y with an amplitude of around 5 nm are attributed to the cantilever's thermal noise at 4.3 K.

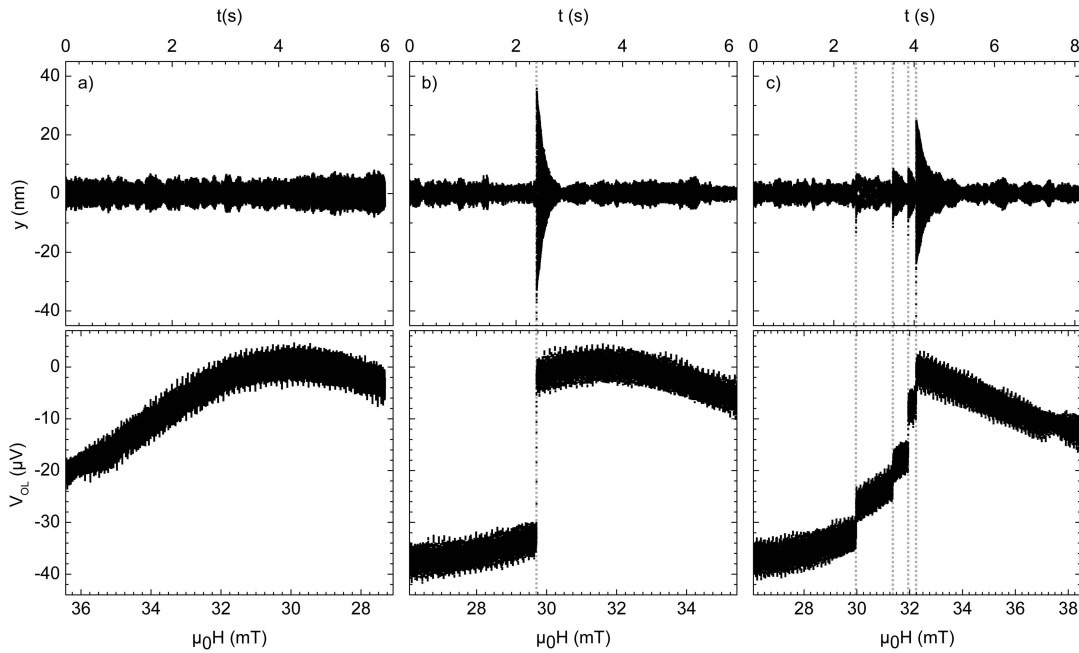


Figure A.5. | Simultaneous measurements of $y(t)$ and $\Phi(t)$ at $z = 200$ μm and an xy -position of optimal coupling. Representative data acquired while sweeping H (a) far from the coercive field and (b), (c) across the coercive field.

In Figs. A.5 (b) and (c), y and V_{OL} are recorded while the field is swept at 1.5 mT/s in a field range where switching is expected. In the first 2.3 s of the sweep shown in (b), the cantilever displacement is given by thermal noise and the flux coupled to the nanoSQUID is free of discontinuities. As a field of 29.7 mT is reached, the cantilever displacement shows a sharp increase in amplitude from 5 nm to 35 nm followed by an exponential decay back to the thermal noise level at around 5 nm. The rise-time is limited by the cantilever's oscillation period. Simultaneous to this mechanical excitation, we observe a jump in V_{OL} . The rising edge is limited by the bandwidth of the preamplifier. Another instance of this behavior is presented in Fig. A.5 (c) where the field is again swept through the nanotube's coercive field. Between 30 and 32 mT, a series of four excitations with varying amplitude appear both in the cantilever

displacement and in the nanoSQUID flux. These two examples are representative of a number of traces taken under the same conditions. The decay time of the mechanical excitations for all events is $\tau \simeq 200$ ms, corresponding to a quality factor $Q = \pi f_0 \tau \simeq 2 \times 10^3$. This quality factor is one order of magnitude smaller than Q_0 . We attribute the reduction to dissipative interactions between the Ni nanotube-tipped cantilever and the nanoSQUID device.

These sudden excitations, given their signature in both the cantilever displacement and the nanoSQUID flux, represent the switching of magnetization domains within the Ni nanotube. On the one hand, the reorientation of a magnetic domain exerts a torque on the cantilever in the presence of an external field and causes its mechanical excitation. On the other hand, the same reorientation suddenly alters the stray field coupled from the Ni nanotube to the nanoSQUID. The kinetic energy imparted to the cantilever by the switching event is estimated as $E_{\text{kin}} = \frac{k}{2\Delta t} \int_t^{t+\Delta t} (y^2 - y_{th}^2) dt$, where t is the time of the excitation, Δt is its duration, and y_{th} is the rms thermal displacement. The magnetic potential energy released in a complete magnetization reversal at field $H_{\text{sw,e}}$ is given by $E_{\text{mag}} = M_s V_{\text{Ni}} \mu_0 H_{\text{sw,e}}$, where M_s is the saturation magnetization of the Ni nanotube and V_{Ni} its volume. For the switching events shown in Figs. A.5 (b) and (c), the magnetic potential energy is estimated to be $E_{\text{mag}} \simeq 3.9 \times 10^{-16}$ J, exceeding the corresponding E_{kin} of the excitations by four orders of magnitude. The large majority of the magnetic potential energy is therefore not captured as oscillations of the cantilever's fundamental mode, possibly dissipating into higher order mechanical modes, as phonons, or as electromagnetic radiation.

Acknowledgements

The exceedingly long author lists of the publications already gave a glimpse, that the work presented in this thesis would not have been possible without the valuable contributions of good colleagues. However, there are more people without their contribution in one way or another this work would not have been possible and my time in Basel not as pleasant.

First of all, I would like to thank my supervisor Martino Poggio for accepting me as a PhD student in his lab. I can not highly enough value the fact that he gave me the chance to pursue this project, despite originally having assigned me to another one. I am grateful not only for the provided freedom to pursue this project, but even more importantly for guidance and moral support whenever necessary. His knowledge of all the bits and pieces in the lab, but even more in understanding the physics behind the data were indispensable to the progression of this thesis.

I thank Joachim Nagel not only for the outstanding teamwork in the lab and the planning of the experiments, but most of all for starting this project together with me in the first place. Without his enthusiasm, LabView wizardry and understanding of nanoSQUIDs this project would have gone nowhere.

I thank Jean-Philippe Ansermet very much for accepting to join my thesis committee and his time spent on this task. I thank Richard Warburton for chairing the defense and putting Basel on my map.

Thanks to Roman Wölbing for taking over the experiments and working together with me during the second half of the project. The perseverance in getting things to run (especially the stubborn SSA) and still not losing the sense of humor was crucial. Thanks to Matthias Kemmler for his contributions in setting up the experiment in the first place and especially the positive thinking that kept us going despite emerging obstacles. For supporting the project and providing scientific input I am grateful to Dieter Kölle and Reinhold Kleiner.

I am grateful to Anna Fontcuberta i Morral, Dirk Grundler and Daniel Ruffer who did not only provide the samples, fundamental to this thesis, but also deep insight into the related science and literature.

For fabrication and supply of the nanoSQUIDs I am thankful to the Fachbereich 2.4 "Quantenelektronik" of the Physikalisch-Technische Bundesanstalt.

XAS measurements were possible due to Armin Kleibert, organizing the beam-time without complication.

A big thank you to all the members of the group, past and present, for creating such a fantastic atmosphere in and out of the lab. In chronological order that is Phani Peddibhotla, Michele Montinaro, Dennis Weber, Fei Xue, Hari Shankar Solanki, Ben Herzog, Andrea Mehlin, Davide Cadeddu, Floris Braakman, Denis Vasyukov, Marcus Wyss, Nicola Rossi, Kavian Davallou, Boris Groß and Panagiotis Fountas. Thank you very much for the amazing time!

I am indebted to Fei Xue for teaching me basically everything I know about handling delicate tasks in the lab like cantilever preparation. Also his support in getting the experiments running is highly valued.

Thank you Dennis, among other things, for the joint work on magnetometry and especially your teaching on how to handle the SEM and FIB. The proof reading not only improved the content, but especially made the thesis look less crude.

Most probably, none of the results in this thesis would have been possible without the department's workshops. I thank Sascha Martin and the machine shop for their rapid and precise manufacturing, Dominik Sifrig for always providing liquid helium also out of schedule and Michael Steinacher and the electronics workshop for their support.

For paying my salary, travel expenses, etc. I acknowledge the Kanton Aargau and the Swiss National Science Foundation (SNSF).

During my time as the group's computer responsible, the support of the department's IT specialist Beat Glatz greatly helped in resolving all occurring computer problems.

For guidance in finding ways through the administrative jungle, the help of Audrey Fisher, Barbara Kammermann, Astrid Kalt and Claudia Wirth is highly appreciated.

For enriching my life in general and distraction from physics I could always rely on dear friends and five familial generations.

Having reached the formal end of my physics education I would like to go back to where it all started and take the chance to thank the members of the ABC-Wg, Cornelius and Benjamin, for the smooth start into the physics studies and the unique time we spent together.

I would like to express my heartfelt gratitude to my parents, who unconditionally supported me throughout my life and made it possible that I could make my way until here. Vielen Dank!

Thank you Constanze for always being there.

Curriculum Vitae

Arne Buchter

Department of Physics
University of Basel
Klingelbergstrasse 82
4056 Basel
Switzerland

Birth: October 19th 1984 in Reutlingen, Germany

Citizenship: German

Education

- 2015 PhD (Dr. phil.) in Experimental Physics
University of Basel, Switzerland
- 2011 Diplom (Dipl.-Phys.) in Physics
Julius-Maximilians Universität, Würzburg, Germany
- 2009 MPhys in Optoelectronics and Lasers
Heriot-Watt University, Edinburgh, United Kingdom
- 2004 Abitur
Friedrich-List-Gymnasium, Reutlingen, Germany

List of Publications

(*) Publication covered in this thesis

1. H. Bentmann, A. Buchter, F. Reinert,
Interplay of electronic structure and atomic ordering on surfaces: Momentum-resolved measurements of Cs atoms adsorbed on a Ag(111) substrate,
Phys. Rev. B **85**, 121412(R) (2012)
2. D. P. Weber, D. Ruffer, A. Buchter, F. Xue, E. Russo-Averchi, R. Huber, P. Berberich, J. Arbiol, A. Fontcuberta i Morral, D. Grundler, and M. Poggio,
Cantilever magnetometry of individual Ni nanotubes,
Nano Lett. **12**, 6139 (2012)
3. (*) A. Buchter, J. Nagel, D. Ruffer, F. Xue, D. P. Weber, O. F. Kieler, T. Weimann, J. Kohlmann, A. B. Zorin, E. Russo-Averchi, R. Huber, P. Berberich, A. Fontcuberta i Morral, M. Kemmler, R. Kleiner, D. Koelle, D. Grundler, and M. Poggio,
Reversal mechanism of an individual Ni nanotube simultaneously studied by torque and SQUID magnetometry,
Phys. Rev. Lett. **111**, 067202 (2013)
4. (*) J. Nagel, A. Buchter, D. Ruffer, F. Xue, D. P. Weber, O. F. Kieler, T. Weimann, J. Kohlmann, A. B. Zorin, E. Russo-Averchi, R. Huber, P. Berberich, A. Fontcuberta i Morral, M. Kemmler, R. Kleiner, D. Koelle, D. Grundler, and M. Poggio,
Nanoscale multifunctional sensor formed by a Ni nanotube and a scanning Nb nanoSQUID,
Phys. Rev. B **88**, 064425 (2013)
5. L. El-Kareh, G. Bihlmayer, A. Buchter, H. Bentmann, S. Blügel, F. Reinert and M. Bode,
A combined experimental and theoretical study of Rashba-split surface states on the $(\sqrt{3} \times \sqrt{3})$ Pb/Ag(111)_{R30} surface,
New J. Phys. **16**, 045017 (2014)
6. (*) A. Buchter, R. Woelbing, M. Wyss, O. F. Kieler, T. Weimann, J. Kohlmann, A. B. Zorin, D. Ruffer, F. Matteini, G. Tütüncüoğlu, F. Heimbach, A. Kleibert, A. Fontcuberta i Morral, D. Grundler, R. Kleiner, D. Koelle, M. Poggio,
Magnetization reversal of an individual exchange biased permalloy nanotube,
accepted in Phys. Rev. B (arXiv:1512.00199)
7. B. Gross, D. P. Weber, D. Ruffer, A. Buchter, A. Fontcuberta i Morral, D. Grundler, M. Poggio,
Dynamic cantilever magnetometry of individual CoFeB nanotubes,
arXiv:1512.00621
8. (*) R. Woelbing, A. Buchter, M. Wyss, O. F. Kieler, T. Weimann, J. Kohlmann, A. B. Zorin, D. Ruffer, F. Matteini, G. Tütüncüoğlu, F. Heimbach, A. Fontcuberta i Morral, D. Grundler, R. Kleiner, D. Koelle, M. Poggio
"Magnetization reversal nucleating at the end of a CoFeB nanotube detected with SQUID and torque magnetometry",
in preparation